UNIVERSITY OF CALIFORNIA, SAN DIEGO

Automated, all-optical cranial surgery for transcranial imaging of mouse brain

A dissertation submitted in partial satisfaction of the requirements for the degree

Doctor of Philosophy

in

Physics

by

Diana Jeong

Committee in Charge:

David Kleinfeld, Chair
Christopher M. Bergeron
Leonid V. Butov
Robert L. Sah
Charles F. Stevens
Clifford M. Surko

2013

The dissertation of Diana Jeong, is approved and it is acceptable in quality and form for publication on microfilm and electronically:

_____

_____

_____

_____

_____

_____
Chair

University of California, San Diego

2013

TABLE OF CONTENTS

LIST OF FIGURES

ACKNOWLEDGEMENTS

First of all, I would like to thank my advisor, Dr. David Kleinfeld for his support and guidance throughout my dissertation research. He generously invested his time for the weekly meetings and laboratory resources for this project. I have learned important skills in both science and life through my interactions with him.

I would also like to thank my committee members, Dr. Charles F. Stevens, Dr. Robert L. Sah, Dr. Clifford M. Surko, and Dr. Leonid V. Butov, and Dr. Christopher M. Bergeron. I am privileged to have committee members from diverse fields, and I sincerely thank them for their scientific advice.

It has been a great pleasure to work with past and present members in the Kleinfeld lab, as I have benefitted so much from talking to my colleagues. I am especially thankful to Dr. Phil Tsai, for his guidance and advice through the hardships in the project and also life. I sincerely thank Allan Schweitzer, for his help on electric circuit and programming as well as his continued patience and encouragement. I thank David Matthews, Celine Mateo, Per Knutsen, and other members in the lab for detailed feedback on the writing and presentation.

I thank many friends in San Diego- my classmates, BMC, UBA, KWiSE, WiSE, and WIP- for their support. I truly enjoyed playing and working with all of you in various volunteer projects.

I would like to thank my family- grandparents, parents, brothers, cousins, and my cat. And I especially thank my husband, Seung Sae Hong for his support.

Chapter1 and Chapter2, in part, is a reprint of D. C. Jeong, P. S. Tsai and D. Kleinfeld, Current Opinions in Neurobiology (2012) 22:24-33. The dissertation author is a first author of this paper.

Chapter2, Chapter3, Chapter4, and Chapter5, in part, are manuscripts in preparation for submission. The dissertation author will be a first author of this paper. The co-authors will be Phil Tsai and David Kleinfeld.

VITA

Ph.D. in Physics	University of California, San Diego	2013
M.S. in Physics	University of California, San Diego	2009
B.S. in Physics	Seoul National University, Seoul, Korea, with Honors	2007

ABSTRACT OF THE DISSERTATION

Automated, all-optical cranial surgery for transcranial imaging of mouse brain

by

Diana Jeong

Doctor of Philosophy in Physics

University of California, San Diego, 2013

Professor David Kleinfeld, Chair

The recent developments of neuroscience have brought us a deeper understanding of the mammalian brain. One of the challenges imposed in neuroscience is to access the brain, with minimal disruption to the neural tissue. The current technologies of using mechanical tools to remove skulls bring both logistical and physiological challenges, as they are labor intensive procedures that are difficult to master. To address this issue, a novel, automated surgical technique has been developed in this dissertation project.

In order to address the issue of automating cranial surgeries, we use ultrafast, nonlinear optics imaging techniques to detect and remove bone. First, applications of the imaging techniques in skull and neural tissue are investigated. Then, the experimental setup and its configuration for automated surgery are studied. Finally, the surgical

technique is used for creating an *in vivo* transcranial window in a mouse skull. The optical quality of the transcranial window is examined via *in vivo* imaging of the vasculature and blood flow. The viability of the brain tissue after the surgery and imaging is assessed using biomarkers for immunohistochemistry.

This dissertation establishes a way to automate sequences of *in vivo* cranial surgery for mouse, using nonlinear optics as feedback and as cutting tools. Direct application of this technique includes *in vivo* craniotomy and making micro-holes for electrode insertion.

Chapter 1. Introduction

The anatomies of animals consist of a variety of distinct tissue types, which may be directly juxtaposed to each other. Hard tissue constitutes bone in vertebrates and chitin in insects, while soft tissue constitutes skin, muscle, connective tissue, and nerve. The ability to surgically operate on hard tissue structures without inflicting damage to surrounding soft structures, such as removing bone while not affecting the underlying nerves, is especially important for *in vivo* neurophysiological studies.

Instead of using mechanical tools, non-linear optical techniques are used to build innovative surgical tools for removing skulls. Since the discovery of light amplification by stimulated emission of radiation (laser), laser systems have been further developed to produce laser pulses with stronger instantaneous intensities. From the strong electric field of the laser pulses, the nonlinear interactions among the photons become accessible, and are now applied to biological systems. In Chapter 2, literatures on ultrafast laser systems, imaging techniques and their applications are reviewed.

Multiple nonlinear optics techniques are implemented to develop the surgical tool, using femtosecond laser pulses. Second harmonic generation imaging is used for the mapping of the skull, while plasma-mediated laser ablation is used for the removal of the skull. Laser induced plasma spectroscopy acts as feedback signals to control the ablation processes. Finally, two-photon laser scanning microscopy is carried out to perform *in vivo* imaging of the brain. The development and construction of the experimental setup are discussed in Chapter 3. Also, detailed protocols for the surgical preparation, skull imaging and ablation, *in vivo* imaging, and histology are provided in Chapter 4.

By incorporating the aforementioned nonlinear optics techniques, a thinned skull window is created all-optically, in a fully-automated setup. First, the construction and mechanical composition of the setup is configured. Then the nonlinear optical methods are applied to biological samples. The nonlinear optical components are combined into a sequence to carry out laser surgery. After the surgery, the thinned skull window is examined by performing *in vivo* imaging of the vasculature and blood flow. Finally, the viability of the window is assessed by immunohistochemistry. The application of the imaging techniques in skull and brain tissue are reported in Chapter 5. The *in vivo* imaging data and histological confirmation of the viability of the brain tissue are presented as well.

This dissertation establishes a way to automate sequences of *in vivo* skull surgery for mouse, using nonlinear optics as feedback and as cutting tools. Further advances of this technique are anticipated, and may include increasing the rate of the surgery by adopting more advanced microscopy techniques. *In vivo* craniotomy and making micro-holes for electrode insertion will be direct application of this technique. The implication of the work and future direction are discussed in Chapter 6.

Chapter 2. Nonlinear optics imaging in biological systems

2.1 Ultrafast laser systems

The discovery of the light amplification by stimulated emission of radiation [1], or laser, which generates strong light that is coherent, has led to investigations of scientific phenomena and the development of applications. Various types of laser systems have been developed over time, and currently, ultrafast laser systems [2] which produce laser pulses with femtosecond temporal width are at the forefront of laser systems.

The femtosecond laser systems were used in this project, applied to processing and imaging biological specimens. As the pulses are extremely short in time, the interaction of the laser pulse and the imaged sample is efficient such that the interaction is highly localized at the focus [3]. This property enables effective *in vivo* imaging and material processing. In this section, the development of the various laser systems will be discussed first, and then the femtosecond laser systems will be introduced.

2.1.1 Conventional laser systems

A laser system produces coherent and amplified photons from externally energized bulk material, or gain medium, which can be in solid crystal or gas form [4]. When the gain medium is energized through various methods, including light and electricity, the energy states of its molecules change their configuration such that more molecules are populated in the energized energy bands, i.e., population inversion takes place. From the population inversion, the excited molecules emit coherent photons via stimulated emission, a process where multiple photons are produced from the perturbation of the molecules by photons. Unlike spontaneous emission, where

incoherent photons are emitted from the excited molecules without stimulation and form broad wavelength ranges, the photons from stimulated emissions are coherent and very narrow in the wavelengths. Thus, the energy externally provided to the gain medium is turned into coherent emission of photons.

The emitted photons can be further accumulated in the optical cavity, where its geometric configuration brings the resonance, which in turn provides additional amplification of the photons. The optical cavity can be formed by installing mirrors, or the gain medium itself can serve as the cavity, too, where the photons are reflected repeatedly within the gain medium multiple times to commence lasing. The cavity provides feedback for the laser and then the beam is released when the intensity reaches the laser oscillation.

2.1.2 Pulsed laser systems

Although the laser beam from the continuous wave (cw) laser system is composed of amplified and coherent photons, the intensity of the laser cannot be easily increased as it would take an extensive amount of energy to produce a powerful laser beam continuously. To address this issue, pulsed laser systems [5] have been developed to increase the intensity of the laser beam. For a cw laser system, average power directly represents the laser power. However, for a pulsed laser system, instantaneous peak power, pulse width, and the repetition rate are taken into consideration to calculate the average power.

One of the common pulsed laser systems is one that utilizes an optical technique of optical switching or Q-switching. The main idea is to amplify the laser pulse by not letting the lasing take place until desired intensity is achieved, and this can be done by

adjusting the laser cavity. For pulsed laser system, the laser cavity is typically composed of two end mirrors with variable reflectance. Saturable absorbers [6] are commonly used for this purpose, and the reflectance of the saturable absorber decreases as the intensity of the laser increases. Therefore, only when the intensity of the laser pulse reaches a certain threshold, the laser pulse is produced and transmitted. Mostly widely used pulsed laser systems are Nd:YAG laser systems [7] , and they utilize Q-switching for producing laser pulses with nanosecond temporal widths.

To produce laser pulses with shorter temporal width, preferably femtosecond, a mode-locking mechanism [8] is used. The principle is to produce discrete laser pulses with short temporal width by adding up different modes of the laser. The modes of the laser are defined from the geometry of the laser cavity, as they form standing waves. Depending on the geometry of the laser cavity, the laser beam can contain multiple longitudinal modes. When the phases of the modes are matched, the modes can be super-positioned to obtain a constructive interference which will result in a Fourier transformation of these modes. Through this mode-locking mechanism, the continuous waves with infinite time domain are transferred to a pulse that has very short time scale, on the range of nanosecond to femtosecond. Consequently, from the uncertainty principle, these temporally short pulses spread out in the frequency domain [9].

To achieve mode-locking, a crystal is first energized by a pump laser to initiate the cw lasing. Then the cw laser beam is passed through an additional optical cavity with optical components such as a prism, grating, and mirrors that are configured such that the mode-locking can take place. The mode-locking can be achieved in active mode-locking or passive mode-locking. For active mode-locking [10], an acousto-opto-modulator is used. For passive mode locking [11], a saturated absorber is used and the

mode-locking is initiated by a slight physical perturbation to the cavity. Typical femtosecond mode-locked laser systems include Ti-Sapphire femtosecond laser systems. The output of the femtosecond laser systems are on the order of a watt [12] and repetition rates of the pulsed laser systems are typically within ~100 MHz ranges.

2.1.3 Amplified laser systems

To obtain stronger femtosecond pulses, the laser pulses are further amplified [13] from the pulsed laser oscillator systems. The main idea is to accumulate multiple femtosecond pulses over time, in order to increase the power per individual pulse. Therefore, the repetition rate of the amplified laser system is reduced, while the intensity of each pulse increases. Among the various techniques to amplify the laser pulses, the regeneratively amplified laser will be introduced, as the system was used in this project.

In the regeneratively amplified laser system, a femtosecond laser pulse is spread out in time (chirped) [14] for avoiding the possible damages to the optical components during the amplification process. The laser system that provides the initial laser pulse is called seed laser system, and a femtosecond laser oscillator is used. The chirped pulse is sent to an optical cavity with a crystal which is energized by a pump laser, and nanosecond pulsed laser systems are typically used. The pulse travels repeatedly through the energized crystal to gain additional energy, and its intensity increases. When the laser pulse finishes its designated number of travels through the cavity, the laser pulse is released from the cavity then gets reshaped to recover its original temporal width.

Pockels cells, optical components with transmission coefficient can be adjusted by applied voltage, are used for defining both the geometry and the number of travels

across the optical cavity for amplification. Fast electronics, on the order of nanosecond precision, is required to manipulate the Pockels cells. For example, a voltage will be assigned to a Pockels cell at 0ns and another voltage will be assigned to the other Pockels cell at 20ns to produce amplified photons with multiple roundtrips through the crystal and cavity.

For expanding and shrinking the temporal width of the seed laser and amplified laser, a grating and a prism are used. The laser pulse energy obtained from the amplified laser system ranges up to 1mJ [15], and the repetition rate ranges up to on the order of 10 kHz. With a high numerical aperture lenses, the fluence of the focused laser pulse is strong enough to initiate laser ablation through plasma. It is possible to remove material by using the plasma created from laser pulses, which can lead to laser machining. The mechanisms of the plasma-mediated laser ablation will be discussed extensively in the plasma-mediation ablation section.

In this project, two different lasers, the Ti-Sapphire laser and femtosecond regeneratively amplified lasers, were used for second harmonic generation imaging and removal of the skull via plasma mediated ablation, respectively, and will be introduced in Chapter 3.

2.2 Microscopy

2.2.1 Wide field microscopy and confocal microscopy

Different types of microscopy [16] have been developed in order to investigate microscopic structures with better resolution and for application in different environments. The most commonly used system is the wide-field microscope [17], which uses

incoherent light sources with broad emission spectra. More advanced systems utilize coherent light sources such as laser, to obtain higher resolution, and to use nonlinear optics [18]. Various nonlinear optics techniques are used for *in vivo* imaging of varying tissues, such as bone and brain tissue. Multiple microscopy systems are introduced in the section, from the wide-field system to the two-photon laser scanning microscopy system.

The wide-field microscopy utilizes multiple lenses to magnify the specimen and uses filaments for light sources. For uniform illumination, the lenses are placed to form the Kohler illumination [19]. The condenser aperture adjusts the brightness of the illumination. Typical resolution of the wide field microscope ranges ~1μm.

Wide field microscopy can also encompass fluorescence microscopy utilizing optical filters. The main idea is to separate out light with specific wavelength for excitation, and also collect only fluorescent light for signal. The optical filters and dichroic mirrors are used to select the light with specific wavelengths. For excitation, dichroic reflects the laser beam into the microscope objective. However, the fluorescent signal is transmitted through the same dichroic mirror, as the fluorescence signal has wavelength within the transmission region of the dichroic mirror.

With the development of laser systems, the coherent, monochromatic beams became available as light sources in microscope systems, and confocal microscopy systems [20] are developed. The laser beam is focused with a microscope objective, and the sample is scanned with the focused laser beam. The fluorescence generated from the sample is passed through an aperture to eliminate out-of-focus light. The resolution in axial scan is enhanced as the out-of-focus light is physically illuminated, and from this

property, optical sectioning becomes possible. The resolution of the confocal microscopy is diffraction limited, and is less than 1μm [21].

2.2.2 Two photon microscopy

Although the confocal system has enhanced resolution, it is not feasible for *in vivo* imaging due to the photo-toxicity [22]. In order to perform *in vivo* imaging, non-linear optics techniques such as two-photon excitation [23] are utilized. The non-linear optics techniques utilize the strong intensity of the laser pulses, and the interaction of the photons generated from the pulses. We introduce the two-photon excitation technique, which is applied to the measurement of blood flow and brain imaging.

Typically, in order to excite a fluorescent molecule, a photon with its wavelength within the excitation wavelength is used. However, the two photon excitation is a phenomenon where the fluorescent molecules are excited with two photons instead of one photon. The two photon excitation takes place when the intensity of the laser pulse is strong enough such that two photons are impinged on the molecule within the femtoseconds. In order to meet this condition, the fluence from the laser pulse should be greater than 10^{-3}J/cm^2 [16]. To penetrate into the scattering tissue, laser pulses with wavelength in near-infrared are typically used.

Due to the high-intensity requirement, the two photon excitation only takes place at the focus and this is advantageous towards *in vivo* imaging [24]. The focal volume that undergoes excitation that is highly localized, and is on the order of femtoliters. This highly localized excitation gives rise to optical sectioning capabilities without apertures, with diffraction limited resolution. The axial resolution for two-photon imaging is ~0.1μm.

Photo-toxicity is greatly reduced due to the minimized volume of excitation, and the two-photon laser microscopy is widely applied for *in vivo* imaging. The photo-bleaching of the fluorescence molecule is also minimized due to the localized excitation.

The two-photon microscopy is applied to *in vivo* imaging of various biological systems, with the recent development in cell biology [25]. Examples of *in vivo* two-photon imaging include the imaging of neuronal structures, astrocytes, and the vasculature [26]. As the two-photon microscopy requires fluorescent molecules, more applications became available with the development of dyes [27], fluorescent transgenic animals [28], and transfection of cells [29]. The dyes are developed to mark only specific cell types or cell activities. One of the examples is calcium sensitive dyes, which are used for the detection of neuronal activities. Transgenetic mice are genetically modified in order to produce targeted, fluorescent cell lines. Specific imaging of various cell types such as microglia, neurons, and pericytes [30] are available. Finally, cells can be labeled using virus infections [31].

2.2.3 Configuration of two-photon laser scanning microscopy

For the realization of two-photon laser scanning microscopy, multiple technical considerations are required for constructing a microscope. The main idea is to scan the beam across the region of interest in the sample and collect the fluorescence per each scanning point. [32]. The two photon scanning microscopy setup was built from previous projects in the lab, and the configuration is introduced in this section.

The two-photon laser scanning microscopy (TPLSM) setup was composed of a scanner, an eye piece, PMT-optics assembly, a microscope objective and translational

stages. The PMT-optics assembly was mounted onto a slider to conveniently change the optical filters and dichroic mirrors.

Different optical filters were used to select only the signal within specific wavelength ranges. There are mainly two purposes of two photon imaging: to image bone, and to image blood flow and vessel structures. In order to image bone, filters to collect second harmonic photons are inserted into the detection module. For imaging of blood flow and vessels, dyes such as fluorescein dextran were injected into the bloodstream to provide contrast. The emission wavelength of the second harmonic photons and two-photon fluorescence are configured to be separated in terms of wavelength, in order to image bone and blood flow simultaneously. Dichroic mirrors were used for coupling in the excitation wavelength and transmitting the signal.

In order to control the various components in the TPLSM setup, a software (MPScan), has been used. Through the MPscan, the scanning parameters, such as the scan rate, the size of the scanning area, the scanning mode, the frame rate, and the amplification of the signal were defined [33]. Also, the MPScan assembled the signal detected from the photomultiplier tube to form images. Images over three-dimensional volume can be taken from MPScan via stack measurements.

Specific regions in the vasculature were selected to be scanned for blood flow measurement, through a computer algorithm called Arbitrary Scan. A region in the brain was scanned in fixed position in z first, and the obtained image was called to the Arbitrary Scan. Then a specific region of interest in the image was selected, typically across and along a single vessel. This algorithm enables efficient scanning only the region of interest, without scanning the entire field of view [34].

After the blood flow data was obtained, the analysis was carried through software called PathAnalyzeGUI. The main principle is to utilize Radon transformation and Fast Fourier transformation for discrete measurements. The window sizes for smoothing can be selected for optimized spectral analysis. From the measurement, the diameter of the selected vessel and the velocity of the blood flow through the vessel can be obtained [35]. The variations of the diameter and velocity over time were further analyzed by spectral analysis, by utilizing a software program, Chronux [36]. The frequency components in the blood flow can be detected by the algorithm.

2.3 Second harmonic generation

From the pulsed laser sources, several nonlinear optical techniques became available. Second harmonic generation (SHG) is one of the nonlinear optics techniques used in this project. The SHG provides a means to detect the surface of the skull or other hard tissue as well as to map the local shape of the surface. Range-finding based on interferometric techniques is common, yet the range-finding can also be performed by harmonic generation with ultra-short laser pulses [37]. In particular, second harmonic generation allows the mapping of the front surface, as well as the back surface of sufficiently thin materials.

Second harmonic generation is a nonlinear process that produces coherent photons with twice the frequency of the incident laser pulses when the intensity of applied laser pulses is sufficiently high [38, 39]. Typically, when the incident laser pulse interacts with dipoles within the material, the dipoles are polarized and the polarization of the material is linearly proportional to the applied light, i.e., electric field. However, when the electric field is increased, the higher order polarization of the dipoles that are

proportional to the intensity squared become significant. In this section, the principles of the second harmonic generation are introduced and the application of second harmonic imaging is discussed.

2.3.1 Physics of second harmonic generation

When a great intensity of electric field is applied, the generation of photons with doubled frequency of incident photons' are become significant. This nonlinear optical phenomena is called second harmonic generation. It occurs because the dipoles in the sample get oscillated with higher terms and the second order terms are most visible among the higher order terms, i.e., second harmonic generation [40].

Typically, the magnitude of polarization (P) can be approximated to be linearly dependent on the electric field (E), $P=\chi E$, where χ is polarizability. However, the full expression for the polarization includes higher order terms.

$$P=\chi_1 E+\chi_2 E^2+...$$

The higher terms are often neglected as the coefficients decrease with $1/E_n$, leading to the well-known approximate expression which defines the relationship to be linear.

The second order term is what we call second harmonic generation. The coefficient of the second order term (χ_2) is called hyperpolarizability [41], and can be obtained by adopting slowly varying approximation [42].

As shown above, second harmonic generation process intrinsically produces coherent photons from the dipoles in the sample. The whole procedure is very fast, on the order of femtoseconds when using femtosecond laser pulses. Also, no external dyes are necessary for the imaging. These properties can be advantageous for the application

in imaging, because photo-bleaching is a non-issue for second harmonic generation, the imaging is done without the use of dyes [43].

2.3.2 Conditions for strong second harmonic generation

Although the second harmonic generation is an intrinsic phenomenon, certain conditions need to be met in order to produce a strong second harmonic signal. First of all, the hyperpolarizability of the material should be large such that the dipoles in the material interact strongly with the incident photons. The strength of the signal depends on the molecular structure of the material [44].

Another requirement for strong second harmonic generation is that the asymmetry in topology of the dipoles is such that the second harmonic signals do not cancel each other out. The second harmonic generation signals are coherent vector quantities and the signals can interfere constructively or destructively. The molecules in the sample should be arranged so that they form a non-centrosymmetric structure. In biological systems, these non-centrosymmetric structures can be widely found. Examples include cell membranes and asymmetric proteins which contain fiber structures that are non-centrosymmetric [45].

In addition to the asymmetric topology, the phases of the second harmonic signals should be matched for constructive interference. Due to the phase matching condition, the thinner sample is advantageous for stronger signals. When the phase matching condition is not perfectly met, quaisi-phase matching can be performed for enhanced signals [46].

Although the second harmonic generation is different from two-photon excitation in terms of signal characteristics and excitation processes, they share similar parameters as they are both second order non-linear optics. For both techniques, femtosecond laser pulses from Ti-Sapphire systems are typically used. The wavelengths are in near-infrared to penetrate into the deeper tissue. As mentioned earlier for two-photon microscopy, higher numerical aperture is advantageous for diffraction-limited resolution [47]. The second harmonic generation also possesses optical sectioning capabilities rising from a highly localized excitation volume.

2.3.3 Application of second harmonic imaging in biological systems

Many tissues, including bone [48, 49], connective tissue [50], and nervous tissue [51] meet these criteria. In the case of bone, the tissue contains a lot of collagen which is fiber-like protein that generates strong second harmonic signals, and also contains hydroxylapatite, which is calcified and crystalized bone tissue that also generates strong second harmonic signals.

Most biological samples scatter a lot, and the scattering is more severe in bulk materials such as bone. The back scattered second harmonic signals are obtained. As mentioned earlier, the quasi-phase matching enhances the second harmonic signal collected in back-scattered form.

For automated surgery, the second harmonic generation will be used as a means to map the surface of the bone and to measure the thickness of bone. *In vivo* second harmonic imaging is particularly useful for feedback guided surgery, since it depends only on intrinsic properties of the sample and does not require external dyes to image

[52, 53, 54]. The application of second harmonic generation imaging of bone will be further investigated in later chapters.

2.4 Plasma-mediated laser ablation

Interaction between materials and laser pulses can be further extended to plasma-mediated laser ablation, which is a process that removes materials by creating local plasma with laser pulses [55]. When a strong laser pulse is focused onto the sample, plasma is created locally at the focus. The laser ablation technique provides cutting precision up to diffraction limited accuracy. Compared to the conventional, mechanical removal of materials, the laser ablation can be advantageous when applied to biological system due to the minimized collateral damages. In this section, the principles of laser ablation and the application of laser ablation to biological systems will be introduced and discussed.

2.4.1 Physics of plasma-mediated laser ablation

Plasma-mediated ablation with pulsed laser excitation builds on the concept of local excitation of molecules through nonlinear absorption. However, the energy densities used for ablation are high enough to tear molecules apart, rather than just drive electronic transitions that lead to fluorescent relaxation [56]. The photo-ionization takes place with the strong electric field form the laser pulses. The photo-ionization can be linear or non-linear, i.e., take single photon or multiple photons for the ionization. In the case of insulators, the non-linear photo-ionization dominates over the linear ionization. The non-linear photo-ionization has multiple mechanisms, including tunneling ionization and avalanche ionization.

Energy fluence, defined as the energy per unit area in the pulse, is a natural metric to describe the extent of material damage produced by a short laser pulse focused to a spot. As an example, a 10-nJ, 100-fs pulse that is focused to a 1-μm^2 area yields a fluence of 1 J/cm^2 or an intensity of 10 TW/cm^2. This is equivalent to an electric field of ~ 10^8 V/cm or ~ 1 V/Å, approaching the ~ 10 V/Å Coulomb field seen by valence electrons in atoms and molecules, and leads to significant electron tunneling that frees bound electrons from their molecular orbitals [57].

The plasma grows as the free electrons seed an impact ionization cascade that involves acceleration of the electrons. The dominant procedure is inverse-Bremsstrahlung absorption, in which an electron absorbs photons while colliding with molecules [58]. After several absorption events, the free electrons achieve sufficiently high kinetic energy to ionize another molecule by impact ionization. This cascade, along with the continued generation of photoelectrons, leads to exponential growth of a micrometer-sized plasma bubble. Eventually the plasma becomes dense and limits the penetration of the incident light to a skin depth of only tens of nanometers. The restricted penetration depth provides axial localization of the plasma that is far less than the focal depth of the incident light.

The plasma created by a femtosecond laser pulse can be characterized by the physical parameters. For the plasma created from femtosecond laser pulses (~100fs), the plasma energy density is on the order of ~1kJ/cm^3 with the electron density of $10^{21}/cm^3$ [59].

The photo-ionization leads to lattice vibration, and results in the melting of the sample. For the plasma created from nanosecond laser pulses, the laser pulse duration

overlaps with the time scale for the lattice vibration, whereas the femtosecond laser pulses disappear before the lattice vibration takes place. The femtosecond laser ablation benefit from the short pulse duration, as the energy of the laser pulse is entirely spent on photo-ionization, leading to much more efficient deposition of energy onto the sample.

The advantage of using ultra-short pulses, as opposed to nanosecond pulses, is a decrease in the threshold value of the fluence necessary to cause ablation [60,61,62]. The minimal fluence of 1 J/cm2 can be achieved with a 10-nJ, 100-fs pulse, focused to a 1-μm^2 area. In practice, fluences of 10 to 100 J/cm^2 have been used for the ablation of a number of hard tissues, beginning with pioneering work on cuticle [63], followed by the cutting of dental enamel [64], dentine [65] and, of direct relevance, bone [66-69]. The precision of plasma-mediated ablation of hard tissue was demonstrated by cutting microscopic features in bone [70].

The termination of the laser pulse is followed by recombination of the free electrons with the positively ionized molecules at the focus. This occurs on the picosecond time scale of electron collisions at typical electron densities, and leads to a transfer of energy from the electrons to the material. The time scale of the recombination is short, compared to the ~ 100 ps acoustic relaxation time in the material. The result is a dramatic pressure increase within the excitation volume that can produce a rupture of the material and form a cavitation bubble. The bubble constitutes the region of ablation. The expansion of the cavitation bubble is associated with an acoustic shockwave that propagates into the surrounding tissue [71] and has the potentially deleterious effect of spreading damage into the sample.

2.4.2 Heat transfer from plasma

A critical issue for the use of plasma-mediated ablation in surgery is the magnitude and extent of the rise in temperature that surrounds the ablation region. The literature is equivocal on this point. Theoretical calculations point to a rise in temperature that decays in less than a micrometer from the site of the plasma bubble [72]. Yet direct measurements of the rise in temperature range from one-tenth to ten degrees at distances of tens to hundreds of micrometers from the site of ablation [73-76]. As a practical matter, microscopic ablations have been achieved for the cutting of fine sub-cellular processes [77-80], as well as the cutting of corneal tissue [81, 82] and the manipulation of fine vascular processes [83-85]. Histological analyses of brain tissue ablated with a strongly focused beam show that the damage is confined to within a micrometer of the ablated surface [86]. In total, these data support the utility of plasma-mediated ablation with ultra-short laser pulses as a precision surgical tool.

2.5 Laser-induced breakdown spectroscopy

Second harmonic generation enables the non-disruptive determination of surface location and curvature and sample thickness, yet the signal is not unique to the type of tissue. The complementary technique of laser induced plasma spectroscopy (LIBS) [87-89] may be used to distinguish hard from soft tissue. Here, the light emitted from the ablation region, which corresponds to the recombination spectra of ionized atoms and molecules, is analyzed with a spectrometer to resolve the atomic composition of the material. The laser induced plasma spectrum can be used to distinguish biological samples based on their chemical composition [90-93]. In particular, bone and other calcified tissue may be distinguished from soft tissue based on the strong calcium emission peaks [94-96]. In this section, the principles of LIBS and its application are introduced.

2.5.1 Physics of Laser-induced breakdown spectroscopy

When the plasma created from the laser cools down, the ions and electrons recombine and emit photons that are specific to the element composition of the sample. This technique is called laser induced breakdown spectroscopy [97]. To be more specific, when the laser pulse first ionizes the atoms, Bremsstrahlung takes place, i.e., the free electrons interact with the ions and emit photons with broadband wavelengths. For the case of using femtosecond laser pulses, it takes about several nanoseconds for the broadband light to decay away [98]. When the electrons emit their excess energy and finally recombine with the ions, they emit photons with specific wavelength to fall to ground states. The duration of these spectral emissions is about several nanoseconds [99].

The emission peak can be isolated from the broadband spectrum using time-resolved spectroscopy, which takes data with varying temporal delays [100]. To illustrate the time evolution of the plasma emission, an example of time-resolved spectroscopy is presented in figure 2.1. The exclusion of the broadband signal can be done by using an intensified charge-coupled device (ICCD) [101]. The ICCD is composed of multi-plate channel where photons are converted to electrons with a presence of strong electric field. By varying the voltage across the multi-plate channel, the data acquisition of ICCD can be operated within nanosecond time scales. Delays are given to the ICCD in order to obtain at different time points. The emission peaks which come after the broadband spectrum are collected by setting a specific temporal delay, based on the time evolution of the plasma emission.

Recent development of the femtosecond lasers paved the path to femtosecond laser induced breakdown spectroscopy [102], although much of the field of laser induced breakdown spectroscopy has been done with nanosecond laser pulses. As the pulse duration is so short that the laser pulse cannot interact with the plasma that already has been created, the broadband emission lasts a much shorter length of time and the signal leads to much higher signal to noise ratio [103]. For the application in surgical settings, femtosecond pulses are used as the heat transfer and collateral damages are minimized for femtosecond pulses, as mentioned earlier.

2.5.2 Laser-induced breakdown spectroscopy under aqueous environment

Feedback guided surgery must frequently be performed in an aqueous environment to protect living tissue. In this case, the laser induced breakdown spectrum may be unresolved as a result of pressure broadening and shortened emission lifetimes [104,105]. A number of approaches have been implemented to overcome these complications. Of particular interest is to utilize double-pulse excitation scheme to increase the signal to noise ratio [106-109].

In the case of LIBS with nanosecond pulses, double-pulse experiments have been performed and significant increase in the signal to noise ratio is reported in both ablation in air and under aqueous environment [110]. The idea is to split a laser pulse into two and delay one pulse in time and the second pulse can interact with various by-products created by the first pulse depending on the time evolution of the plasma created by the first pulse.

For femtosecond LIBS, double pulse setup is tested only in the air. Here, the incident ultra-short laser pulse is split with both pulses focused on the same region of the

sample, but with one temporally delayed by order of one nanosecond, relative to the other [111,112]. The second pulse interacts with the plasma created by the first pulse, and the emission spectrum has a greater signal-to-noise ratio than the spectrum after a single pulse. This improvement may relate to greater heating of the plasma, or to the formation of an air-like expansion environment after the first pulse that minimizes pressure broadening of the plasma emission after the second pulse [113-116]. Further, temporal-gating of the collection of the spectra will isolate the signal from the initial broadband spectrum that is generated by nonlinear processes and by initial pressure broadening at the center of the plasma bubble [117-119]. Details aside, the existing literature supports the real-time identification of bone versus soft tissue via their optical emission spectrum on a pulse by pulse basis, and forms the platform for control of the laser ablation beam in surgery.

2.6 Cranial surgery for accessing brain

The anatomy of animals consists of a variety of distinct tissue types that may be directly juxtaposed to each other. Hard tissue constitutes bone in vertebrates and chitin in insects, while soft tissue constitutes skin, muscle, connective tissue, and nerve. The ability to surgically operate on hard tissue structures without inflicting damage to surrounding soft structures, such as removing bone while not affecting underlying nerve, is especially important for *in vivo* neurophysiological studies.

In vivo imaging of neuronal activity [120] or blood flow [121] in the brain with resolution near the optical diffraction limit typically requires mechanical thinning [122-124] or removal [125,126] of a portion of the skull to gain optical access to the brain. The craniotomy can be more physiologically damaging, as the pressure and temperature of

brain can change rapidly. The recently developed thinned skull technique offers more stable way of imaging neurons, but the physical access of brain is not obtained.

The realization of a craniotomy and thinned-skull preparation requires fine surgical skill and is typically performed with a hand-held dental drill. To be more specific, first the scalp and periosteum are removed from skull, and then the skull is manually thinned to obtain optical transparency with a dental drill. The thinned portion of the skull is used as window for imaging. For full craniotomy, the thinned portion of the skull is carefully removed to obtain physical access to the brain. No quantified feedback signal on how much bone to be removed is provided, and the surgeon has to rely upon the skills obtained through surgical experience. Also the procedures are manually performed, and significant amount of training is required for obtaining surgical techniques.

The outcome of the procedure can vary widely from surgeon to surgeon. This influences the physiology of the underlying brain, including the potential for inflammation [127], disturbed vasodynamics [128], and cortical spreading depression [129]. Craniotomies often stand as the rate-limiting step in biomedical research that enables the use of sophisticated optical tools to image structures deep within the cortex [130,131] of mouse models of brain function, in which structural or functional fluorescent indicators are expressed in specific cell types [132]. Lastly, a similar set of concerns exists for gaining optical access to the spinal cord [133].

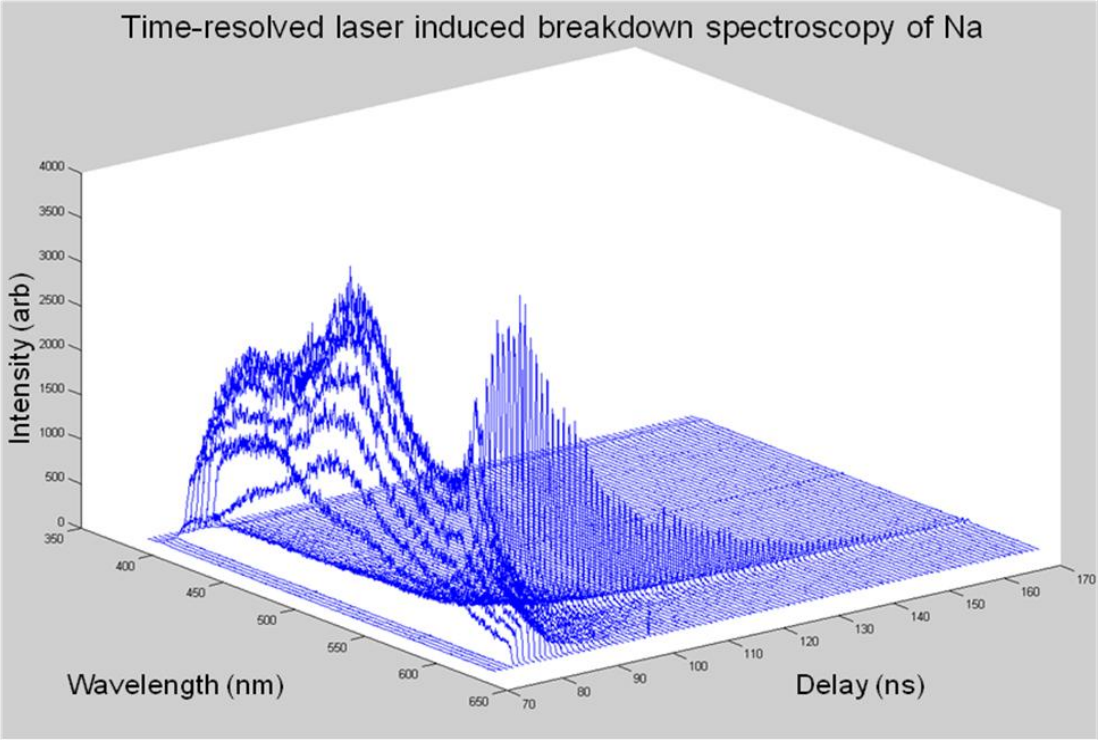

Figure 2.1. Time-resolved spectroscopy for laser-induced breakdown spectroscopy. Measurement of time resolve spectroscopy of sodium emission obtained from phosphate buffered saline, is shown as an example. After the plasma has been created from a laser pulse, it expands and releases its energy by emitting photons. First, the laser pulse arrives at 8ns, then the free electrons recombine with ions and emit broadband spectrum (Bremsstrahlung), as shown in 18-25ns window. After the recombination, the excited electrons generate discrete sodium emission peak at 588nm, as shown in 26ns-50ns. The emission signal decays away as the plasma is further cooled down.

Chapter 3. Construction of experimental setup for automated cranial surgery

In this chapter, technical considerations for the setup and the construction procedures will be discussed. The project involved multiple devices, including lasers, electronic circuits, and mechanical components. Therefore for the construction of the setup, it is critical to consider the technical details of the individual components and also their compatibilities. Also, the computer algorithms and triggering schemes for controlling the automated surgery are presented. Once the setup has been established, the development of methodologies for the automated surgery will be presented.

3.1. Mechanical setup: stage, motors, and motor controller

In order to automatically image and remove an area of bone, it is necessary to have a motorized stage system which can be driven by a computer program. The motorized stages and motors were selected to ensure precise movements in both time and space on the order of milliseconds and micrometers, relatively (figure 3.1.). The x-stage and y-stage (Danaher, XYR-8080) operated via lead screws, and z- stage via on ball bearing. Extra power supply of 20v and 16A was used to un-lock the break on the z stage. A set of optical encoders (Renishaw) were installed on the stages to read out their positions up to micron precision. Stepper motors for x-y stage had lead screws with a pitch of 508μm and the motor for z stage had a 2mm pitch ball screw. This combination of motors and stages provided precise movement to minimum travel amount to 0.3μm and with velocity up to ~35mm/s.

The setup was configured to minimize the resonance, which could undermine the accuracy of the imaging and ablation. The x-stage and y-stage were mounted separately from the z-stage to minimize the vibration from the cantilevered structure. To further damp the possible vibration, multiple damping blocks were attached to the optics rail, which was cantilevered out from x-stage.

The x- stage and y-stage were mounted on five risers and a plate, to be about 30 inches above the table, providing enough room to place the animal. The standard adapter plate for the NEMA-23 motor was replaced by a custom-made l-bracket to attach a routing mirror and a beam expander, at a fixed distance from the dichroic mirror. On top of the x stage, collection optics was attached via another l-bracket. The z stage was mounted on an x-95 rail on the optical table and an l-bracket was attached to the stage to provide a mounting plate for the animal. Multiple adapter plates were custom made to mount the stages onto the optics table and x-95 rail. Also, additional adapter plates were needed for mounting the optical components onto the stages.

The linearity of the motorized stages was tested to ensure the accurate stage movements. Stage linearity refers to the linear movement of the stage according to the commands given by the stage controllers. A command was given to the stage to move at a constant speed, and then the real-time position of the stage was measured with an optical encoder. The stage controller gave commands to both steer the stage. and to record the position of the stage. As shown in the figure 3.2., the stage moved in a linear fashion except at the very end of the run, as the acceleration took place to completely stop the stage. From this measurement, it was confirmed that the stage moved linearly and reliably, to the commands given by the motor controller.

3.2 Electrical command and configuration

The motors were controlled by a motor controller (DMC-40x0, Galil) and the controller was driven by software written in MATLAB. The controller had its own language, as shown in figure 3.3. First, the motor configurations, such as step sizes, acceleration, and current settings were defined. These command were called constantly, and were written in a file then downloaded into the local memory of the motor controller.

After the settings were established, the commands to actually run the motors were sent out. Exact control of when a specific command should be given out were managed by utilizing set point commands. The set point commands included thresholding the position, acceleration, or velocity of the motors. Also, it was possible to control the exact timing of each segment of the motor movement. This precise control was possible due to the property of the command line, as the commands were given in a single line, and each command takes action only after the previous condition is met. Also, digital trigger signals were given out by the motor controller, providing timing control, or synchronization, among multiple apparatus.

For example, to move the stage in z direction, the travel distance was defined first, and then the command to begin movement was given out. A digital trigger was sent out to open the shutter. Set point commands were inserted, to open the shutter only after a certain distance or at a constant velocity. In this example, a command which detects the complete stop of the motors was used as a set point for closing the shutter. When the motor finished its movement, the conditions for the satisfied and the digital trigger was turned off, and then the shutter was closed. An asterisk was printed out after the entire procedure was finished.

The motor controller was interfaced with the MATLAB code in order to drive the motors from the computer, as shown in figure 3.4. The communication was carried through the RS-232 connection. For initializing the MATLAB to setup communication, the serial object was configured. The baud rate was 115200, terminator was set to ':', and the readout mode was set to asynchronized. These configurations were critical for accurately sending out the commands and reading in the outputs, such as position and velocity, from the stages. After the connection was established between the motor controller and MATLAB, it was possible to send the command to the motor controller and readout outputs from the controller.

3.3 Detection of photons using photomultiplier tube and intensified charge-coupled device

Two different detection modules were used to detect photons that are generated from biological tissues, the photomultiplier tube (PMT) and the intensified charge-coupled device (ICCD). For the measurement of second harmonic generation signals, photomultiplier tubes were used for effective detection of photons at low light levels. For the spectroscopy of photons that are generated by plasma-mediated laser ablation, an intensified charge-coupled device spectrometer was used for time-resolved spectroscopy.

In order to image skulls though SHG, it was important to have high resolution across the sample, to have precise measurements of surface position and the thickness of skull. This required a high duty cycle for detection apparatus, i.e., converting the second harmonic photons continuously without any downtime. Also, the wavelength of the emitted photons was fixed, which made it ideal to use a photomultiplier tube. Within

the detection wavelength, photomultipliers do not have wavelength specific detection of photons. As the photons were converted to electrons via phosphorous plate in single channel, continuous detection was possible. The photomultiplier tube used in this project is Hamamatsu H7422-40. The quantum efficiency is around 40% and photoelectron gain at maximum voltage reads 10^6. Collection optics for the detection through the photomultiplier systems consisted of a dichroic mirror(Chroma, ZET 405) to separate out the second harmonic signal at 400nm, a filter(BG 39) to remove laser line and a lens(Thorlabs, AC 254-50-A) to focus the detected photons to PMT.

For detection of photons from the plasma ablation of bone, it was important to be able to detect photons over a range of wavelength. Another important capability required was to have temporal resolution for distinguishing early broadband photons created from plasma, versus the discrete emission which come later in time. This time resolution enhanced signal-to-noise ratio for the spectroscopy. The temporal resolution required was on the order of nanoseconds, for both gate delay and gate width. Intensified charge-coupled device was used for time resolved spectroscopy.

Intensified charge-coupled device (ICCD) is composed of an intensifier tube with an array of charge-coupled devices (CCD). The ICCDs are capable of collecting photons over a range of wavelength with nanosecond precision. The intensified charge-coupled device used here was from Andor (iStar DH720-18F-63). The quantum efficiency is around 40% and photoelectron gain is on the order of 500 fold. Typical gating conditions are 10-20ns gate delays with 5 to tens of nanosecond gate width. The shift speed of the pixels was on the order of 1us. Collection optics for the ICCD consist of a primary dichroic mirror to separate signals from laser line (700DCXRU), a lens (Thorlabs, AC 254-100-A) to focus collected photons, and an optical fiber (Thorlabs,

M25L02) to deliver the photons from the lens to ICCD. Maximum spot size of the collected beam after going through the lens was calculated to make sure all the photons can enter through the opening of the fiber, which was 200µm.

The ICCD was connected to a spectrometer (Shamrock 303i, Andor), and the wavelength was calibrated through the software. The resolution of the spectrometer was 0.1nm. The detection range for the spectrometer was defined by the length of the ICCD, and in our system, it was 350-700nm. Also, the dynamic range of the ICCD was 350nm, and the quantum efficiency of the ICCD was around 40%.

Acquisition parameters were set for the ICCD system, through software (Solis, Andor). The ICCD was set at external trigger mode, i.e., acquisition took place synchronized to external triggers, such as laser pulses. Additional temporal delays were given to the initiation of the acquisition (gate delay), with respect to the arrival of the laser pulses. The integration time, which was the time that the CCD was exposed to the laser pulses, was defined. The time for the ICCD to remain active was defined by the gate width. By controlling the integration time, the number of pulses to accumulate for a single spectrum was defined. For example, if the integration time was set at 20ms, the laser pulse had a repetition rate of 5 kHz, the gate width was 10ns, and the acquired spectrum was the sum of signals from 100 laser pulses, each contributing 10ns acquisition of the signal. In order to collect multiple spectra, the ICCD was set at kinetic series.

Although the gate width can be as low as 5ns, the minimum integration time was limited by the electron transfer rate of the CCD. The transfer rate was the limiting factor for low resolution of LIBS. Even after the clean cycle, which cleanses the CCD after

each acquisition, the maximum frame transfer rate was 62.5 Hz in the external trigger mode.

3.4 Laser systems and routing optics

A microscope objective attached to the stage was moved in a square pattern to cover a region of interest. Relay optics and collection optics were also attached to the stages to be moved along with the objective, which ensured fixed distance between the objective and the optics.

The main consideration for the optics is to have as accurate an axial resolution in the z-axis as possible. A high numerical aperture (0.8) microscope objective was used and the back aperture was completely filled with a beam expander which consisted of a negative lens and a positive lens.

The photons generated and backscattered from the bone included second harmonic photons and auto-fluorescent photons. Also, reflected laser pulses proceed along with those signals generated from bone. Optical filters and dichroic mirrors are used to separate the signals from each other, and also from the reflected laser pulse.

Dichroic mirrors were used to bring in the laser pulses and then to send second harmonic photons to the detector. To further ensure that only the second harmonic photons get collected, a band pass filter with wavelength width of 10nm centered at the emission wavelength, and a filter to cut out laser light were used. All of the collection optics was held by a cage system to make a compact detection module, and this allowed for mounting of the assembly onto the stages. This compactness was also important as

the second harmonic generation detection module was combined with the spectroscopy detection module. The entire assembly was moved along with the microscope objective.

Routing optics parts were carefully selected to deliver the beam effectively, i.e., to minimize the intensity loss and temporal expansion of the pulse. The mirrors and lenses had anti-reflective coating for near infra-red wavelengths. Dielectric mirrors which have coatings for laser pulses with strong intensities were mostly used. From the laser output, the beam first went through the intensity controller, consisting of a half-wave plate and a polarizing beam splitter. Then the beam was sent through a 50-50 beam splitter to share the beam with another setup. Next, the beam was sent to the motorized intensity controller where the half-wave plate was rotated via a stepper motor, which was controlled by a programmable motor controller which drove three other motors for the x-stage, y-stage and z- stage. A periscope was used to bring the beam to the height of the stages, which was mounted on the optics table. A beam expander was used to increase the beam diameter of 3mm to 6mm, in order to fill the back aperture of the objective to fully use the numerical aperture of the objective, which maximized the axial cutting resolution. The beam expander consisted of a negative lens and a positive lens to avoid possible damages to the lens, as the fluence of the focused ablation laser pulse was strong enough to damage the lenses.

For the detection of the spectroscopic light and delivering the signal to a detection device, it was important to consider the most effective ways to configure optics on a single optical axis. First, the emitted light was collected with the same objective that had been used for bringing the laser pulse. Then the signal was passed through a dichroic mirror, which transmitted the emitted light but reflected the incident laser pulse. Finally, a collection lens was used to focus the light into an optical fiber.

In order to collect as much light as possible via fiber, a collection lens was mounted on a micrometer stages to be moved in x-axis and y-axis to precisely focus the emission lights onto the fiber. The fiber was multi-mode with 200µm core diameter and brought the signal to the detection device, the intensified charge-coupled device (ICCD). No additional slit was used for the ICCD as the diameter of the fiber was already 200µm.

The quality of the laser beam delivered to the microscope objective from the optical components was measured, as shown in figure 3.5. The diameter of the beam was approximately 7.5mm immediately after the beam expander. The divergence of the beam effects the resolution of the SHG imaging and laser ablation, and it was measured by comparing the beam divergences at various points in the optical axis. The divergence was 0.5mm over 150mm, and the beam was considered to be well-defined.

3.5 Configuration for second harmonic generation imaging

During the second harmonic generation imaging, the MATLAB code sent commands to the motor controller to move the stages and to open and close the shutter. When the stage was accelerated to a pre-defined velocity, the controller generated a trigger signal to a data acquisition board (NI-6110, National Instruments) to initiate the data acquisition. The rate of data acquisition was defined previously to 5 kHz. When the stages finished their movement, the data was sent to the PC. The MATLAB code then read and analyzed the data to control the next movement of the beam.

In order to interface the data acquisition board through MATLAB code, the data acquisition board was configured and initialized, as shown in figure 3.6. For the synchronization of the data acquisition and the stage movement, the board was operated in the external trigger mode. The PMT signal was directly sent to the board.

When a digital trigger was sent from the set point of the stage controller, the board acquired 5000 samples per second. During the acquisition, no additional triggering to the laser pulses was required. This was due to fact that the Ti-Sapphire laser had a repetition rate of 80 MHz and produced almost continuous signal.

The SHG data was taken by coordinating the movements of motorized stages, data acquisition from the board, by the MATLAB code. First of all, the board started its acquisition in external trigger mode, i.e., the board awaited for the trigger signal from the stages to actually begin the recording. Then the functions to run the stages were called though MATLAB.

The MATLAB functions called pieces of codes that had been written in the stage controller, as shown in figure 3.7. The controller codes were comprised of multiple commands, such as moving the stage in z direction, opening and closing the shutter, sending the digital trigger to the board, and reporting the end of stage movement by generating a byte.

In order to complete the data acquisition, the MATLAB function waited until the stage had finished its run, using a while loop at the end of each function. The while loop kept track of how many bytes were coming back from the stage. Only when there was additional bytes coming back from the stages, which indicated that the stage finished its run, was the function ended. As the acquisition finished after the SHG run, the data was read into MATLAB and the surface position was calculated and recorded. For a typical SHG scan over an area in the sample, the sample was scanned at a point in z then moved to another point to repeat the SHG. At each point, the coordinates of the motor position were measured and recorded for the reference.

When scanning over a large area, the length of the SHG scan was modified based on the SHG signal. If the surface was detected in the middle of the scan, the scan path was identical for the next scan. When the surface was detected below or above the middle part of the scan, the next scan started one step below or above the previous starting position in z. The feedback algorithm is shown in figure 3.8. The x, y steps remained identical for the entire SHG scan.

Calibration of the SHG signal was performed by measuring the thickness of a BBO crystal with a known thickness of 200µm, as shown in figure 3.9. First, the SHG signal was measured with our setup, and then was measured in the previously established laser scanning microscope setup. The thicknesses measured by both setups agreed to be 200µm.

3.6 Configuration for ablation

3.6.1 Optimization of stage parameters per fluence

To efficiently achieve the laser ablation of an area in the skull, stage parameters such as scanning velocity and step sizes were optimized. During the ablation process of making a rectangular cut, the objective was scanned in a raster pattern. The raster pattern was composed of moving the objective quickly in one direction to cover the width of a rectangle, and slowly in the other direction. The focused laser pulses formed a cone-shape, and an overlap in the pulses in the fast axis was required to ensure stable cutting. The overlaps were controlled by adjusting the stage velocity and the fluence of the laser pulse. When the objective was scanned slowly, the overlap increased and much of the ablation was performed on saline, not bone. Also, the LIBS signal was dominated by ablation of water, leading to low signal-to-noise ratio. In the case when the

objective was scanned quickly, the overlap decreased and the bone was ablated insufficiently. The LIBS signal was dominated by ablation of the bone. Therefore, the stage parameters were configured to optimize the ablation rate and spectroscopic signal.

In order to optimize the overlap, the beam profile at the focus was calculated, as shown in figure 3.10.a. The pulse energy defined the volume of the plasma and the material to be removed. The focused laser beam was in the shape of cone, and the fluence decreased as the distance from the focus increased. At pulse energy of 1.6μJ with using 0.8NA objective, the maximum radius which gave fluence above the ablation threshold was 7μm. Therefore the maximum step size was 7μm.

The radius of the focused laser pulse was confirmed by the ablation of the bone. A bone sample was ablated with 1.5J pulses, with steps in the slow axis for guaranteed separation of the pulses, as shown in figure 3.10.b. The width of the ablated streaks was 6μm, which was confirmed with the calculation.

3.6.2 Interpolated move

Once the stage parameters were established for laser ablation, the stages were further configured for the ablation along pre-defined curvature. For ablation along the curvature, the x-stage and y-stage were moved simultaneously. The stage controller was configured to operate at a coordinated move mode. In order to test the coordinated move, the ablation was performed on a glass slide in a circular pattern, as shown in figure 3.11. The laser pulses were separated out in a circular path, as the velocity of the stage was set faster than the laser pulses would overlap at 5 kHz. This confirmed that the coordinated move worked properly.

The coordinated move was further tested for the interpolated SHG curvature. To send commands to the stages, the curvature was sent as an array and downloaded onto the motor controller, as shown in figure 3.12. First, a piece of code was written for the motor controller to define a coordinated move with an array. Then the data from the SHG curvature was sent to the motor controller to define the array. After the SHG curvature was sent to the motor controller, the stage was run according to the curvature, and the optical encoder kept track of the position of the stages. The actual positions of the stages and the interpolated curvature matched well.

During the actual ablation process, the shutter and trigger signals were controlled by the MATLAB code, along with the stage movement. The synchronized shutter control was implemented to prevent damages at the edges. The edges were exposed to excessive amount of pulses as the velocity decreased due to the deceleration during the turn around. The beam was shut off by the shutter at the corners and edges.

After the stage started to move according to the downloaded array from the SHG curvature, the stage movement reached a set point of constant velocity. Then the motor controller sent out a trigger signal to open the shutter to let in the ablation beam. The shutter was closed after moving along a predefined path. The motor controller sent out a trigger signal to the ICCD for synchronized data acquisition, and the triggering result is explained in detail in the next section.

3.7 Settings for laser induced breakdown spectroscopy

For the accurate laser induced breakdown spectroscopy acquisition, the acquisition process was temporally linked with both the stage movement and laser pulses. The synchronization was done by combining the two different signals from the

motor controller and laser pulses, as shown in figure 3.13. As mentioned earlier, the motor controller produced trigger signals which started at the beginning of the stage movement and ended as the stages finished the movement.

In order to obtain trigger signals synchronized to laser pulses, trigger signals that control the Pockels cells were used. The synchronization and delay generator (Coherent, SDG) produced trigger signals for the Pockels cells, which controlled the laser pulses by changing their reflectance. As the repetition rate of the laser was set at 5 kHz, the trigger pulses were produced at 5 kHz as well. The synchronization and delay generator provided adjustable trigger output, which preceded the laser pulses by 90ns at most, giving enough temporal distance between the arrival of the laser pulses and data acquisition. The two trigger signals were combined via a NAND gate (74LS02, Motorola), as shown in figure 3.14. The SDG input was 5khz, 1.5μs TTL pulses train and the gate input from motor controller was TTL pulse synched to the stage motion.

The combined trigger signal was sent to ICCD, which operated at an external trigger mode. The ICCD was configured through the software mentioned earlier. During the ablation, the ICCD was set at kinetic series mode, where repeated measurements were performed for a defined number of times. Typically, a spectrum was obtained per each line in the raster pattern.

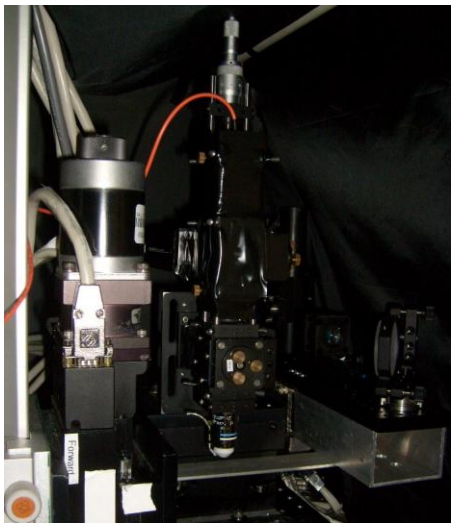

Figure 3.1. Mechanical structure of the setup. The photography of the actual setup shows the stage, motors, and detection optics. The y-stage was mounted on the x-stage and the combined x-y stage were mounted onto the optics table. The beam expander and mirror were mounted onto the x-stage, and was scanned in y-direction only. The PMT, optical fiber, dichroic mirror, filters and microscope objective were mounted onto the x-stage, and were scanned in both x and y direction. Finally, the samples holder was mounted on the z-stage. In order to assemble the stages and mount the optics onto the stages, multiple adapter plates were designed and machined.

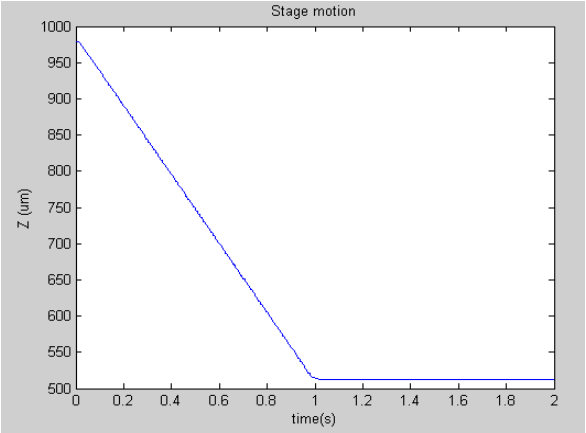

Figure 3.2. Linearity of the stage movement. Reliability and consistency of the stages were tested by measuring the position of the stage during a movement. The stage was driven by the motors to move 500µm with constant velocity. The realtime position of the stage was measured from an optical encoder. As shown in the graph, the stage moved in a linearized motion with a constant velocity for most of the movement. The acceleration of the stage motion was varied when the stage came to a full stop. It is shown that the stage can be moved accurately and reliably, except at the end of the movement, on the order of few µm.

```
#SEG
LM XYZ
I=0
#LOOP1
LI 0,Y[I],Z[I]
I=I+1;
JP #LOOP1, I<=9
LE
VA 100000
VD 100000
VS 24000
BGS
MC YZ;MG {N} "*"
EN
#FWD
OB 1,0;PRX=nx;BGX;WT 10;OB 1,1;WT 35;OB 2,1;WT 160;OB 2,0;WT 70;
OB 1,0;MCX;MG {N} "*";
EN
#SDZ
OB 1,0;PRZ=sz;BGZ;MCZ;OB 1,1;WT 5;OB 1,0;MG {N} "*";
EN
#TES
OB 1,0;OB 2,1;PRZ=ts;BGZ;OB 1,1;MCZ;OB 1,0;OB 2,0;MG {N} "*";
EN
#REV
OB 1,0
PRX=-nx
BGX
WT 10
OB 1,1
WT 35
OB 2,1
WT 160
OB 2,0
WT 70
OB 1,0
MCX
MG {N} "*"
EN
#MTZ
PRZ=tz;BGZ;MCZ;MG {N} "*";
EN
#FTY
PRY=fy;BGY;MCY;MG {N} "*";
EN
#STX
PRX=sx;BGX;MCX;MG {N} "*";
EN
#TTY
PRY=ty;BGY;MCY;MG {N} "*";
EN
#TTX
PRX=tx;BGX;MCX;MG {N} "*";
EN
#STZ
PRZ=mz;BGZ;MCZ;MG {N} "*";
EN
#TTZ
PRZ=dz;BGZ;MCZ;MG {N} "*";
EN
```

Figure 3.3. Codes for motor controller. A snippet of codes is presented as an example. The stage velocity, the distance to be moved, and the various set points were defined through the code. For example, #FWD controlled the x-stage to move in microsteps defined in nx, then after waiting 10ms, the trigger signal to open the shutter was sent out. After a 35ms wait, the second trigger signal for the detection appartus was sent out. After the stage completed its move, the trigger signals were stopped. An asterisk * was issued to notify the end of the #FWD program.

```
% init_s.m
% initialize global serial port object s
% 5-5-2010 ALS
%global s;
s = serial('COM1','BaudRate',115200);
s.InputBufferSize=4960;
s.OutputBufferSize=4960;
fopen(s);
set(s,'RequestToSend','on');
set(s,'DataTerminalReady','on');
set(s,'ReadAsyncMode','continuous');
set(s,'Terminator',':');
```

Figure 3.4. Serial communication between the MATLAB and the motor. The configuration and initialization of the serial communication is presented in the MATLAB code. In order to continue the communication with the controller during issuing of the commands, the ReadAsyncMode was set at continuous in the MATLAB code. The terminator was set to a colon, which was different from the MATLAB default terminator.

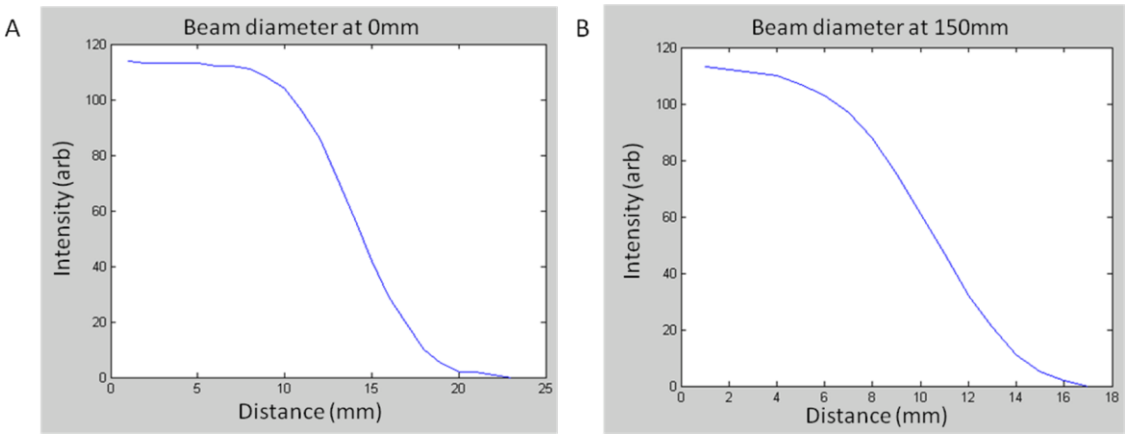

Figure 3.5. Measurement of beam diameter and divergence. Beam diameter and divergence were measured to verify the quality of optics. (A) The beam diameter was measured to be 7.5mm, by taking full-width half-maximum. (B) The divergence of the beam was determined by measuring the beam diameter at different positions in the optical axis. From the measurements, the beam diameter varied 0.5mm over the distance of 150mm. This confirmed that the divergence of the beam provided a consistent imaging condition.

```
%%

AI = analoginput('nidaq',1);
chan = addchannel(AI,1);

duration = 1; %1 second acquisition over full z
set(AI,'SampleRate',5000) %1 kHz = 1ms per sample %10us=100000
%ActualRate = get(AI,'SampleRate');

set(AI,'SamplesPerTrigger',5000)
%set(AI,'TriggerType','Manual')
%blocksize = get(AI,'SamplesPerTrigger');
%Fs = ActualRate;

set(AI,'TriggerType','HwDigital')
set(AI,'HwDigitalTriggerSource','PFI0')
set(AI,'TriggerCondition','PositiveEdge')
set(AI,'TriggerConditionValue',4.5)

%set(AI,'ClockSource','ExternalScanCtrl')
%set(AI,'ExternalScanClockSource','PFI0')
set(AI,'SamplesAcquiredFcnCount',100000)
set(AI,'TimerPeriod',10000)
AI.Channel.InputRange = [-5   5];

```

Figure 3.6. Configuration of data acquisition via MATLAB. The data acquisition board was configured through a MATLAB code. The board was set at hardware digital trigger mode (HwDigital trigger mode), to enable synchronization between the data acquisition and stage movement. Positive edges of the trigger signals were detected, and 5000 measurements were taken per each stage movement. Current generated from the PMT was directly recorded through the board, as the resistance of the board was high enough to act as an I-V converter. As the laser source had repetition rate of 80 MHz, it was regarded as a continuous source and no additional synchronization was installed for the laser pulses.

```
50 -            if scannum>2500
51 -                FTY2
52 -                MZD2 %move in Z,PRZ=PRZ-150,PRY=PRX=0;
53 -            elseif scannum>=2400 && scannum<=2500
54 -                TTZ2
55 -                FTY2 %typical move,PRZ=zstep*imax;PRY=Y,PRX=X;
56 -            else
57 -                MZU2 %move in Z, up
58 -                FTY2
59 -            end
60 -            TD2
61 -            end
```

Figure 3.7. Feedback control of SHG scans. Each stage movement was written up as a separate function. After reading the each SHG scan, depending on the position of the bone surface, the SHG path was modified or stayed at the original path. For a modified path, the scan path was raised up (MZU2) or raised down (MZD2). The position of the stages was read out after each SHG run.

```
%%
% <2>-1 Fitting ztotf with polyfit - find coefficients
zcurve1t=zcurve1.';
COEF2=zeros([10,5]);
for n=1:10
    COEF2(n,:)=polyfit(X,zcurve1t(n,:),4);
end
%%
% <2>-2 Fitting ztotf with polyfit - find values
zcurve2t=zeros([10,10]);
for n=1:10
    for i=1:10
    zcurve2t(n,i)=COEF2(n,1)*X(i)^4+COEF2(n,2)*X(i)^3+COEF2(n,3)*X(i)^2+COEF2(n,4)*X(i)+COEF2(n,5);
    end
end
zcurve2=zcurve2t.';
%%
for n=1:100
    %SHGnet(:,n)=SHGraw(:,n);
    for i=1:5000
        if SHGnet(i,n)>= 0.5*max(SHGnet(:,n))
            break
        end
    end
        fn(n)=i;
        for j=1:5000
            if SHGnet(5001-j,n)>=0.5*max(SHGnet(:,n))
                break
            end
        end
        rn(n)=5001-j;
end
```

Figure 3.8. SHG data analysis in MATLAB codes. Bone curvature obtained via SHG was curve-fitted and interpolated. The first segment shows the 4th order polynomial fitting. The second segment shows the linear interpolation for the curves. Finally, the thickness of the bone was determined from the SHG using a full-width half-maximum calculation, as shown in the last segment.

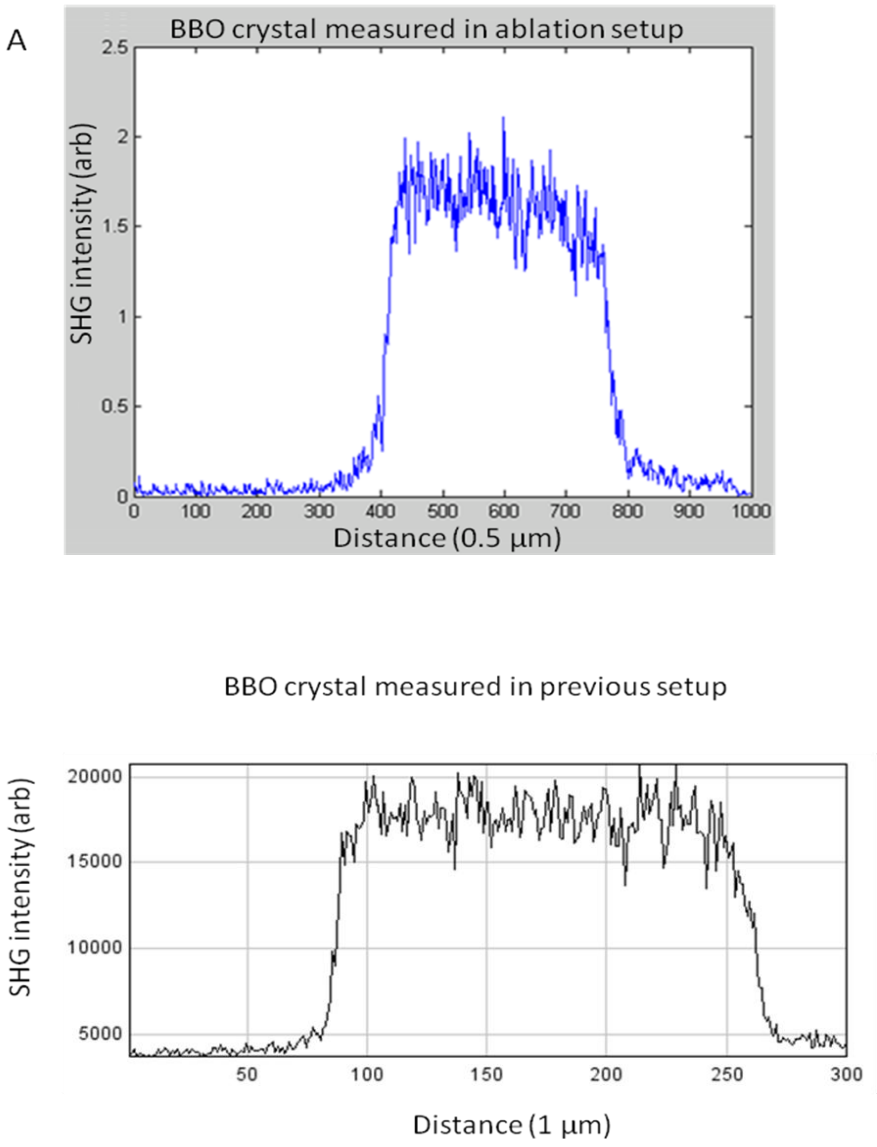

Figure 3.9. Calibration of SHG signal with BBO crystal. BBO crystal of known thickness of 200µm was imaged. The crystal was imaged with SHG in two different setups: the ablation setup (A) and the previously established laser scanning microscopy system (B). Both measurements gave 200µm, confirming the consistency of the SHG measurement performed in the ablation setup.

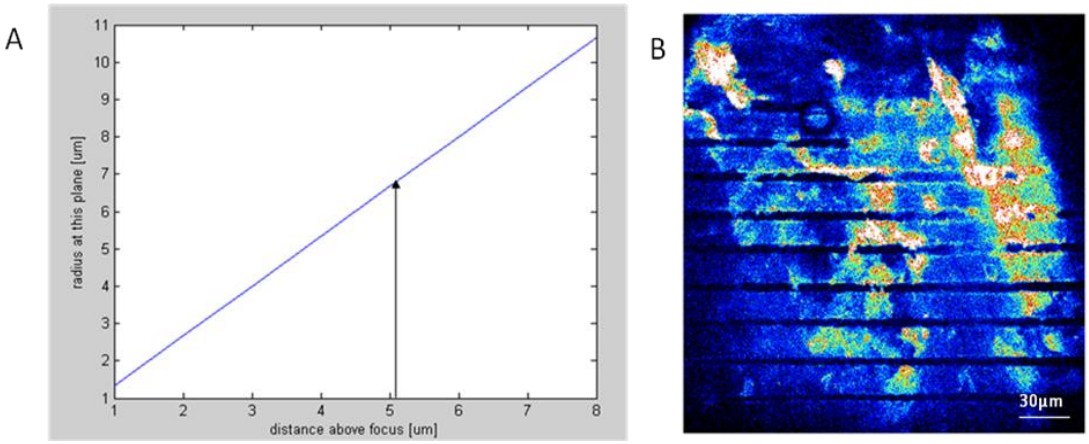

Figure 3.10 Optimization of stage parameters per fluence. (A) The diameter of the pulse was calculated for the optimization. When a laser pulse of 1.6µJ is focused down, the radius of the beam increased linearly as the distance from the focus increased. The fluence decreased as the diameter increased. The black arrow indicated the maximum radius before the fluence fell below the threshold for ablation. (B) A bone sample was ablated and imaged with two-photon microscopy to experimentally determine the pulse sizes. The beam radius was measured to be 6µm for 1.5µJ pulses.

A

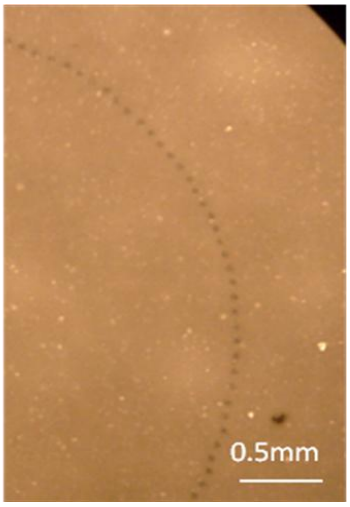

B

```
for repn=1:250
    ind=250*(znum-1)+repn+1;
    TD2

    fwrite(sp1, uint8('DM Y[99];'))
    fwrite(sp1, uint8('DM Z[99];'))
    for nx=1:99
        fwrite(sp1,uint8(['Y[',num2str(nx-1),']=',num2str(YcommandLI(nx,repn)),';Z[',num2str(nx-1),']='
    end
    while sp1.BytesAvailable < 200
        continue
    end
    %pause(0.1)
    fread(sp1,sp1.BytesAvailable);
    fwrite(sp1,uint8('XQ #SEG8;'))
  while sp1.BytesAvailable < 2
        continue
  end
    %pause(0.1)
    fread(sp1,sp1.BytesAvailable);
    fwrite(sp1,uint8('XQ #TTX;'))
    %fwrite(s,uint8('XQ #ST7;'))
```

Figure3.11. Coordinated movements of the motorized stages. Stages were operated in coordinated move mode for ablation along the curvature of the skull. (A) The coordinated move was tested in a glass slide. The ablation path was defined to be a circle and the stage was driven at a high speed to spread the pulses out. As shown in the figure, the ablation took place in a circular pattern with 2mm diameter. (B) To drive the stages along the curvature of the skull, the SHG curvature was downloaded onto the motor controller as an array. Then the predefined function in the motor controller was initiated to move the stage according to the given array. The array was given by the differences of position in the skull curvature, as the stage was driven in relative coordinate mode.

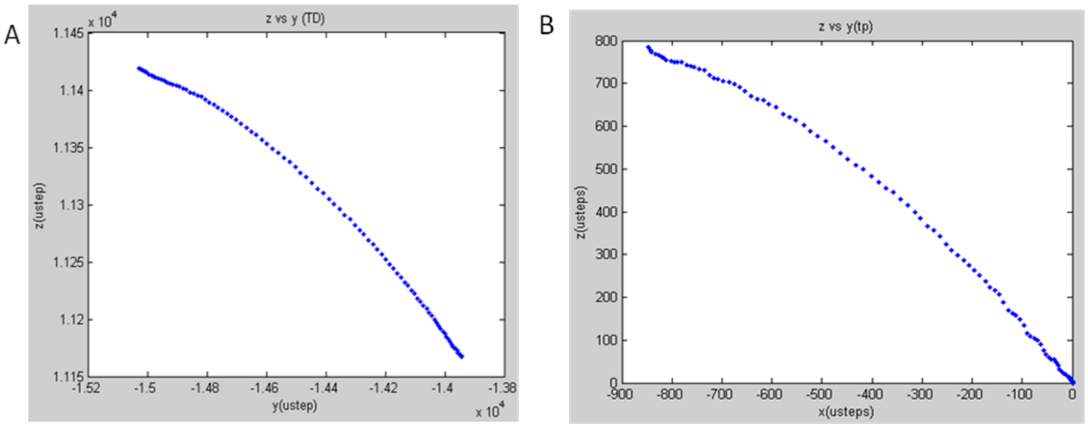

Figure 3.12.Verification of coordinated move. The SHG curvature was given to the stages as a command. As an example, a single trace was selected from a previously interpolated curvature to perform the measurement. The commands given to the stages is shown in (A). The actual position of the stage was measured during the movement as shown in (B) It was possible to conduct the coordinated move reliably, as confirmed by comparison of the two traces.

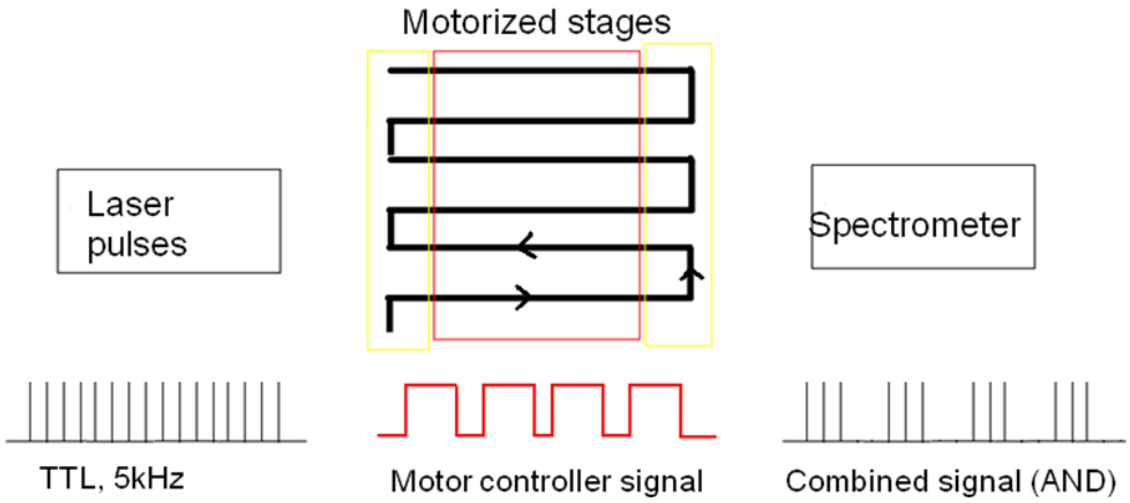

Figure 3.13. Configuration of trigger pulses for synchronized data acquisition. Trigger pulses were configured for data acquisition synchronized to both the stage movement and laser pulses. First, trigger pulses at 5 kHz were obtained, which were used for controlling the Pockels cells. These trigger pulses were directly locked to the laser pulses. The trigger pulses were combined with trigger signals (red) produced from the motor controller. As the stages were accelerated and reached a constant velocity, a trigger signal was turned on. When the stage decelerated, stopped, and turned around for the next scan, the trigger signal was turned off. The two trigger signals were combined to produce bursts of trigger pulses. The combined trigger pulses were sent to the spectrometer and spectra were collected only during the stage movement, and each measurement was locked to laser pulses.

A

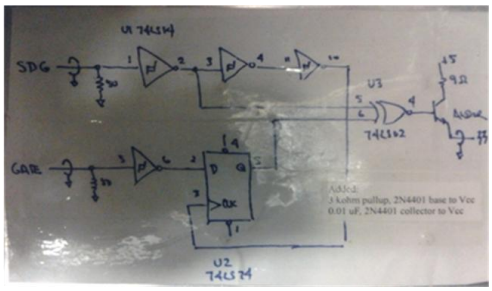

B

Figure 3.14. Summation of trigger pulses from multiple sources. The trigger pulses from the motor controller and laser system were combined via a custom-made circuit (A). The delay added by passing through additional electronics was minimized by selecting fast chips. An AND gate (LS7402, Motorolla) was used for adding up the trigger pulses. The delay added to trigger pulses were 35ns. Signal interface was configured in standard BNC cable (B). The assembly of the circuit was carried out by A. Schweitzer.

Chapter 4. Methods and the protocols for *in vivo* cranial surgery

In this chapter, we provide detailed procedures for making an *in vivo* thinned skull window and obtaining *in vivo* imaging through the thinned skull window. The animal preparation and surgical methods are described, and then the configuration of the setup is discussed. Optical surgical procedures are presented, along with the imaging preparation and procedures. Immunohistochemistry and imaging of the brain slices are discussed. Finally, a checklist for the entire experimental steps is presented.

4.1 Protocols

4.1.1 Sample preparation

Ex vivo skull samples were taken from C57BL6 mice that had been euthanized with a 3 gram per kg body weight dose of pentobarbital (Fatal Plus). The extracted skulls were post-fixed by immersion in 4% PFA overnight. The periosteum was removed from a fixed skull, and then the skull was thoroughly dried. The dried skull was attached to a glass slide to fix its position.

4.1.2 Surgery prior to thinned skull procedures

Male C57BL6 mice from Jackson Labs, over 25g in weight were used. Animals were anesthetized with 0.2 mL of 0.2% (W/V) chlorprothixene, followed by 0.2 mL of 10% (W/V) urethane. The head of each mouse was shaved and an incision was made along the midline of the scalp after analgesia by injection of lidocane. The skin was retracted to expose the skull, and the periosteum was removed by scraping with a surgical blade. The skull was dried with a cotton applicator prior to applying a thin layer

of cyanoacrylate to the bone. To indicate the starting position of the window, a point in the skull was marked. Grip Cement (Dentsply) was applied to the skull to attach a metal head stage frame to it. Cement was also applied around the perimeter of the central opening in the head stage in order to adhere a custom well dish. The custom well dish consisted of a small petri dish (351008, BD Falcon) with a 5mm diameter hole in the bottom, and a draining port drilled in the side and fitted with a tubing adapter. The central hole in the well dish and head stage provided optical access and direct flow of phosphate buffer solution (1M) to the skull. An aquarium pump was used for circulation of the saline.

4.1.3 Laser systems

Multiple femtosecond laser systems were used for efficient imaging and ablation of the sample. Second harmonic signals were generated with femtosecond pulses from a Ti:Sapphire laser system (Mira, Coherent Inc.), which provided an 80 MHz train of 100 fs pulses with wavelength of 800nm and had maximum average power of 2W. Laser ablation was performed with femtosecond pulses from a regenerative amplifier laser system (Libra, Coherent Inc.), which provided a 5 kHz train of 100 fs pulses with wavelength of 810nm and had maximum average power was 1W. Lastly, for two photon laser scanning microscopy, a Ti-Sapphire femtosecond laser system (Mira HP, Coherent) was used. The wavelength range was at 800nm, maximum average power was 1W with repetition rate of 80 MHZ. The temporal width of the laser pulses were 150fs.

4.1.4 Optics

<u>Ablation optics</u>

To control the intensity of the ablation laser beam, a half-wave plate (10RP52-2, Newport) was coupled to a stepper motor (42BYGH404-R, Jameco) and rotated for the desired intensity. The beam exposure onto the sample was controlled by a shutter (LS3, Uniblitz) that was driven by the motor controller.

A set of routing optics were mounted onto translational stages. A beam expander comprised of a negative lens and positive lens (ACN254-050-B and AC254-100-B, Thorlabs) was used for the expansion of the beam to fill the back aperture of the microscope objective. The filters and dichroics were mounted onto a cage system (Microbench, Qioptic) into 1 inch cubes. A primary dichroic (700DCXRU, Chroma) was used for the transmission of the laser pulse to the sample and blocking the laser pulse reflected off the sample. The beam expander and a folding mirror were mounted onto the x-stage to maintain alignment with respect to the microscope objective. A water dipping microscope objective (LUMPLANF, Olympus) was used for both focusing the laser beam onto the collection of signal. The microscope objective and dichroic mirror were mounted onto the y-stage for simultaneous scanning and emission detection.

Second harmonic generation optics

For SHG setup, additional optics components were installed onto the ablation optics setup. As the optical axis was shared between two different sources, a flip mirror was for switching between the ablation beam and Ti-Sapphire laser beam for SHG imaging. An additional beam expander built with two positive lenses (AC254-502-B and AC254-100-B, Thorlabs) were installed to further expand the Ti:Sapphire laser beam. For the isolation of the second harmonic signal from the laser beam and auto-fluorescence of the bone, a secondary band pass dichroic mirror (ZET40s, Chroma) and

a filter(BG 39, Schott) were installed. For the detection of the SHG signal, a photo-multiplier tube (H7422-40, Hamamatsu) was used. To maintain the optical alignment during the scanning, the dichroic mirror, filter and the photo-multiplier tube were mounted onto the x-y translational stages.

4.1.5 Motorized stage system

To scan the beam across the sample, the microscope objective was steered by translational x-stage, y-stage (XYR-6060, Danaher) and z-stage (LMB-600, Danaher). To minimize the vibration, the z stage was mounted onto the optics table separate to the jointly mounted x-stage and y-stage. The lead screw pitch was 508μm for x-stage and y-stage and the z-stage was run on a 2mm ball screw. The minimum travel for the stages was 0.3μm. To read out the positions of the stages, a set of optical encoders were installed onto the stages. To steer the stages, a set of stepper motors (42BYGH404-R, Jameco) were connected to the stages. The speed of the stage motion for cutting was modified with different laser pulse energies, and at 3uJ pulse, the stages were driven at the speed of ~4mm/s. A motor controller (DMC-4040, Galil) sent out commands to the stepper motors to drive the stages. The controller was connected with a MATLAB algorithm in the PC via RS-232 communication.

4.1.6 Computer algorithm for temporal synchronization and feedback control of SHG

In order to perform both SHG imaging and laser ablation with a micrometer precision, the temporal coordination and synchronization of the multiple experimental procedures, such as data acquisition and beam control, were required. A MATLAB algorithm controlled the entire experimental sequence from the initialization of the data acquisition to the data analysis and feedback control from the analysis. When the code

was initiated, the stages started the movements to steer the microscope objective. The motor controller was configured to send out a TTL pulse to the shutter when the stages reached a constant velocity after the initial acceleration. Also, another TTL pulse was generated from the controller which was sent to the data acquisition (DAQ) board (NI 6110, National Instruments) to initiate the data acquisition.

To minimize the time it takes to perform the SHG scan on the bone, a feedback algorithm was installed. After acquiring the second harmonic trace, the MATLAB algorithm calculated the precise position of the surface from the measurement. If the surface position was significantly higher or lower than the center of the scanning path, the scanning path was adjusted for the next scan accordingly. This feedback control allowed efficient scanning with 500μm scanning path over the surface position ranged up to millimeters. With the above settings, the scanning of a single point in bone took about 2 seconds.

4.1.7 Fabrication of thinned skull window

Animal preparation

The prepared animal was place on a heating pad to maintain constant body temperature. The animal was then secured onto the optics table via the attached head stage, and the exposed skull was placed at the focal plane of the microscope objective. To remove air bubbles from aggregating at the surface of the microscope objective, custom-shaped metal tubing was attached to the objective. The opening of the tubing was directed towards the focal point of the objective to remove the bubbles created from laser ablation under water. A pump was submerged in a saline reservoir on the table to generate a continuous flow of saline across the front surface of the objective through the

attached tubing. The saline accumulated in the well dish and was drained out through the exit port, which recycled the saline to the reservoir.

SHG scan

The curvature of the bone was captured using second harmonic generation scanning. An area of skull was scanned with resolution of 200μm in both x and y and 0.1μm in z. The laser pulse energy was 2nJ. Then the raw second harmonic generation data of the skull was processed to obtain a smooth cutting path. The data points were fitted with 4^{th} order curve fitting for smoothness. Then by using linear interpolation method, the resolutions in x and y were increased to 5μm.

Laser ablation

A MATLAB algorithm was configured to send the processed curvature to the motor controller. The three dimensional curvature was split into multiple two dimensional curves in x-z plane and the y was incremented in a fixed step. For each laser ablation sequence, the 2D curve was sent to the stages in an array. The motor controller was configured to operate coordinated moves which involved the simultaneous steering of the x-stage and y-stages. After the stages begun their moves and approached a constant velocity, the shutter opens to pass the laser beam through for the laser ablation. When the x-z stages finish their moves, the shutter closes and the y-stage moves in a fixed incremental step. Finally, when the entire plane of skull was removed according to the curvature, the x and y stages returned to their initial positions while the z-stage was lowered down with a fixed step for the ablation of the next plane in the skull. The laser pulses with 3uJ were used. The cutting steps were 5μm in x and y, 8μm in z. The

thickness of skull was measured via second harmonic generation after the laser ablation to obtain feedback.

4.1.8 Preparation for *in vivo* Imaging

After the thinned skull window was created, the thinned skull window was dried then a thin layer of cyoanoacrylate was applied to attach a 2mm by 2mm piece of #0 cover slip (Ted Pella) onto the window. To stain blood plasma for visualization of vasculature, 0.05ml 10% fluorescein dextran (70kDA, Sigma) was retro-orbitally injected to the mouse.

4.1.9 Two-photon laser scanning microscopy

Laser and optics

For *in vivo* imaging, a previously configured two-photon laser scanning microscopy setup was used. A femtosecond Ti:Sapphire laser system (Tsunami, SpectraPhysics) tuned at 800nm was used as a source. For focusing of the laser pulse and collecting emission, a microscope objective (LUMPLANF, Olympus) was used as a lens. The optics components used in the TPLSM was mounted onto the cage system (Microbench, Qioptiq). A primary dichroic mirror (700DCXRU, Chroma) was used for both sending laser pulse into the microscope objective and to isolate signal from the laser pulse. A photo-multiplier tube (R6357, Hamamatsu) was used for the detection apparatus. Filters (E680SP-2P, Chroma) were used for isolating only the signal into the PMT. A lens (PAC025, Newport) was used for focusing down the emission signal onto the PMT.

Scan mirrors and translational stages

To image over a region of the sample, the laser beam was scanned over the region with a pair of scanning mirrors. The alignment was maintained during the scanning procedure by using the telescope lenses (AC254-050, Thorlabs). In addition to the scanning of the laser beam, translational stages systems (Danaher) were used for moving the sample to image over different regions in the sample. The stages were driven by a set of stepper motors (Vexta PH268M-M1.5, Herbach and Rademan Company) that were controlled by a motor controller (DMC-4040, Galil).

Software

A software platform (MPScope) previously written in Pascal was used for controlling data acquisition and hardware interfaces. Through the software, the scanning mirrors were controlled by the parameters such as rate of the scanning, dwell time per each pixel and size of the scanned region. The signal obtained from the PMT was analyzed by the software, and combined with the information on the position of the scan mirrors, the image from the sample is retrieved. The position of the translational stages was controlled through the software. The laser intensity was controlled by the software, using a servo motor to rotate the wave plate.

4.1.10 Imaging and analysis of vasculature and blood flow

In vivo imaging of the vasculature and blood flow was performed with two-photon laser scanning microscopy. Stacks of images were collected from a volume of 500µm by 500µm in x and y and 200µm in z from the microscopy. The collected images were further analyzed with MATLAB and ImageJ for median filtering and intensity adjustments.

An algorithm (Arbitrary Scanning) previously written in MATLAB was used for measurement of the blood cell movement in a blood vessel. The Arbitrary Scanning algorithm allowed for selecting the scanning region, and only the regions along the vessel and across the vessel were scanned through the algorithm for obtaining vessel diameter and blood flow velocity. The blood flow analysis was carried out through a Radon transformation and spectral analysis to calculate the velocity of the blood flow.

4.1.11 Histology

After *in vivo* imaging, the animals were perfused with 3% para-formaldehyde (PFA) and then their brains were extracted and immersed in PFA overnight. Next, the brains were immersed in 30% sucrose for 2 days for cryoprotection. The brains were frozen to -20C then slices of 50µm were obtained by a microtome. The slices were stained with 1:100 diluted primary anti-body of GFAP (Invitrogen) for the detection of glial activation due to significant damages to the neurons and vasculature. NeuN (Invitrogen) and MAP2 (Invitrogen) were diluted to 1:100 and used for visualizing the neuronal cell density and processes, respectively, to find possible damages to the neurons. Then, the slices were further stained with secondary anti-body of Alexa 594 (Invitrogen) and Alexa 488 (Invitrogen) for to tag the primary anti-bodies with dyes for fluorescent imaging.

4.2 Checklist for optical surgery

A detailed checklist for performing the *in vivo* automated surgery is provided to articulate the specific orders of the various tasks which were required for the surgery. The experiment was terminal, and the animal was perfused at the end of each imaging session.

1. Measure the weight and record the age of the animal
2. Make anesthesia solutions (urethane and chloroprothixane)
3. Injection of anesthetic solution after initial anesthesia from isoflurane
4. Turn on the chillers and lasers (Libra, Mira, and Tsunami)
5. Wait for the animal to go be anesthetized (supplement injection if needed)
6. Make a bath of phosphate buffered saline
7. Shave head of the animal
8. Inject lidocane into the scalp
9. Remove scalp and periosteum
10. Dry the exposed skull and apply cyanoacrylate glue
11. Make a fiducial to mark the sight to make the window
12. Attach the metal frame with cement glue
13. Attach plastic container onto the metal frame
14. Wait until the cement is fully dried
15. Final preparation for the measurements, check the alignment and start various software
16. Mount the animal onto a designated mount
17. Carry the animal over to the laser rig and connect to the heat pad

18. Connect the tubing to the plastic container and initiate the saline flow

19. Roughly align the animal so the window can be made near the fiducial, by using sodium plasma dot created in the saline from the laser pulse

20. Detect the surface of the skull and place the focus well above the skull

21. Switch to SHG beam and check the intensity of the laser beam

22. Set parameters to following: 2 X 2mm, 200µm resolution, triggering of data acquisition through motor controller, shutter, feedback controlled scan

23. Start SHG scanning

24. Calculate the curvature obtained from SHG

25. Protect edges by raising the curvature

26. Reposition the stage to the starting point

27. Adjust laser pulse energy to ablation parameters

28. Spectrometer (ICCD) triggered by laser pulse with pre-defined delay setting and gate width

29. Resolution of the spectroscopy set to one line per spectra, 200lines per plane, with 5µm steps in y

30. Start laser ablation

31. Continue ablation until the intensity of the calcium peaks bounces back from the decrease from spongy layer in skull which contains blood vessels

32. Reposition the stages to be 200μm above the current cutting plane to center the SHG scanning in z

33. Measure skull thickness by SHG measurement

34. Repeat the ablation and SHG imaging until the average thickness is ~20μm or less

35. Continuously monitor PBS level and refill the reservoir

36. Take out the animal from the rig

37. Inspection of the window under the microscope: there should be no bleeding, and the window should be transparent enough to see the vessels through the window

38. Dry the skull

39. Apply cyanoacrylate glue and cover slip

40. Retro-orbital injection to introduce dyes to the blood plasma in the vessel

41. Supplement anesthesia, if needed

42. Set up filters in the two-photon laser scanning microscopy setup for the dye used in injection

43. Check alignment of the two-photon laser scanning microscopy system

44. Adjust wavelength, mode-locking, and intensity of the laser

45. Set scan parameters

46. Image with 10x objective to obtain the overview of the window

47. Select the region of interest from 10x overview, and image with 40x objective

48. Obtain z stack with maximum averaging for vasculature imaging

49. Blood flow measurement through arbitrary scan (at least 3minutes of data is required for spectral analysis)

50. Take the animal out of the rig

51. Euthanasia

52. Perfusion with PBS

53. Perfusion with paraformaldehyde

54. Extract the brain and skull

55. Fix the brain and skull overnight in paraformaldehyde

56. Cryoprotect the brain by submerging the brain in sucrose until the brain sinks

57. Slice the brain tissue into 50µm slices

58. Stain with primary antibody

59. Rinse brain slices

60. Stain with secondary antibody

61. Mount the slices onto glass slides

62. Fluorescent imaging of the processed brain slices

Chapter 5. Realization of automated cranial surgery and *in vivo* imaging of brain

In this chapter, the results leading to making the thinned skull window is presented. First, the nonlinear optics techniques are applied to bone, and the results are discussed. Each of the nonlinear optics methods will be used as a building block for the automated cranial surgical experiment. For the automated, optical thinned skull surgery, the skull was first scanned to obtain its curvature then was thinned with laser pulses. Once the thinned skull window was created, the brain tissue was imaged through the window. The viability of the brain tissue was assessed by using antibodies those marked the damages to the neural tissue.

5.1 Double pulse laser-induced breakdown spectroscopy

5.1.1 Signal drop in LIBS under aqueous environment

For biological experiments, it is important to keep the sample wet in order to maintain a suitable environment for the tissue to stay viable. In surgeries, saline is used to wash away debris and blood. The ions in saline create a more hostile environment for plasma expansion, as the dynamics of plasma evolution that has been created under water is quite different than that of in the air. To be more specific, the signal from the emission from the plasma evolving under water drops, compared to the plasma emission in the air, due to the interaction of the plasma and the water molecules surrounding it [106].

When created under water, the plasma is disturbed by the water molecules, as the water dipoles are electrically charged. Also, the emission peaks are broadened due to pressure from the water molecules, as shown in figure 5.1. It is shown that the emission signal produced from the samples in the air has a strong signal-to-noise ratio, with multiple peaks. On the other hand, the emission peaks from the samples submerged under water are significantly lower in signal to noise ratio, and the peaks are severely broadened to the point that the peaks are not distinguishable from each other. Also, the continuum generation from the emission under water is much stronger than that of in air.

5.1.2 Background on double pulse for signal enhancement

As mentioned earlier in Chapter 2, double-pulse LIBS with nanosecond pulses experiments have been performed, and significant increases in the signal to noise ratio in both ablation in air and under aqueous environment have been reported. The main idea is to split a laser pulse into two, and then to delay one pulse in time so that the second pulse can interact with various by-products created by the first pulse. Different phases of the plasma evolution can be targeted by adjusting the inter-pulse delays. Significant signal enhancement by the double pulse experiments are reported to be in all cases of nanosecond LIBS in air [104], nanosecond LIBS under water [110], and femtosecond in air [111].

While a definitive theoretical explanation is not yet provided to explain the signal enhancement, several mechanisms are hypothesized to account for the enhancement of the signal. Depending on the temporal delay between the split pulses, the mechanisms

can be divided into the following categories: laser-plasma interaction, plasma-plasma interaction and plasma expansion in more air-like environments.

The laser-plasma interaction takes place when the temporal delay for the second pulse is relatively short, and thus the plasma created by the first pulse is energized by the second laser pulse. For the plasma expansion mechanism, the targeted inter-pulse delay is much longer. The first laser pulse creates a plasma bubble, while the second pulse is delayed until the plasma expands to become more like an air bubble as it cools down. The second pulse then interacts with the sample within the plasma bubble created by the first pulse. Now, the plasma created by the second pulse can be expanded in the same place where the first bubble had created a space for it to expand freely [115].

Double pulse experiments of the femtosecond LIBS under water have not been reported yet, and we tested the idea of signal enhancement via laser-plasma interaction. Ideally, the signal enhancement from the air-like plasma expansion will produce stronger effects, but the laboratory space was limited to generate adequate delay for the laser pulse. The radius of the plasma created underwater is reported to remain constant in the time window from 100ps to 10ns, and then the plasma expand exponentially afterwards [71]. We targeted the inter-pulse delay where the plasma is still 1μm for the laser-plasma interaction.

5.1.3 Double pulse setup

To implement the double pulse setup for the femtosecond LIBS under water, a Michelson interferometer with variable delay was constructed on the optical table (figure 5.2). Polarizing beam splitters were used to split the pulse into two, and then to spatially combine the pulses after the second pulse had been delayed. The temporal delay for the

second pulse was adjusted with two routing mirrors mounted onto a micrometer stage. The two laser pulses were aligned to the accuracy of 5 micro-radians (less than 1mm divergence over 3 meters distance), to bring the pulses together for maximizing the laser-plasma interaction. Since the dimensions of the plasma were on the order of $1\mu m^3$ with laser pulse energy of 1μJ, this precision allowed for spatial overlap of the second pulse onto the plasma, ensuring the interaction between the two.

5.1.4 Double pulse result: spectra from saline and bone

From the double pulse setup, significant increases in the signal from emission under water were observed for both sodium emission from phosphate buffered solution (PBS) and calcium emission from the bone. (figure 5.3) Amplified laser beam with a temporal width of 150fs and a 5 kHz repetition rate was used for the light source. With the laser pulse energy of 0.8-1.6 μJ, the delay between the pulses was set in the range from 0.2-0.5ns, which agreed with the temporal regimes of the plasma evolution at the pulse energy. In the case of the sodium emission at 588nm from the PBS, the emission spectra from the double pulses were much longer in time as well, and the signal was significantly enhanced compared to the single pulse emission.

The calcium emission from the bone submerged in PBS was obtained with the identical double pulse setup and laser pulse conditions, as shown in figure 5.4. Compared to the single pulse measurement, the double pulse LIBS produced clear emission peaks with an enhanced signal-to-noise ratio and with increased resolution of the emission peaks at various wavelengths. As shown in the figure, the emission peaks from the double pulse setup contained several distinguishable calcium peaks at 399nm,

420nm, and 450nm, whereas only the peak at 420 nm was detectable from the single pulse emission.

5.1.5 Calibration Data

The spectroscopy signal was calibrated and characterized from the NaCl solution and the $CaCl_2$ solution with varying concentrations. To make solutions with varying concentrations, solid NaCl and $CaCl_2$ were weighed and dissolved into double-distilled water. The solutions were buffered to pH7 to eliminate the pH factor from the results. In the case of measuring the signal under water, the objective was submerged in the circulating solutions to avoid bubbles accumulating on the objective. For measurements in air, the position of the objective was adjusted until the focused laser beam interfaced with the surface of the solution. The light was delivered in double-pulse mode, then the signal was collected via ICCD spectrometer in time-resolved mode. For the ICCD spectrometer, the gate delay was increased with increment of 1ns, and a gate width was set to be 5ns per each trace. After the acquisition, the initial broadband spectrum was discarded and only the emission peaks were taken into consideration for an accurate comparison of emission peak intensities, as the duration of the broadband emission varied from concentration to concentration. For this comparison, solutions were ablated in air as well.

As shown in figure 5.5., the signal-to-noise ratio monotonically increased as the concentration increased in air, for both the sodium emission and calcium emission. The peaks were overlaid with different colors assigned to different concentrations. As the concentration was increased, the intensity of the emission increased and the trend of

increasing signal continued until the strongest concentration. The peak intensity exhibited exponential increase with increasing concentration.

On the contrary, the signal to noise ratio increased only up to a certain concentration then decreased, in the case of ablation under aqueous solution for both calcium and sodium emission, as shown in figure 5.6. Not only did the signal drop, but also the durations of the emissions also reduced significantly. The logarithmic plot shows there was a sharp turning point at the concentration 250mM in both sodium chloride and calcium chloride. The exact mechanism behind the decrease of the signal is not identified yet. However, the drop in signal with higher concentration levels suggests that other properties of the solutions, such as the viscosity of the solution or the density of ions in the solution, could play a role in the emission of the plasma.

Furthermore, calcium peaks from various materials have been obtained as a reference to later compare them with the emission peaks from bone (figure 5.7.). Solid, insoluble materials those contain calcium, in this case calcite and chalk, were submerged under PBS and then ablated with laser pulses to obtain LIBS signals. For both chalk and calcite, spectra with calcium peaks at same wavelength were observed, and also agreed with spectra from ablation of bone.

5.1.6 Spectra of tissue vs. bone

Now that the calibration and characterization of the LIBS have been established, spectral emission from tissue and bone were measured to be used as a means to distinguish bone from tissue. As plasma emission peaks are specific to the elements of the sample being ablated, it is possible to utilize the emission signal for distinguishing bone from soft tissue in automated surgeries. Previous works done in air with *in vitro*

samples clearly show different peaks in bone versus soft tissue [94]. Although both tissue and bone contain calcium, we expect to obtain a stronger signal from bone as its calcium concentration is on the order of several moles, which is significantly higher than that of the soft tissue [134].

The emission spectra obtained from bone contained multiple, clearly distinguishable calcium peaks, whereas the emission obtained from tissue only exhibited a sodium peak (figure 5.8). The spectra was obtained from bone and tissue submerged under saline, and continuous flow of saline was provided by a pump.

Emission peaks from soft tissue were obtained from the same experimental setup and parameters. Only the peaks from sodium were observed in the case of the soft tissue. Spectra obtained from the tissue showed a peak at 589nm only, which corresponded with the sodium peak. When compared with the peaks from saline ablation, the two spectra matched well.

As the emission spectra from tissue is distinctively different from that of bone due to calcium emission, it was confirmed that the spectral lines can be used for distinguishing bone from soft tissue. In the following sections, the spectral response was utilized as a feedback signal during the laser ablation, to control the ablation process in order to remove only the skull from the surrounding brain tissue, which is very close to the skull.

5.2 Plasma-mediated laser ablation

5.2.1 Ablation calibration

The accuracy and precision of femtosecond plasma-mediated laser ablation was measured by ablating glass slides with different pulse energies. The femtosecond plasma-mediated laser ablation can be precise as mentioned earlier in the chapter, and the calibration of the double pulse laser ablation was required to confirm in the custom made setup. The glass slides were ablated with the same fluence but with different step sizes, and then imaged with femtosecond two-photon scanning laser microscopy (TPLSM). The TPSLM provided adequate resolution in both lateral and axial directions. The ablated glass slides were submerged under fluorescein bath to provide contrast.

As shown in figure 5.9., as the step sizes were increased, the smoothness of the ablated surface increased as well. The surface roughness was on the order of 3-4 µm for 5 µm steps, 1 µm for 2.5 µm steps, and less than for 1 µm step. The surface roughness from ablation was caused by the optical cavity, or stage vibration could also have been a cause for such irregularities. With the lowest step size of 1µm, the surface was smoothest.

The measurements suggest that it is important to smooth and index match the surface for an optically smooth surface suitable for imaging. Although the lowest pulse energy provided the smoothest ablated surface, the step sizes were smallest and the ablation speed was slowest. For surgical preparations, the speed of the ablation was important and with the pulse energy at 3µJ, it takes 2 minutes to ablate a 2x2 mm square, which was too slow to be applied to *in vivo* experiments. Thus it was strategic to ablate with higher pulse energies since those pulses allowed for speedy ablation and also smooth the surface. The smoothing and index matching can be done by applying cyanoacrylate glue to fill in the grooves on the surface of skull, then by putting a cover

slip onto the area. When tested on the ablated glass slide, the rough surface regions were optically smooth after the procedure.

5.2.2 Preliminary ablation data

After the laser ablation was characterized in glass slides, the laser ablation was tested on biological samples, as shown in figure 5.10. First, an *ex vivo*, paraformaldehyde-fixed rat skull was ablated with the amplified laser pulses in squares of varying sizes. The size of squares varied by 50µm, and the step size in z was 50µm as well. The intrinsic curvature of the rat skull was not taken into consideration, and the laser beam was scanned parallel to the optics table. The ablated squares exhibited sharp corners.

Furthermore, the ablation was tested over the suture line in an *ex vivo* rat skull and showed the successful removal of bone without damaging the structure of the skull during the ablation. Traditionally, the suture lines were avoided for the cranial surgery, as the mechanical tools applied forces onto the fragile suture lines. As the laser ablation does not apply pressure during the removal procedures, bone can be ablated in fine patterns near and on the suture line.

The ablation capabilities were further tested in an *ex-vivo* mouse skull with the brain and dura attached to the skull. As shown in the figure, the ablation was precise enough to remove only the bone and not damage the sagittal sinus and part of the dura. These examples demonstrate the preciseness of the laser ablation and the control capacities of the laser ablation in bone.

Finally, the ablation was tested in *ex-vivo* soft tissue from a mouse. A square patterned volume in the soft tissue was successfully removed without rupturing the tissue nearby. With mechanical tools, generally, it is not possible to ablate soft tissue without disturbing the surrounding tissue as the brain tissue has high content in water and has mechanically weak structure. However, with laser ablation, it was possible to gently and precisely remove soft tissue in sharp square patterns without tearing the nearby tissue.

5.2.3 LIBS and ablation

Now, the next step was to perform laser ablation on bone with spectral feedback from LIBS, as shown in figure 5.11. First, the calcium emission from bone was processed to determine the ablation of the bone, versus ablation of saline or soft tissue which were represented by the sodium emission. As shown previously in figure 9, the calcium peak at 422nm was used for obtaining the criteria to identify the ablation of bone. The ratios were taken from the intensity of the 422nm peak versus that of the 500nm region where both the calcium and sodium emission peaks were absent. When the ratio was lower than 1.3, the spectra was regarded as lacking calcium peak, thus the spectral signal was not from bone.

To test the accuracy of the criterion, a skull sample with a square hole that had been previously ablated was used. A square pattern that was concentric to the hole was ablated, and the LIBS signal was taken simultaneously. The resolution was 5μm for the fast axis and 20μm for slow axis. When the calcium peaks were present at an ablated spot, the spot was indicated as a red dot. On the other hand, when spectrum from a position was without calcium peaks, the position was represented as a blue dot. As

shown in the figure, image reconstruction by this red/blue determination from the spectral signal faithfully matched the dimension of the hole. Thus it was possible to accurately detect the LIBS signal and utilize it for controlling the precise ablation of the bone.

Next, the feasibility of the thinning of the bone along the curvature was tested by using the laser induced breakdown spectroscopy. The main idea was to first map the surface of the bone, and then define the ablation paths along the mapped curvature of the skull. Then using coordinated movements of the stages, the ablation was performed along the skull. The precision of the ablation was tested by taking LIBS measurement during the ablation, as shown in figure 5.12.

First, the surface of the skull was identified and the objective was located such that the ablation started well above the bone. In this stage, as the PBS was ablated, the spectra contained sodium peaks only (figure 5.12.a.). As the objective is lowered step by step and the focus reaches the surface of the skull, the ablation of bone was initiated. As the ablation process proceeded down the z axis, the calcium peaks started to appear. The calcium LIBS signal indicated ablation of bone, and compared to the previous plots, every single line contains calcium peaks (figure 5.12.b.). This confirmed that the SHG mapping was accurate at least in the lateral direction and the ablation was initiated along the curvature of the skull.

The calcium LIBS signal disappeared and the sodium signal re-appeared at the last scan. From the first plane, LIBS data was continuously taken during the ablation scan process. The calcium signal was continuously present in all of the trace, meaning that the bone was ablated at every single pass. In the second to last scan, the calcium

lines start to disappear, indicating that the skull has been fully ablated. Finally, in the last scan, the calcium peaks fully disappear, confirming that the entire plane in the skull was completely ablated. As the vanishing of the calcium peaks took place over only two last planes, the accuracy of the ablation along the curvature was approximately 10μm.

The discrepancy of the disappearing of the calcium peaks can be from the difference in the curvature between the top surface and the back surface of the skull. Although the bottom surface was not taken into consideration, the discrepancy was on the order of 10μm, indicating the skull thickness to be quite uniform across the plane. The accuracy of the ablation along the curvature could be improved by measuring the bottom surface and updating the ablation path on a real-time feedback control. Another source of error could be from the low resolution of the SHG imaging, as the resolution of the SHG was maintained at a lower resolution to minimize the time spent for SHG imaging.

It is noteworthy to mention the resolution and speed of the LIBS procedure. The minimum unit for ablation was determined by the laser intensity, and measured to by $1\mu m^3$, and the minimum detection for LIBS with the setup was on the order of 10 pulses, i.e., the resolution was limited by the detection sensitivity of the ICCD used for LIBS detection.

The speed of the detection was limited by the transfer rate of the ICCD camera, and was too slow to be applied to *in vivo* experiments. The slower speed came from the fact that it took more time for ICCD to take more spectral data due to the transfer rate of the CCD pixels. Also, the transferring of the data to the PC and processing them added

additional delays. In order to fully apply the LIBS to ablation, it would be necessary to speed up the ICCD data acquisition and data processing.

5.3 Second harmonic generation from bone

5.3.1 SHG of tissue vs. bone

Although precise ablation with resolution of 5μm was proved to be possible by utilizing the LIBS, the technique is inherently disruptive, i.e., even though the volume is confined to $1\mu m^3$, the volume has to be ablated in order to perform the spectroscopy. To address this issue, a non-invasive imaging technique has been adopted for imaging and range-finding the skull. As mentioned earlier, second harmonic generation (SHG) can be utilized for this purpose as it is a nonlinear optical phenomenon from the intrinsic property of bone that allows optical sectioning within the bone.

To successfully apply SHG to a skull which was closely spaced to connective tissue and brain, we compared the SHG intensities produced from the brain and skull. We focused on the intensity of the SHG as the wavelengths were identical for both bone and brain, at half of the incident beam. With the same laser intensities and parameter settings, the SHG signals were obtained from brain tissue and skull. As shown in figure 5.13, the intensity of the SHG produced from the bone was much greater than that of the SHG produced from the soft tissue. Therefore, it was possible to utilize SHG signal to probe the geometry of the skull even when the skull was close to the brain tissue.

5.3.2 SHG mapping of skull and thickness measurement

In order to precisely control the thinning of the skull, quantitative measurement of the geometric profile of the skull was required. As a means to detect the position of the

skull surface and determine the skull thickness at a particular lateral position, the second harmonic generation signal from an intact bone was measured as a function of the axial position of the focus relative to the preparation, as shown in figure 5.14. As the focus enters the top surface of the skull from above, the SHG signal rapidly increases to maximum value. As the focus is lowered into the skull, the signal decays exponentially due to scattering in the opaque bone. If the thickness of the bone is greater than ~50 micrometers, then the gradual exponential decay of the SHG signal continues to drop to background levels, which is the case for the intact bone. If the skull is thinner than ~50 micrometers, then the SHG signal exhibits a sharp transition as the focus is lowered past the back surface of the skull. The half maximal position on the rising edge defines the absolute height of the top surface of the skull at this lateral position. The full-width-at-half-maximum of the curve provides a lower limit on the thickness of the skull. To illustrate the measurement of the bone thickness, a measurement from a previously thinned bone sample is presented in panel B, with its thickness being 20μm.

The SHG measurement at a single lateral position was further extended and applied to measure the curvature over a region of skull, by conducting multiple SHG scans over the region. The curvature of the top surface of a skull was measured with SHG to obtain and visualize the intrinsic curvature of the skull. A 10 X 0.4mm region of the skull was scanned sagittally in a grid-like pattern, as shown in panel C, with lateral step size of 200μm and axial resolution of 0.1μm. The skull curvature obtained from the SHG scan exhibited an arc-like curve with a decrement of ~1500μm in z over the 1cm lateral width of the skull, which was in agreement with the typical ranges of the physical dimensions of a mouse skull.

The accuracy of the SHG measurement of the skull curvature was further assessed by comparing against the conventional bright-field imaging of the skull. The cross-section of the skull along the scanned region was obtained by mechanically cutting the skull sample, which was previously scanned with SHG. The cross-section was dyed with fluorescein to enhance the contrast for the bright-field microscopy. The overlay of the wide-field measurement and the SHG contour map is shown in panel D. At the edges, the curvatures were no longer captured as the laser pulse was obstructed by the edge due to the NA of the objective, and also as the slope of the edge became much narrower than the NA.

5.4 Automated i*n vivo* cranial surgery to make thinned skull window

5.4.1 *In vivo* SHG mapping of skull as guidance for thinning process

The resolution of the curvature was increased from 200μm to 5μm by linear interpolation, to accommodate the fine step size for cutting with regards to the fluence of the laser pulse. The skull was thinned in a grid-like pattern by steering the stages along the curvature, with a shutter synchronized to the stage movement to control the laser beam. The pulse energy was 3μJ at the focus and the step sizes were 8μm in all three axes. The SHG scanning was used intermittently during the laser ablation, to measure the thickness and the contour of the thinned portion of the bone, which in turn provided information for control of the laser ablation process.

The thinned skull window was examined by using SHG to measure the dimension and the thickness of the window obtained by laser ablation. By scanning over the same region as prior to the laser ablation, the top surface of thinned skull window is visualized, as shown in figure 5.15. From the intact bone, ~350 depth of bone was

removed and the window was cut in a square pattern with dimensions of 1.8 X 2 mm. The thickness of the skull was measured over the window via SHG, as the thickness was within the detection range of the SHG scan of the bone. The statistics of the thicknesses of the skull over the window had a median value of 24μm, which was within the range of skull thicknesses for the conventional thinned skull window, as shown in panel D.

5.4.2 Thinned skull window

After the setup for SHG-LIBS-ablation had been established for *ex vivo* skull samples, the technique was applied to *in vivo* experiments. For performing the *in vivo* surgery, it was critical to find a way to fix the mouse head for stably defining the optical axis and plane. To address this issue, a metal plate was designed and attached to the mouse skull, using dental cement. A custom made well was attached onto the metal plate was to hold the PBS and its flow (for washing away debris and blood) without leakage. The plate and well assembly were mounted onto metal post to firmly fix the animal onto the table, as shown in figure 5.16.

A typical window made *in vivo* is shown in panel B, and the thinned skull window had increased transparency and allowed more vessels to be seen even with the naked eye. The position of the window was typically over the motor cortex, near the saggital suture line. The bleeding from bone was minimal, except at the edges where the vessels running through the bone were exposed. Again, from the precise ablation, the shape of the window was sharply square.

In vivo tissue ablation was also tested to see the damaging effect of the laser ablation to the tissue. Even with the flow of saline, there were bleeding from the vessels

in dura and brain. When the brain was extracted, no significant staining was observed. The viability of the tissue was further assessed by immunohistochemistry. The microscopy photos show (panel C) clear removal of soft tissue by laser ablation. GFAP showed activation of the glial cells due to the damages to the neurons, MAP2 showed the process of the neurons, and NeuN showed the nuclei of the neurons. From the histological data, the damages to the brain tissue from the laser ablation appeared minimal. Further investigation is necessary to obtain conclusive evidence. However, the results suggest that the damages to the brain tissue which can be caused from ablation of the bone were minimal, at least for acute animal preparation.

5.4.3 LIBS profile of bone

LIBS profile was obtained across the planes during the laser ablation. Although the high resolution LIBS imaging during laser ablation was developed, it was not feasible to utilize the full imaging capabilities during *in vivo* surgery due to the time duration, as time was the critical factor in the *in vivo* surgery. Instead, LIBS signal was measured line by line in the planes and then the signals were averaged to a single value that represented the plane. The profile of the intensity of LIBS signal of the calcium peak can be obtained, as shown in figure 5.17.

The intensity profile of the calcium peak revealed the structure within the skull. When the ablation was started well above the bone, the intensity of the calcium peak was at minimum, indicating that the ablation was mostly done in the PBS. As the focus approached the surface of the skull, the intensity of the calcium peak increased. The ablation continued into the porous region of the skull, which contained blood vessels. In this region, the intensity of the calcium peak decreased as the density of bone

decreased. After the porous region had been ablated away, the intensity was recovered to the higher values from the ablation of the second dense layer, which had similar density compared to the first layer.

The LIBS profile provides efficient ways to save time until the porous region was ablated away. The porous region was difficult to be measured with SHG as the thickness can be very thin at one point while thick at other points. Also, it would be time-consuming to repeat SHG scanning after each ablation pass. Thus it would be logical to utilize LIBS profile as the existence of the porous region in the skull is known *a priori*. The SHG scans were not necessary until the signal bounces back, i.e., the ablation of the second thick layer had begun.

5.5 Assessment of quality of thinned skull window

5.5.1 Blood flow and vasculature imaging through the thinned skull window

For *in vivo* imaging in the brain, the scattering from the thinned skull window needs to be minimized in order to maximize the imaging depth in the scattering brain tissue. To verify that the optical quality of the window was sufficient for *in vivo* imaging of the brain, the vasculature in the cortex was imaged with the two-photon laser scanning microscopy. A 300 X 300 μm region within the thinned skull window was imaged plane by plane with 1μm steps, to obtain stacks of images which provided information in x, y, and z. The z projection of the images over different imaging depths of 150μm and 200μm (figure 5.18.a and b) showed clear images of vasculature including arterioles in the lateral direction, up to 200μm deep in the cortex. The projection of the images in x-z and y-z direction visualized the vertical structures of the vasculature, including the blood

vessels descending into the cortex. The thinned skull window allowed for clear imaging in both lateral and vertical directions, up to 200μm deep in the cortex.

5.5.2 Immunohistochemistry

Another way to examine the optical transparency of the thinned skull window is to perform blood flow imaging, as fine resolution is required to image the movements of individual red blood cells. An arteriole in the vasculature within the thinned skull window was selected and imaged for blood flow measurements. The scanning path was defined along the blood vessel in order to measure the movements of the red blood cells as they were individually imaged (figure 5.18.c). The velocity of the blood flow was determined from the slope of the red blood cells within the arteriole and the spectral analysis of the velocity was performed to measure the mouse heart rate of 8 Hz, which was well within the normal physiological range (figure 5.18.d).

To confirm that the brain tissue was intact and viable after the *in vivo* laser surgery and imaging, the immunohistochemistry was performed on the brain tissue, using markers to visualize possible damages and cell death (figure 5.19.a). The brain slices stained by GFAP markers visualized glial activation (figure 5.19.b). Compared to the contra-lateral side as a control, the region of the brain under the thinned skull window showed that no significant damages occurred to trigger the glial activation. The NeuN and MAP2 markers were used for visualization of the neuronal cell density and neuronal processes, respectively (figure 5.19.c and 5.19.d). In comparison to the contra-lateral side, the brain tissue that was under the thinned skull window showed comparable level of cell density and similar preservation of neuronal processes.

5.5.3 Imaging of microglia in CX3CR1 mice

Transgenic CX3CR1 mice were used to verify that the damages to the tissue during ablation and the microglia were viable and that the processes were well preserved, as shown in figure 5.20. With the recent development of transgenic mice, several mouse lines were genetically modified to have specific cell types that are fluorescent. The CX3CR1 mouse line has microglia cells labeled with enhanced green fluorescent protein (eGFP) [135]. After the thinned skull was made in the CX3CR1 mouse, the blood vessels and microglia were imaged. The vessels were stained with Texas Red (Life Technologies) which had a distinct emission line from the eGFP labeling of the microglia. The blood vessels were imaged through the thinned skull window along with the microglia. The magnified images of the microglia shows that the processes were intact and the microglia activation had not been observed. After extraction of the brain, the slices were obtained and imaged. The glial activation levels in the control and in the window were comparable, further confirming the viability of the microglia and neurons after the laser ablation surgery.

5.6 Preliminary data on electrode arrays

One of the applications utilizing the precise removal capabilities of laser ablation is to make arrays of holes in the skull. Currently, in order to insert an electrode array [136], the entire region of the skull needs to be removed, which is inefficient as more of the skull is removed than necessary. To address this issue, we attempt to create micro-holes via laser ablation, instead of full craniotomy, as shown in figure 5.21.

To visualize the electrode holes, a conventional hole drilled with a mechanical dental drill was compared with an array of electrode holes made with laser ablation. The holes were space 250μm from each other with the diameter of the holes were 200μm.

As shown in the figure, even the smallest drill bit of 500μm was much larger than that of the laser-created holes. Thus, it is shown that the laser ablation could provide efficient ways to create holes and preserve the skull, which can be useful as more intact skull could provide more support for the electrode arrays and more protection for the brain tissue.

An array of holes was made *in vivo* in channel rhodopsin [137] mouse, and the fiber optics was inserted to excite the cells. The channel rhodopsin mouse line has optogentic neurons, i.e., neurons that can be activated by applying light on to them. We activate the neurons by delivering light to the neurons from fiber optics. The holes were made to fit the 200μm fiber that was connected to the blue light source. When the holes were made, the bleeding was observed as through-holes had to be made to insert the fiber. The fiber delivered the light into the cortex, and through one of the other holes, an electrode was inserted to record the firing of the neuron when excited by a light source. The setup was provided by Dr. Per Knutsen. The histology showed damages to the brain from the electrode array insertion.

To more accurately make electrode arrays, it is critical to increase the resolution of the SHG and the sensitivity of the ablation. It would also be important to define parameters for optimized ablation of the hole, as making through-holes without damaging the tissue underneath involves more delicate ablation and detection techniques.

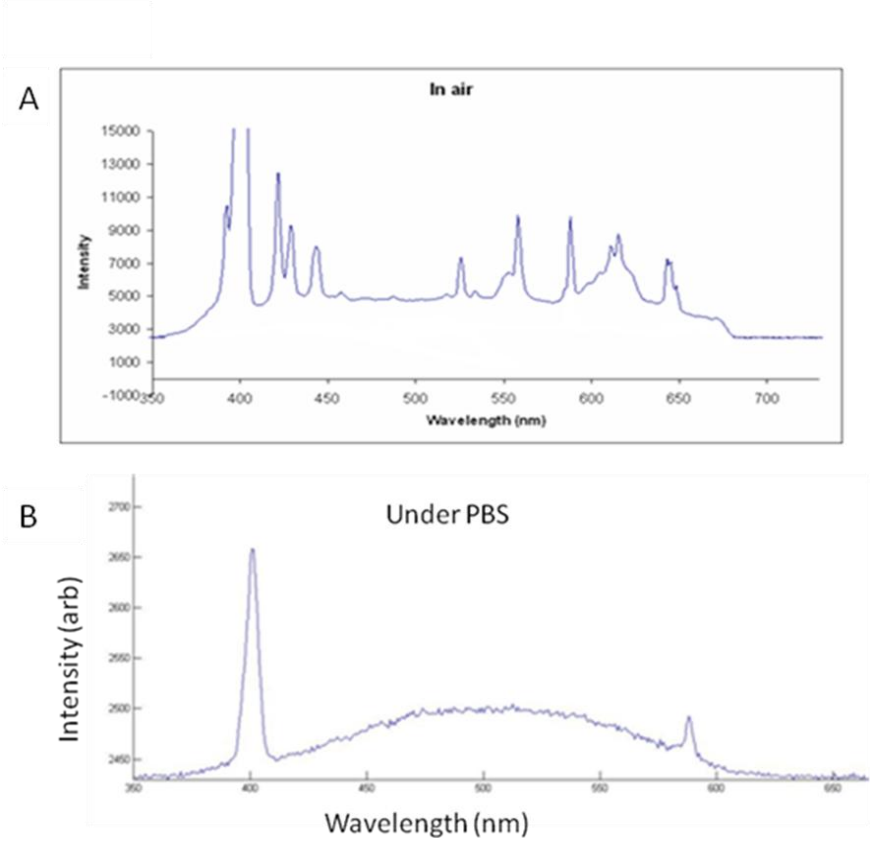

Figure 5.1. Decrease of LIBS signal in aqueous environment. (A) LIBS from ablation of bone in air. Multiple distinct calcium peaks were obtained, with high signal-to-noise ratio. Peak at 400nm is second harmonic generation. (B) LIBS from ablation of bone under phosphate buffered solution. The spectra contained only sodium peaks, without significant calcium peaks. The peak at 400nm is second harmonic generation from bone.

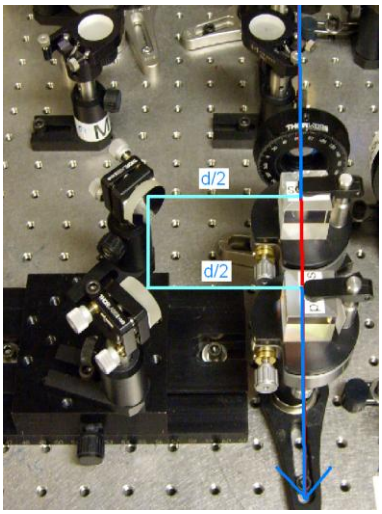

Figure 5.2. Double pulse setup. The amplified beam (in blue) was split into two beams through the first polarizing beam splitter. The wave plate adjusted the intensities of the orthogonal polarizations. The split-pulse with vertical polarization passed through the beam splitter (in red). The split-pulse with horizontal polarization was reflected from the beam splitter and routed through the delay line, comprised of two routing mirrors and a micrometer stage (in light blue). The temporal delay added by the delay line ranged from 0.2ns to 0.5ns. For most experiments, 0.3 ns delay was used. Two beams are merged after the delay line through the second beam splitter. The beams were aligned to ensure that they overlap at the focus.

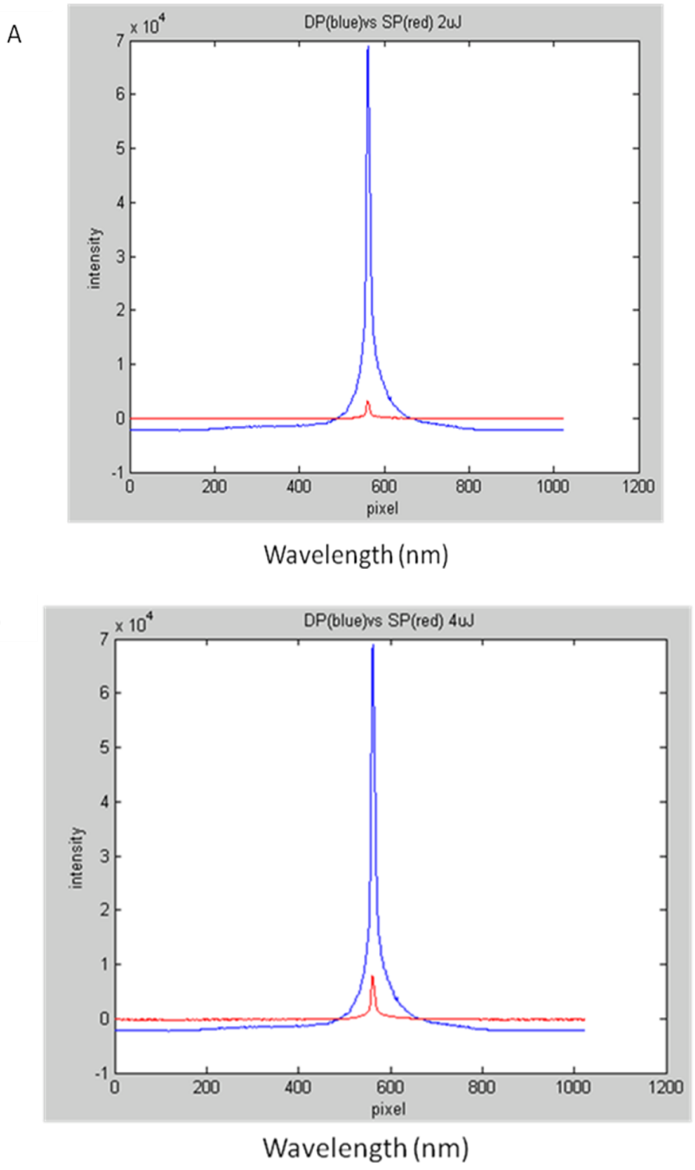

Figure 5.3. Signal enhancement from double pulse LIBS: sodium peaks in saline. (A) The double pulse setup enhanced the signal of LIBS under phosphate buffered solution (PBS). With the pulse energies 2uJ and with delay of 0.3ns, the signal was enhanced by 10 fold with double pulse setup. (B) With the pulse energies of 4uJ and with a delay of 0.3ns, the signal was enhanced by factor of 5 by double pulse.

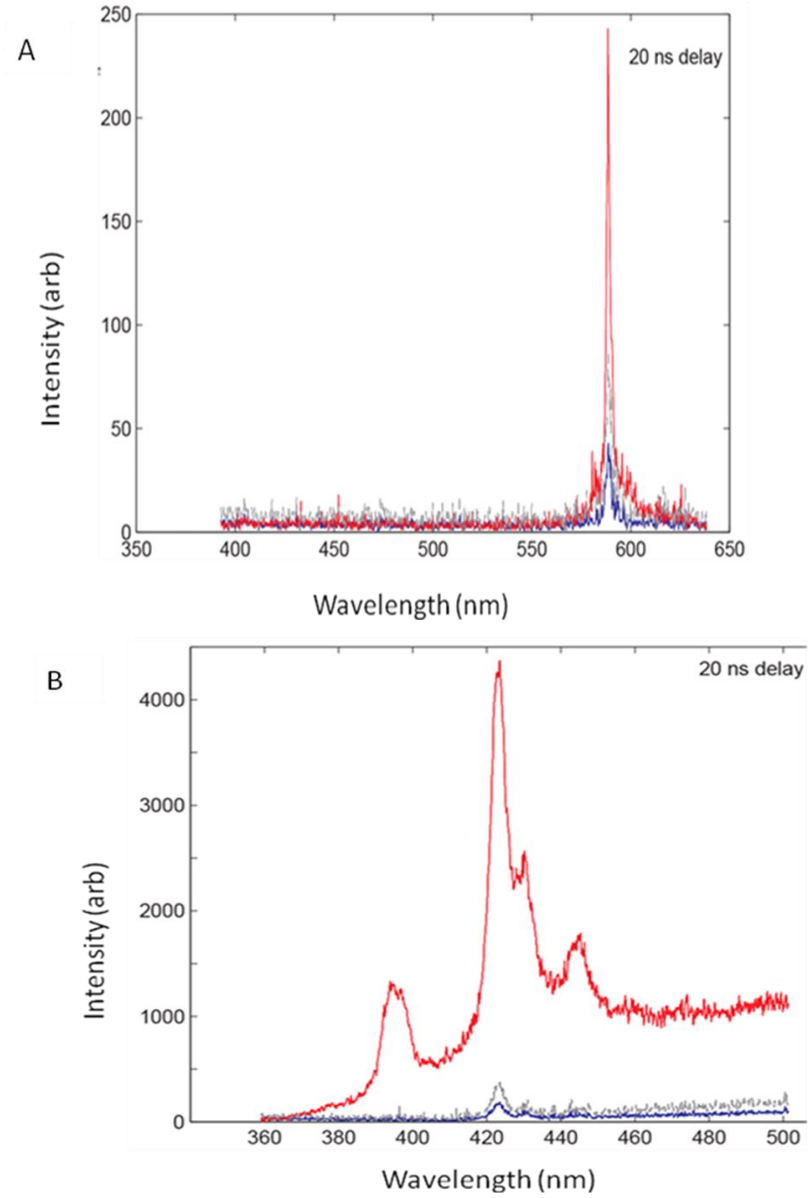

Figure 5.4. Signal enhancement of emission from bone from double pulse LIBS. Double pulse enhanced the emission signal generated under saline. Both PBS (phosphate buffered saline) and bone were ablated by the moving beam from the microscope objective, which was steered by motorized stages. (A)The sodium peaks are presented for the control, and they showed enhancement of 2.5 fold. (B) Spectra from bone. The intensity of the signal was enhanced significantly with the double pulse setup (red), compared to single pulse (blue). Also, the number of distinguishable peaks increased. With the double pulses, the peaks at 396nm, 422nm, and 443nm from calcium were clearly visible, whereas in the single pulse setup the SNR was too low to see the peaks.

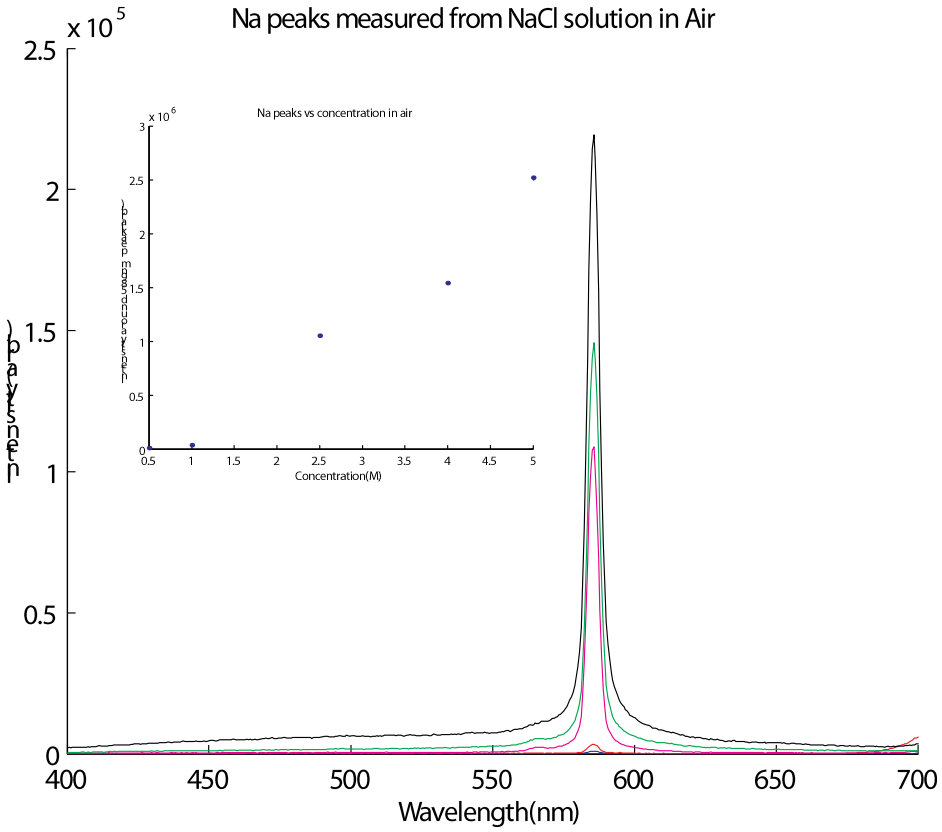

Figure 5.5. Measurement of LIBS signal from NaCl solution in air. The signal intensity of the sodium peak at 588nm increased as the concentration of the solutions was increased.

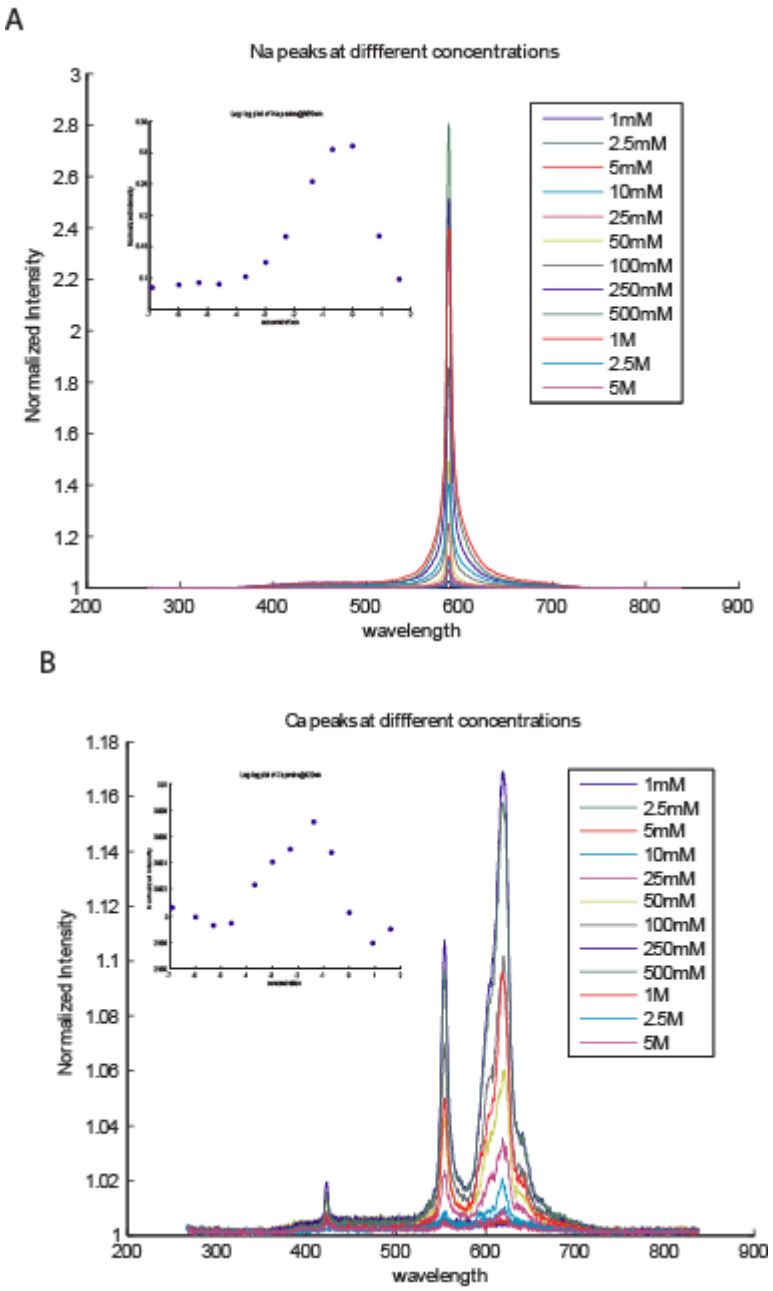

Figure 5.6. Measurement of LIBS signal from solutions. The LIBS signals varied as the concentration levels of the solution changed. For the LIBS obtained under water, the intensity of the signal increased until 250mM, and then decreased afterwards. Both the intensities and durations of the signals decreased after the set point at 250mM, and the decreases were observed in both sodium and calcium solutions.

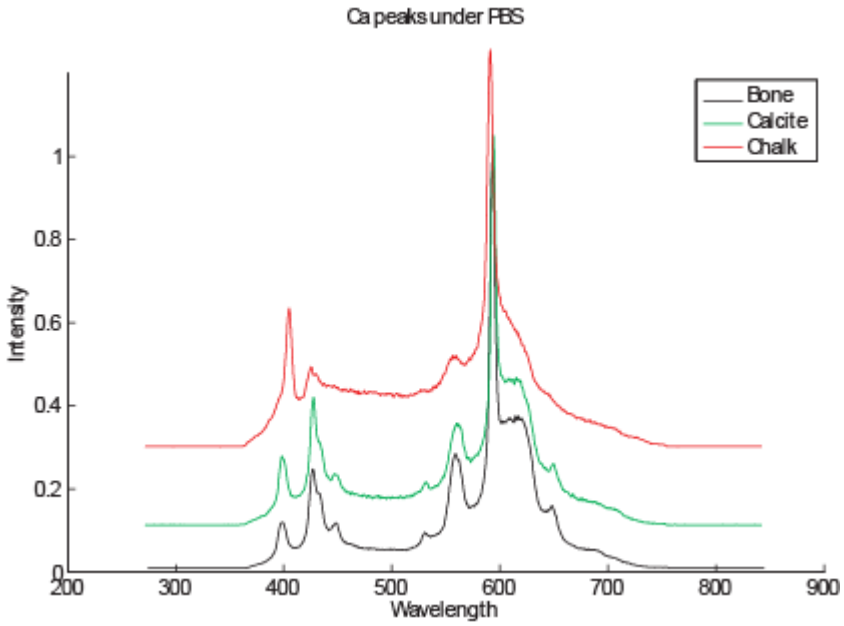

Figure 5.7. Measurement of calcium spectra from different materials. The spectra were obtained under PBS, from solid materials containing calcium. In both chalk and calcite, calcium peaks were obtained. These were used as a reference to verify the LIBS signal obtained from bone.

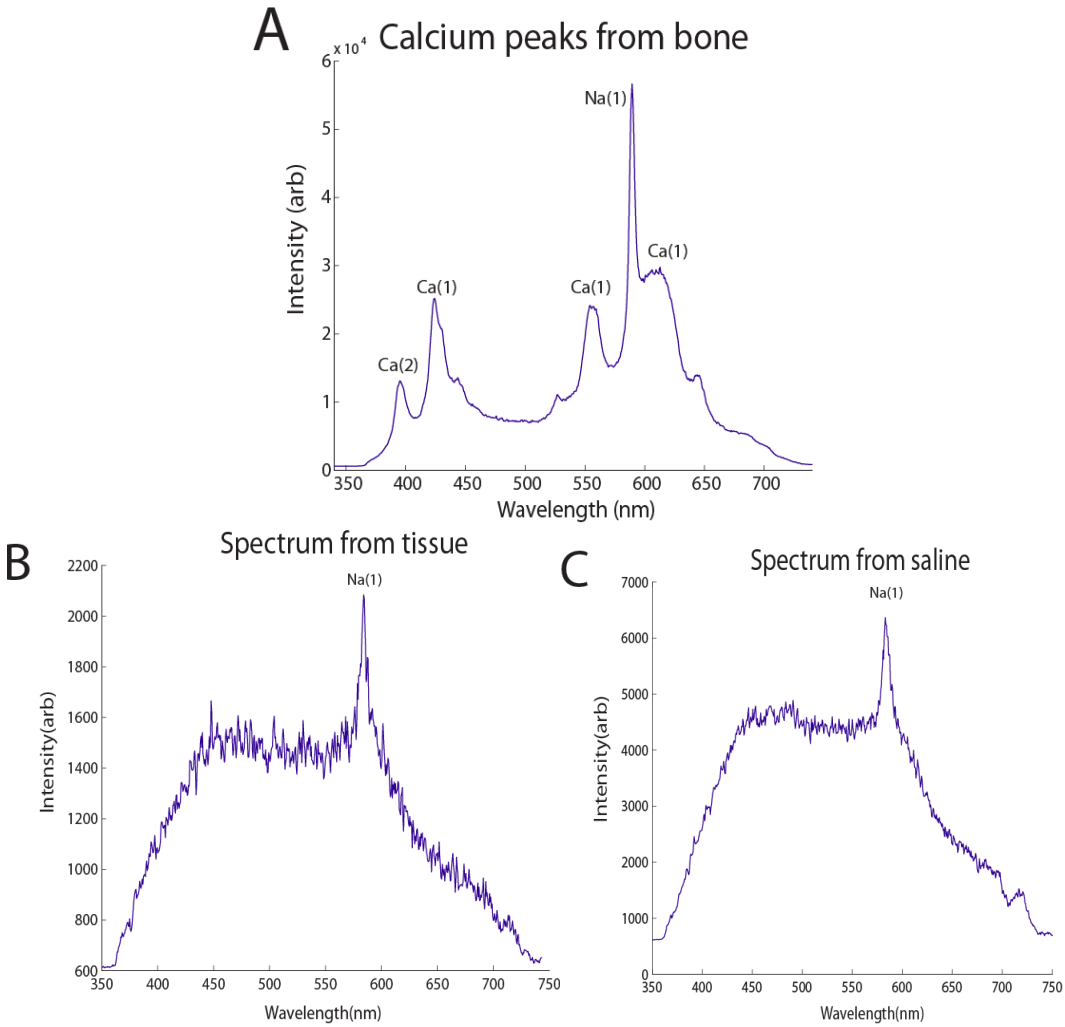

Figure 5.8. Comparison of calcium emission from bone and tissue. (A) Calcium peaks were detected from bone in LIBS measurement while only sodium peaks were observed from tissue. (B) Spectrum obtained from brain tissue contained sodium peaks, without significant calcium peaks. (C) Spectrum obtained from saline is presented as a control.

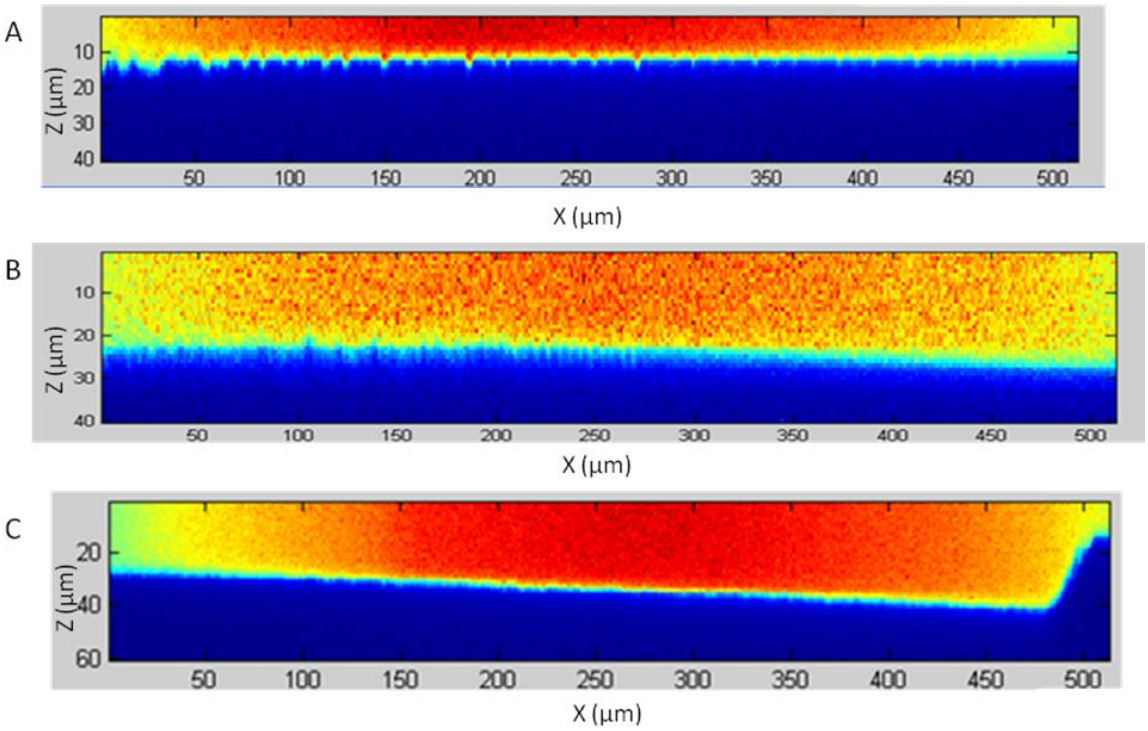

Figure 5.9. Calibration of ablation of glass slide. Smoothness of the ablated surface was assessed in glass slides. The smoothness was measured after the ablation with different step sizes. The smoothness increased as the step sizes were decreased. The step sizes were 5µm (A), 2.5µm (B), and 1µm (C). As step sizes were decreased, the surface roughness decreased to less than 1µm in the case of the smallest steps. In order to remedy the surface roughness and match refractive indices, cyanoacrylate glue was applied and a cover slip was attached, after the ablation was finished.

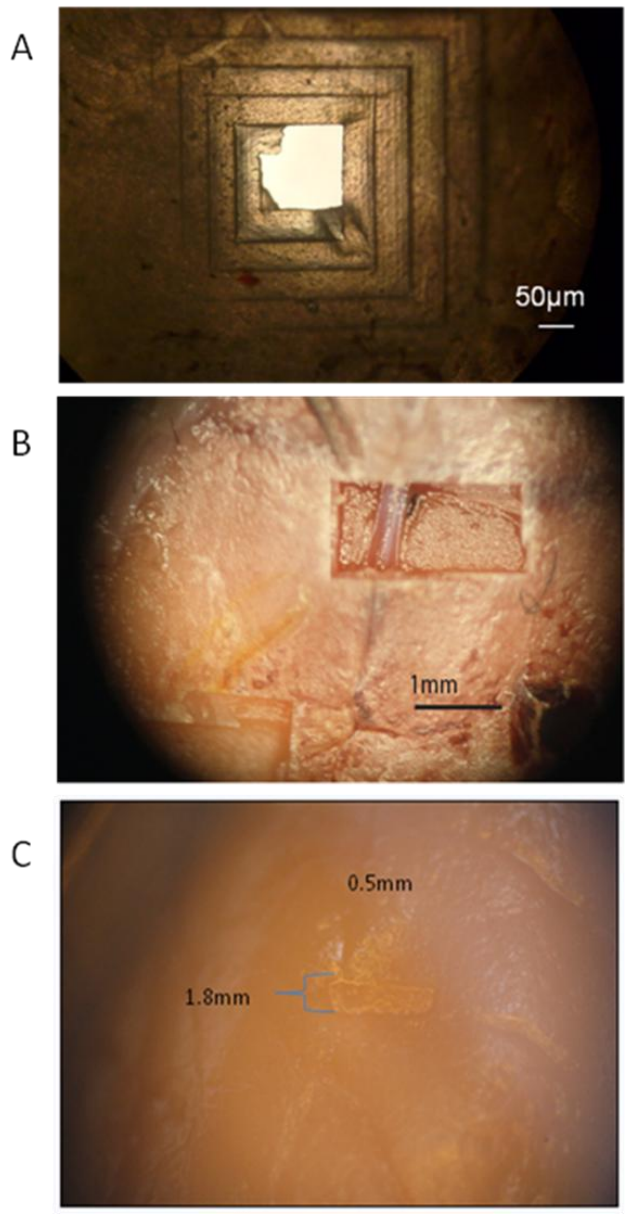

Figure 5.10. Ablation of bone, skull attached to brain, and brain tissue. (A) For the ablation of the skull, concentric squares were created with a decrement of 50µm. The skull was perforated at the last square. Unlike the holes created with mechanical tools, the precision and accuracy of the patterns were observed. (B) For the ablation of the skull with brain attached, the ablation was stopped as calcium signal decreased. The sagittal sinus was left intact, indicating the preciseness and sensitivity of the ablation technique. (C)Finally, in the soft tissue, a sharp square pattern was created without disrupting the soft tissue.

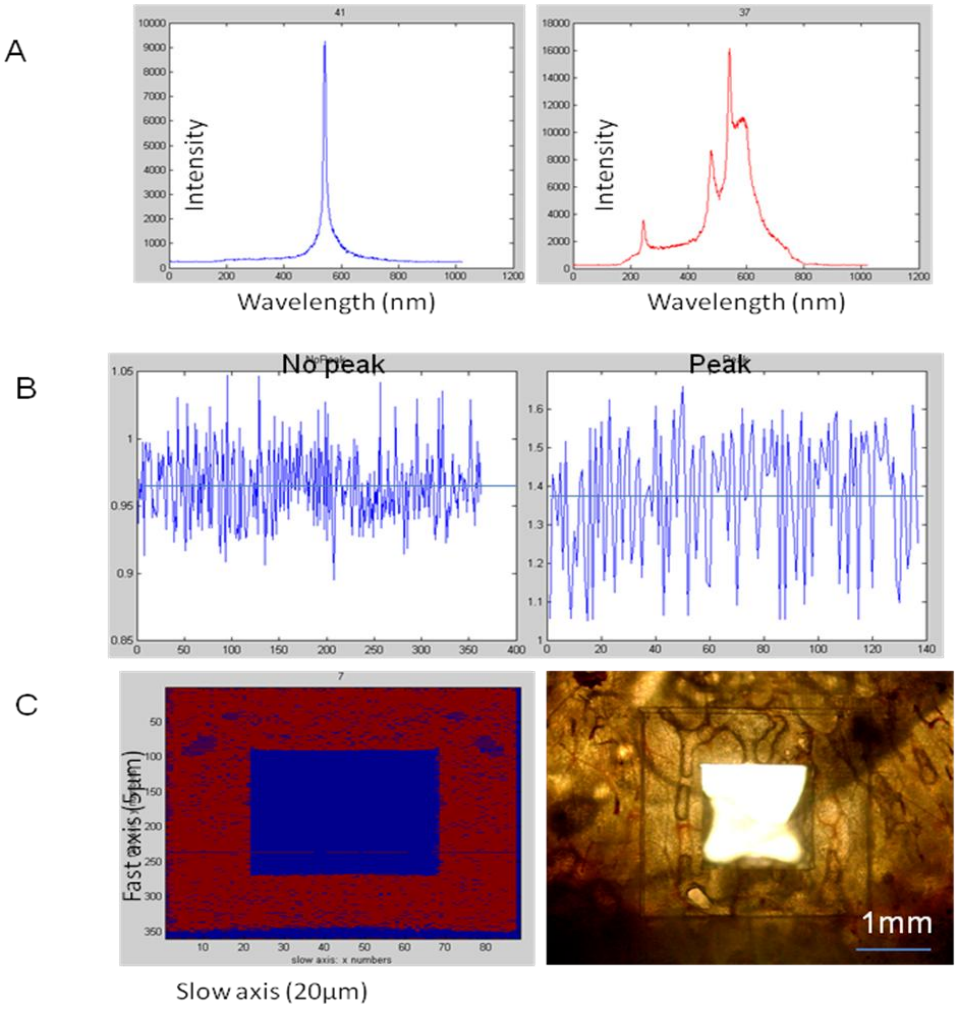

Figure 5.11. Feedback controlled ablation via LIBS. LIBS data was used as feedback during the laser ablation of bone. (A), (B) From the LIBS spectra, the ratio between the calcium peak at 422nm and 500nm were taken to determine the existence of the calcium peak automatically. The ratio reliably distinguished calcium peak vs. no calcium peak as the ratio increased from below 1 to 1.3-1.4. The ratio was thresholded to determine the peaks, and the peaks were assigned to red and no peaks were assigned for blue. (C) A bone sample with a hole was ablated and LIBS data was recorded simultaneously. The resolution was 5µm in the fast axis and 20µm in the slow axis. Images of the bone surface after each ablation pass were obtained from the LIBS signal. LIBS data reliably reconstructed the hole and the bone, confirming that the LIBS can be used as a detection signal for ablation of bone.

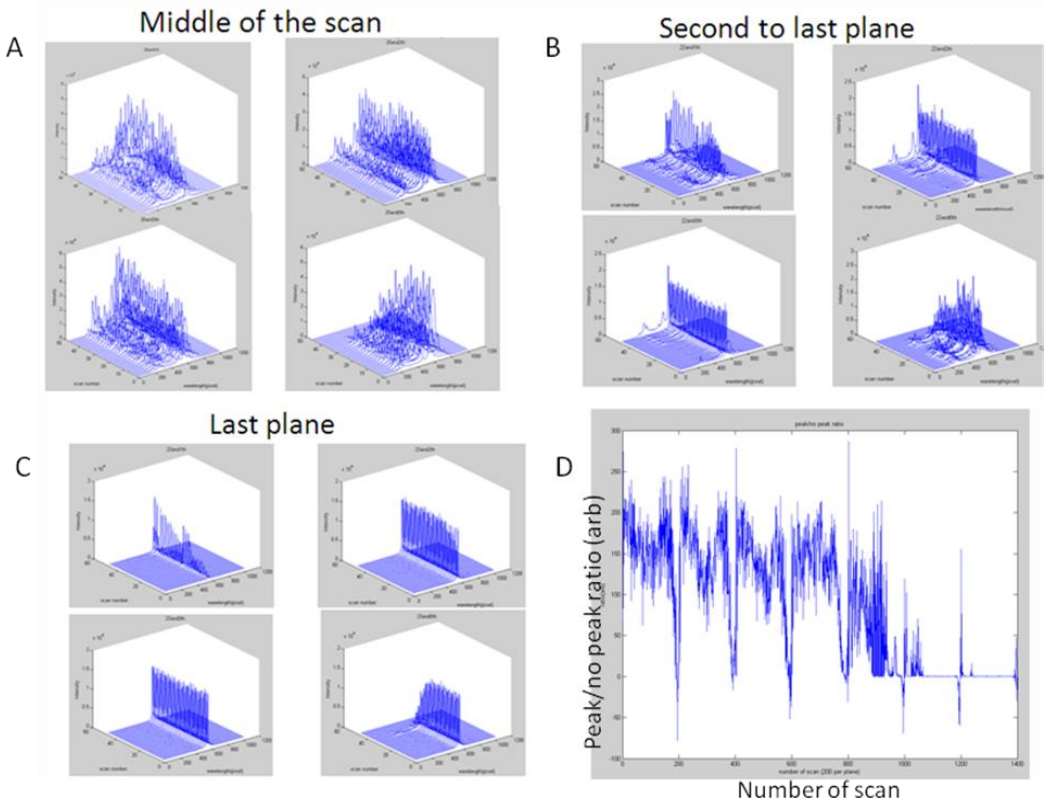

Figure 5.12. Confirmation of validity of the ablation along the curvature of bone. The ablation was performed along the curvature of bone captured by the SHG signal. At the beginning of the ablation procedure, only the sodium peaks were present as saline above bone was ablated mostly. (A) In the middle of the ablation scan, the bone was ablated and the LIBS signal contained calcium peaks. (B) When the second to last plane was ablated, the calcium peaks in the LIBS spectra started to disappear. (C) In the last plane, the calcium peaks in LIBS completely disappeared, indicating that the ablation along the bone curvature was reliable within 10μm. The step sizes were 5μm in x, y, and z. (D) The peak versus no peak ratio is plotted against number of scans, or travel in z. The ratio for calcium peaks suddenly dropped as the ablation through the bone was finished, and the signal was dominated with sodium peaks again.

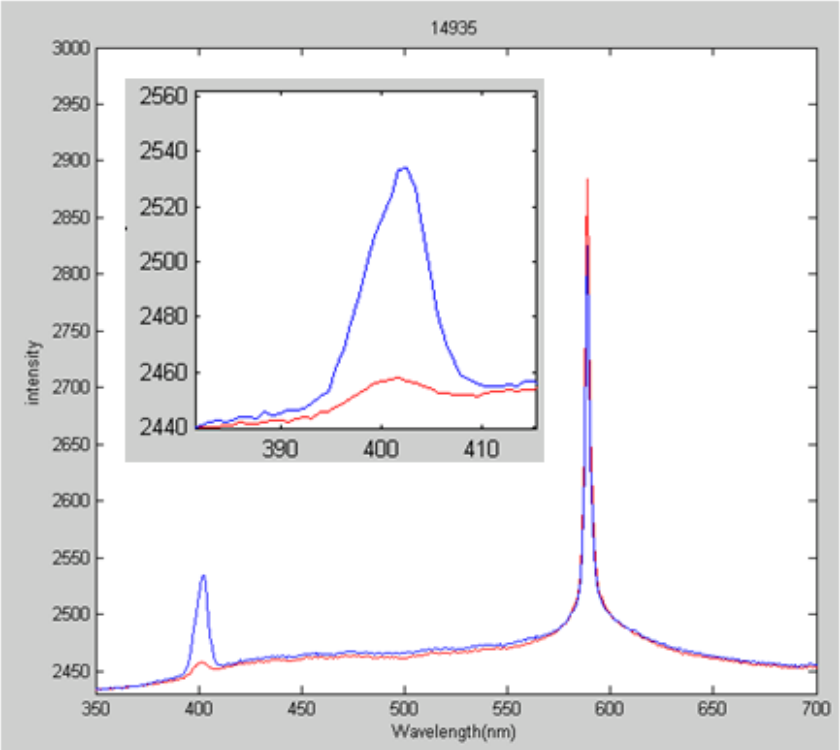

Figure 5.13. Comparison of SHG signals from bone versus tissue. SHG signal generated from bone (blue) was greater than that from soft tissue (red). With same pulse energy, the SHG signal at 400nm was much greater for bone. Both bone and tissue were submerged under saline. The sodium peaks in both spectra confirmed that the focus was above the surface of the sample. From the intensity difference in SHG generated by bone vs. soft tissue, it was possible to utilize SHG for measuring skull surface and thickness even near the brain tissue.

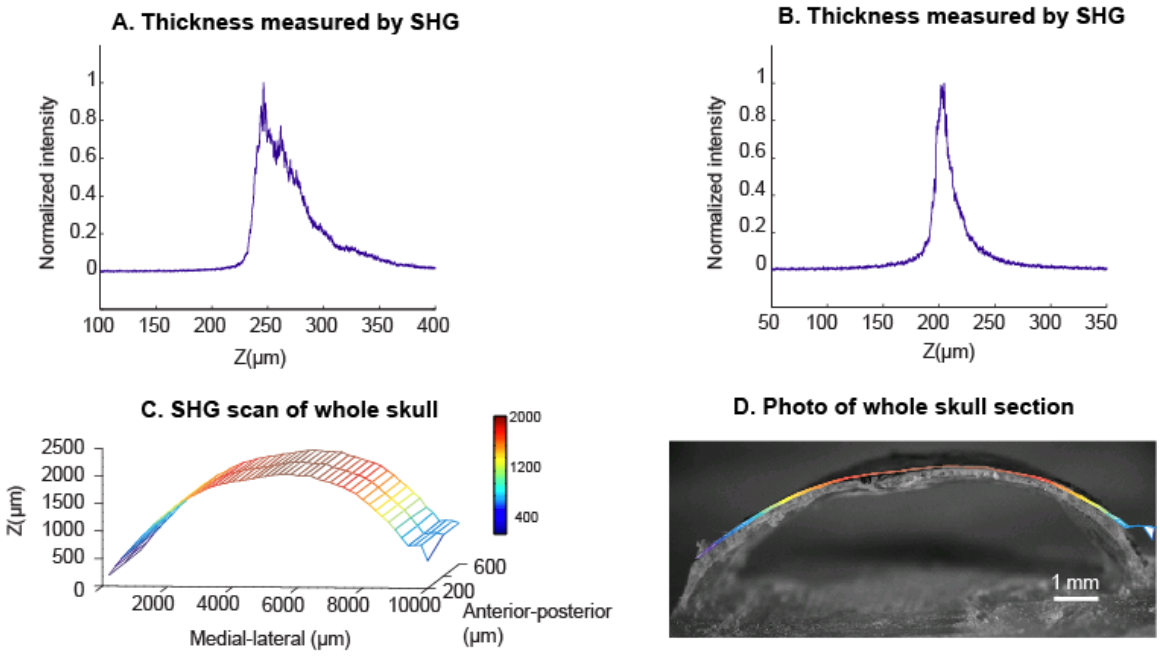

Fig 5.14. SHG measurement of skull surface and thickness. (A) Intact bone was scanned by SHG to obtain surface position. The signal increased as the focus approached the surface of the skull and then decayed to the background level as the focus was further lowered. (B) Previously thinned bone was measured by SHG to obtain both surface position and thickness, as a thinner bone sample reduced scattering within the bone. The thickness was obtained from the full-width half-maximum of the sharp decay in the SHG signal. (C) A region across the entire skull was mapped in the medial-lateral direction, via SHG scan. The area of the region was 1 X 0.4 mm with lateral step size of 200μm and 0.1μm resolution in the z direction. (D) The overlay of the curvature obtained in (C) with curvature obtained from brightfield microscopy is shown. The cross-section of the skull was obtained by mechanically cutting the skull along the previously scanned path.

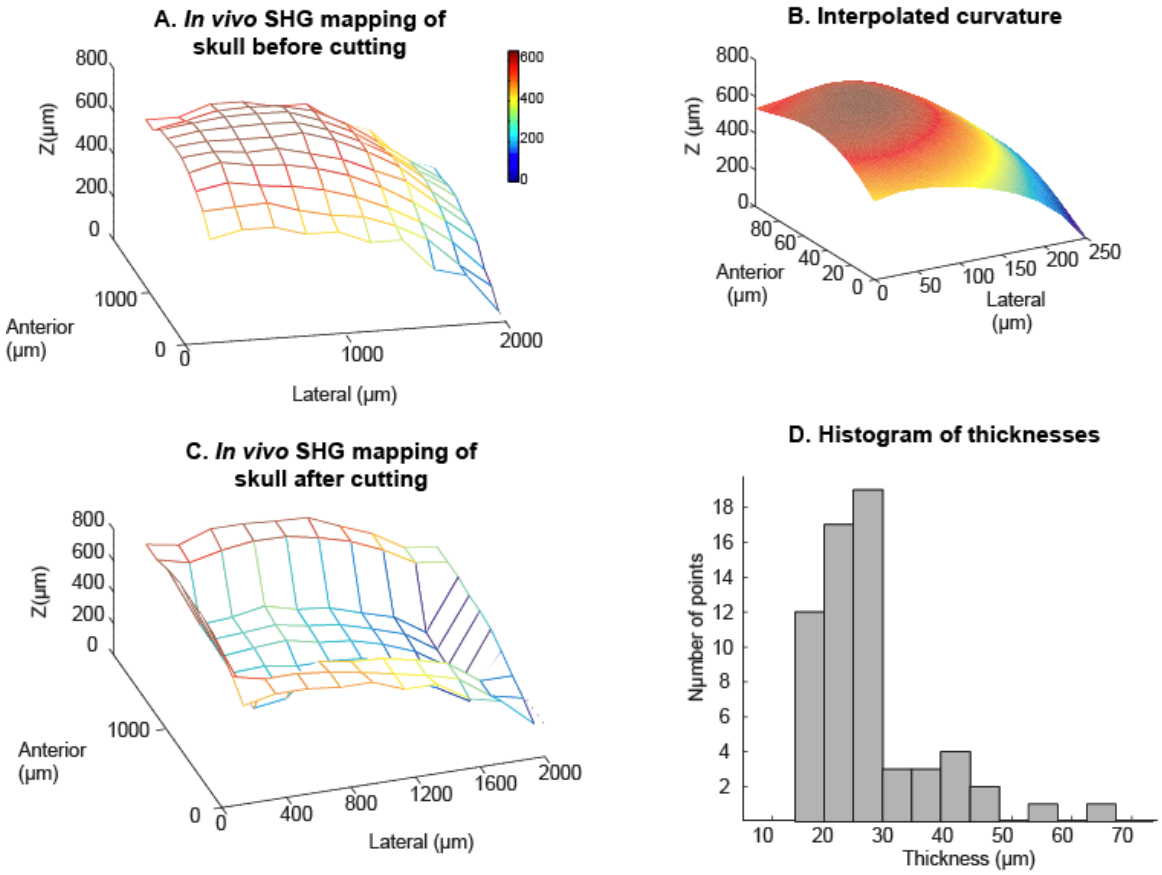

Figure 5.15. *In vivo* SHG mapping and thickness measurement in thinned skull surgery. (A) The intrinsic curvature of the skull was mapped over a 2 X 2 mm region to obtain the cutting path to create thinned skull window. (B) The curvature obtained in (A) was processed to obtain smooth curvature for the translational stage movements. (C) The top surface of the thinned skull window was measured with SHG after the laser ablation. (D) The histogram of the thickness obtained from SHG shows the median thickness of the window at 24μm.

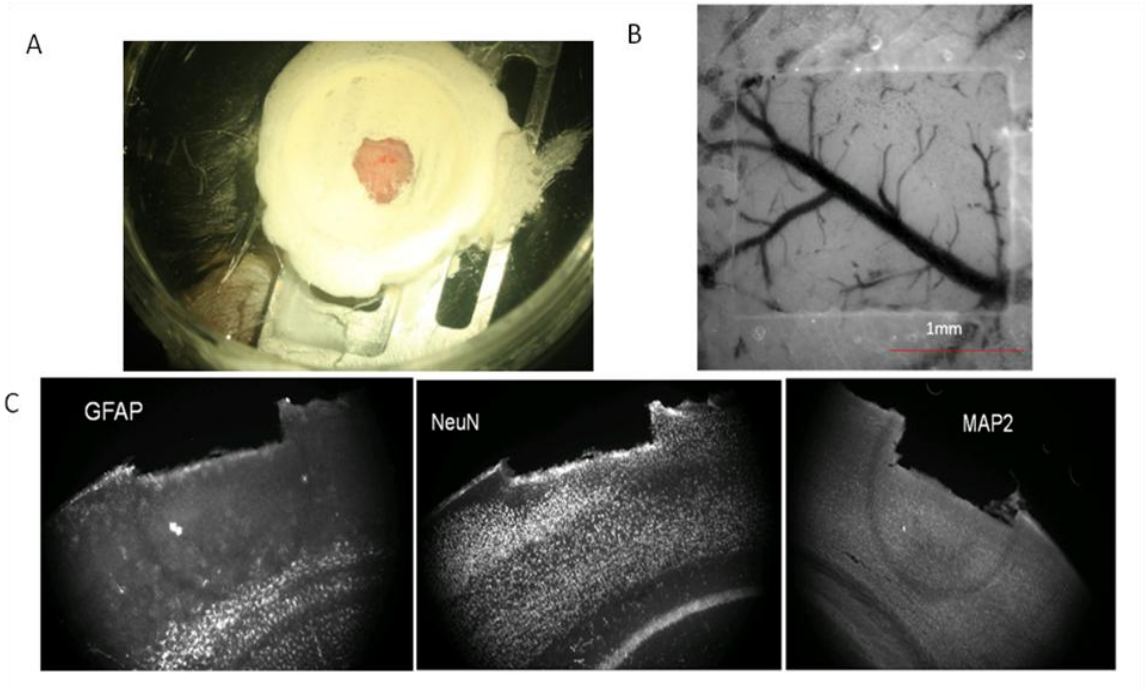

Figure 5.16. Thinned skull window after laser surgery. (A) The metal head plate and the well were attached to the mouse skull. (B) An example of thinned skull created by the laser ablation is shown. The thinned skull region was more transparent and the blood vessels were more visible in the region. (C) Soft tissue was ablated *in vivo*, and damages were assessed by using immunohistochemistry. Biomarker were used to indicate possible damages to the brain tissue after the ablation. Although bleeding occurred from the brain tissue, the histological assessment showed that the collateral damages were minimal.

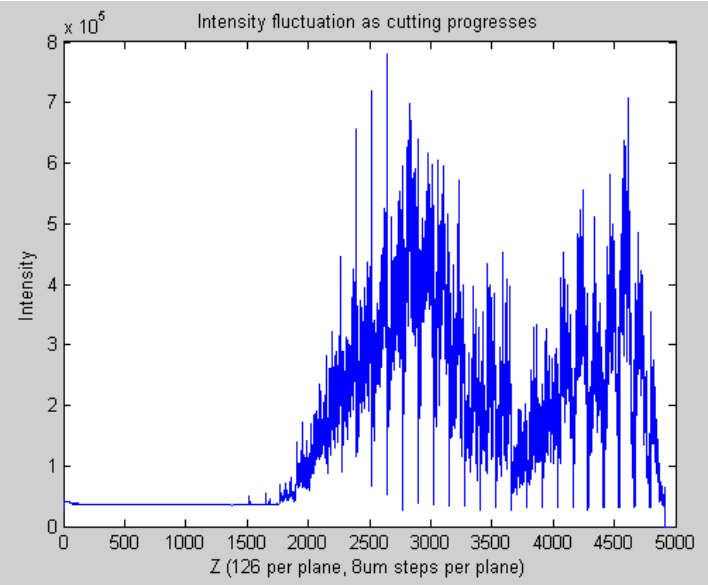

Figure 5.17. LIBS profile obtained from ablation of bone. The profile of the bone in the z direction was obtained from averaged LIBS signal. In each plane, the intensity of 422nm calcium peak was averaged. As the ablation started, the calcium signal was not present, and the calcium signal increased as the stage was lowered and ablation of bone started. The intensity decreased as the ablation was done in the porous region of bone. The intensity increased after the porous region was removed by the ablation and the ablation proceeds into the dense bone area. Although the resolution of the LIBS signal was not maximized, the averaged LIBS data gave a good overview of the status of the ablation process. The speed of the ablation process was increased as the SHG scans could be minimized until the ablation of the porous region was finished.

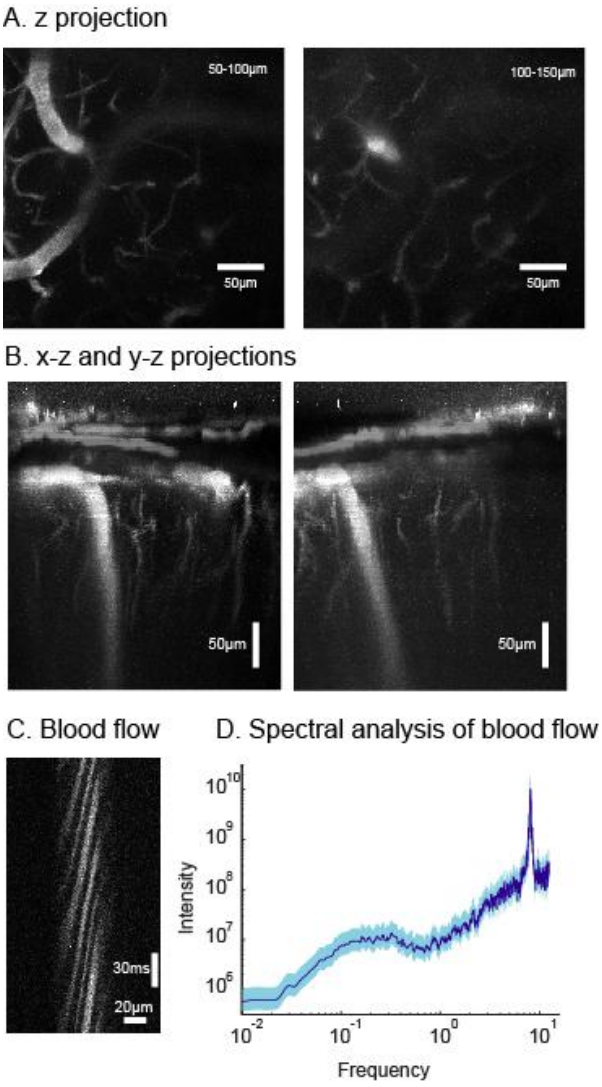

Fig 5.18. *In vivo* functional imaging through thinned skull window. Viability of thinned skull window. *In vivo* imaging and immunohistochemisty were performed to show the quality and viability of the thinned skull window made by laser ablation. (A) The stack of images over the range of 200μm depth in the cortex was taken through the thinned skull window in 300 X 300 μm region. The z-projection of 100-150μm (left) and 150-200 (right) showed that the arterioles were imaged through the thinned skull in the lateral direction. (B) The stack was resliced to obtain the x-z and y-z projection to visualize the vessels along the optical axis. The diving vessels were imaged down to 200μm in the cortex. (C) The blood flow was measured along the vessel to find the velocity of the red blood cells moving through the vessels. Individual red blood cells were imaged through the thinned skull window. (D) The velocity of the blood flow was analyzed to detect the heart rate of the animal at 8Hz, which is within the phyisological range for a mouse.

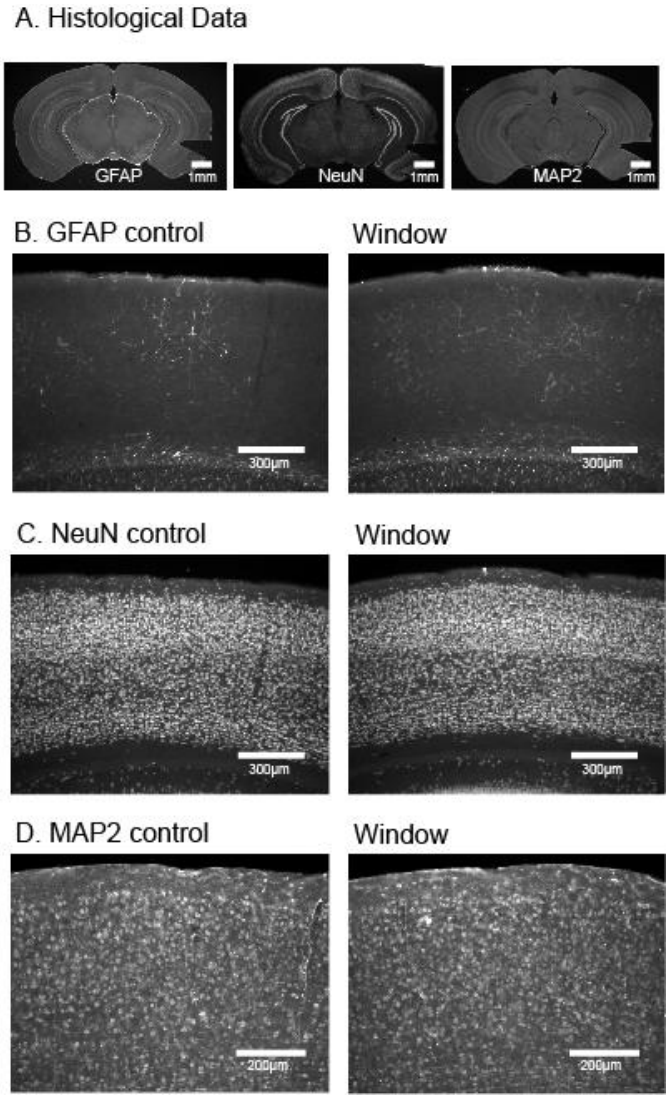

Figure 5.19. Verification of viability of brain tissue by immunohistochemistry. (A) The brain slices were stained with damage markers of MAP(Left), NeuN(Middle), and GFAP(right) to detect possible damages done to the brain from the laser ablation and imaging. (B) The GFAP marker visualizes glial activation which is an indication of damage. The brain under the thinned skull window (right) had a GFAP level comparable to the contralateral side as a control(left). (C) The NeuN marker stains the nuclei of the neurons and the cell densities are visualized. Both the window(right) and control(left) had comparable neuronal cell densities. (D) Neuronal processes are visualized by MAP staining. The processes of the neurons are preserved for both the window(right) and control(left).

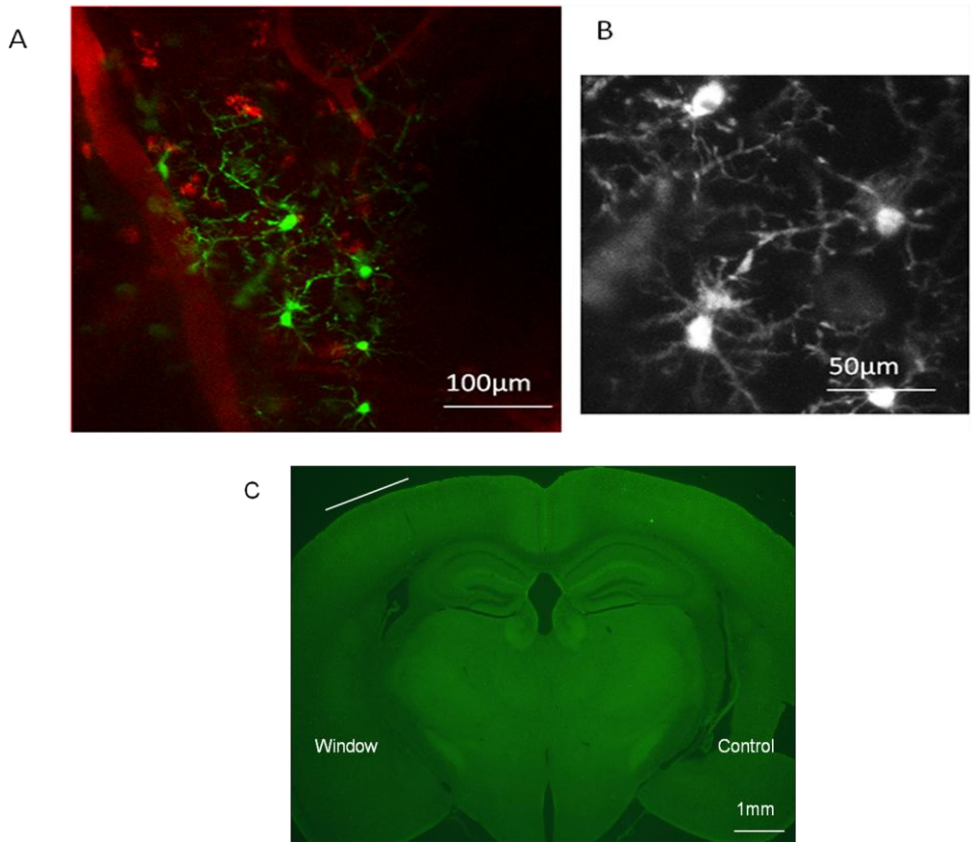

Figure 5.20. Confirmation of viability by observing microglia activation. The viability of the glia was observed through the thinned skull in a genetically engineered mouse. A thinned skull window was made by laser ablation in a CX3CR1 mouse, which was genetically engineered to have fluorescent glia. (A) Through the thinned skull window, blood vessels and microglia were imaged with two-photon laser scanning microscopy. The blood vessel was labeled with Texas red dye (red) and the microglia was imaged from the intrinsic labeling by enhanced green fluorescent proteins (green). (B) The zoomed in imaging of the microglia showed the processes of the cells were well-preserved, indicating the viability of the cells. (C) The overview of brain slice of the CX3CR1 mouse than has been imaged is presented. The glial activation levels were similar for both control and window, confirming the damages to the tissue by laser surgery was minimal.

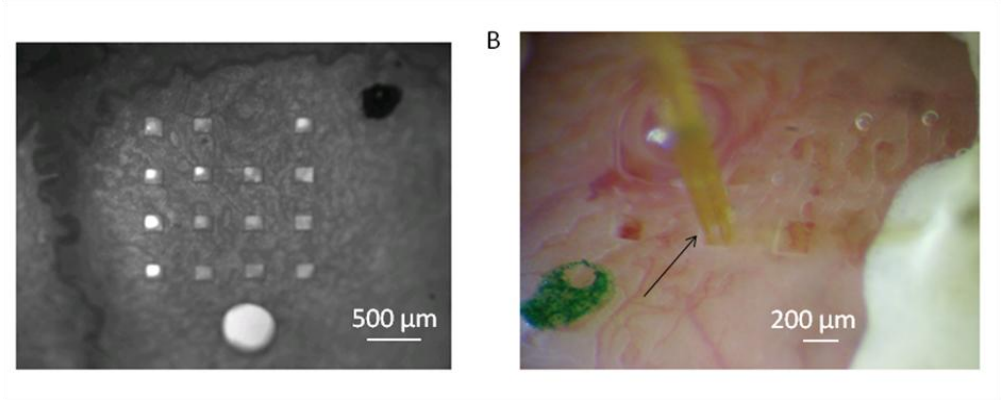

Figure 5.21. Creation of holes in skull via laser ablation. (A) An array of 200µm holes with 250µm spacing were made with laser ablation. For comparison, a hole was made with smallest dental drill burr, and the diameter of the hole was 500µm. (B) An array of holes were made *in vivo* with laser ablation and LIBS in a channel rhodopsin mouse, a genetically engineered mouse with light-excitable neurons. An optical fiber (arrow) was inserted though the hole to excite the neurons. Another metal electrode was inserted in another hole (not shown) to measure the firing of the cell excited by the light stimulation. Electrophysiology of the neurons were performed by Dr. Per Knutsen, with his experimental setup

Chapter 6. Discussion and concluding remarks

In this dissertation, the fabrication of a thinned skull window via laser ablation was demonstrated. The nonlinear optics techniques provided ways to (1) detect the surface of the skull, (2) to remove the skull, (3) to feedback control the ablation process, and to (4) *in vivo* image the brain tissue. The thinned skull window made from laser surgery was tested by imaging the vasculature, as well as the blood flow within the vasculature. The viability of the brain tissue after the thinned skull surgery was verified with immunohistochemistry, and no significant damages to the neuronal nuclei (NeuN), neuronal processes (MAP2), or activation of glial fibrilliary acidic protein (GFAP) was observed.

To further develop on this surgical technique, it is required to develop faster, more precise, full craniotomy capabilities. To address the limited speed of surgery, recent developments in temporal focusing can be applied to the laser surgical setup [138]. The laser pulse is dispersed temporally and spatially, and the ablation takes place only at the focus as the dispersed pulse components merge at that location. Even with a lower numerical aperture objective, the axial resolution of the ablation remains diffraction-limited. By utilizing this property, the region of the skull removed by a single pulse can be increased as the area of the focus is enlarged. A study applied to *ex vivo* rat skull demonstrated that a 2x2mm window can be created within 20 minutes [139].

Another issue to consider is increasing the precision of the surgery, by enhancing the second harmonic resolution. Currently, the resolution of second harmonic scanning

is limited to 200μm, mainly due to the speed issues. Various methods which can increase the scanning speed and resolution should be implemented.

Also, the LIBS signal can be more utilized in the system as a real-time feedback for craniotomies. Currently, the rendering speed of the spectra through the spectrometer is a rate limiting step, and the process needs to be accelerated. The software interface with the spectrometer can be improved by using a lower-level language and implementing the dynamic link library via a software development kit.

Multiple applications of the automated cranial surgery are possible, such as fabricating complicated patterns in the skull and making arrays of holes for multi-electrode recordings. For more efficient and improved instrumentations, automated cranial surgery for custom patterns will become available.

This dissertation explores the ways to automate cranial surgery, and shows the first proof-of-principle experiment for *in vivo* surgery in mouse. Further advances will provide easier and more efficient surgical techniques, applicable to both animals and clinical surgeries.

References

1. Schawlow, A.L., Townes, C.H., *Infrared and Optical Masers*. Physical Review, 1958. 112:1940-1949.

2. Fork, R. L., Greene, B. I., and Shank, C. V., *Generation of optical pulses shorter than 0.1 psec by colliding pulse mode locking.* Applied Physics Letters, 1981. 38: 671-672.

3. Chen, S., Maksimchuk, A., and Umstadter., D. *Experimental observation of relativistic nonlinear Thomson scattering*. Nature 1998, 396: 653-655.

4. Siegman, A. E., *Lasers*. University Science Books, 1986.

5. McClung, F. J., and Hellwarth, R. W. *Giant Optical Pulsations from Ruby*. Journal of Applied Physics, 1962. 33: 828-829.

6. Colin, S., Contesse, E., Le Boudec, P., Stephan, G., and Sanchez, F., *Evidence of a saturable-absorption effect in heavily erbium-doped fibers*. Optics Letters, 1996. 21: 1987-1989.

7. Geusic, J. E., Marcos, H. M., van Uitert, L. G., *Laser Oscillations in Nd-doped Yttrium Aluminum, Yttrium Gallium and Gadolinium Garnets*. Applied Physics Letters, 1964. 4: 182-184.

8. Lamb WE, Jr.: Theory of an Optical Maser. Physical Review, 1964. 134:A1429-A1450.

9. Koechner, W., *Solid-state laser engineering*. Springer-Verlag, 1965.

10. Hargrove, L. E., Fork R. L., and Pollack, M. A. *Locking of He–Ne laser modes induced by synchronous intracavity modulation.* Applied Physics Letters, 1964. 5: 4-5.

11. Ippen, E.P., Shank, C.V., and Dienes, A. *Passive mode locking of the cw dye laser*. Applied Physics Letters, 1972. 21: 348-350.

12. Trebino, R., and Zeek, E., *Ultrashort Laser Pulses*. Ultrafast optics, Trenbio, R. (Ed.) pre-published online.

13. Strickland, D., Mourou, G. *Compression of amplified chirped optical pulses*. Optics Communications, 1985. 56:219-221.

14. Squier, J., Durfee III, C., Planchon, T., *Chirped Pulse Amplification*. Ultrafast optics, Trenbio, R. (Ed.) pre-published online.

15. D. C. Jeong, P. S. Tsai and D. Kleinfeld. *Prospect for feedback guided surgery with ultra-short pulsed laser light*. Current Opinions in Neurobiology, 2012. 22:24-33

16. D.B. Murphy, *Fundamentals of light microscopy and electronic imaging*. Wiley-Blackwell, 2013

17. Bradbury, S. and Bracegirdle, B., *Introduction to Light Microscopy,*BIOS Scientific Publishers, 1998

18. R.W. Boyd, *Nonlinear optics.* Academic Press, 2003

19. A. Koehler, *New Method of Illimination for Phomicrographical Purposes*. Journal of the Royal Microscopical Society, 1894. 14: 261–262.

20. M. Minsky, *Memoir on Inventing the Confocal Scanning Microscope.* Scanning, 1988. 10: 128–138.

21. G. Cox and C. J. R. Sheppard, *Practical Limits of Resolution in Confocal and Non-Linear Microscopy*. Microscopy research and technique, 2004. 63:18 –22

22. M. Dailey, E. Manders, D. Soll, and M. Terasaki, *Handbook of Biological Confocal Microscopy* (James Pawley, Ed). Springer, 2005

23. M. Goeppert-Mayer, *Über Elementarakte mit zwei Quantensprüngen*. Ann Phys, 1931. 9: 273–95

24. W. Denk, J. Strickler, and W. Webb, *Two-photon laser scanning fluorescence microscopy*. Science, 1990. 248: 73–6

25. R. Tsien, *The green fluorescent protein*. Annu Rev Biochem, 1998. 67: 509–44

26. D. Kleinfeld, P. P. Mitra, F. Helmchen, and W. Denk, *Fluctuations and stimulus-induced changes in blood flow observed in individual capillaries in layers 2 through 4 of rat neocortex*. Proceedings of the National Academy of Sciences USA, 1998. 95:15741-15746

27. Reinhardt, B. A., Brott, L. L., Clarson, S. J., Dillard A. G., Bhatt, J.C., Kannan, R., Yuan, L., He, G. S., and Prasad, P. N., *Highly Active Two-Photon Dyes: Design, Synthesis, and Characterization toward Application.* Chemistry of Materials, 1998. 10: 1863-1874

28. Praag, H., Schinder, A. F., Christie, B. R., Toni, N., Palmer., T. D., Gage, F. H., *Functional neurogenesis in the adult hippocampus*. Nature, 2002. 415: 1030-1034

29. Nguyen, Q.-T., Schroeder, L. F., Mank, M., Muller, A., Taylor, P. W., Griesbeck, O. and Kleinfeld, D. , *An in vivo biosensor for neurotransmitter release and in situ receptor activity*. Nature Neuroscience, 2010. 13:127-132

30. Proebstl, D., Voisin, M.-B., Woodfin, A., Whiteford, J., D'Acquisto, F., Jones, G. E., Rowe, D., and Nourshargh, S., *Pericytes support neutrophil subendothelial cell crawling and breaching of venular walls in vivo*. JEM 209:1219-1234

31. Tian, L., Hires, S. A., Mao, T., Huber, D., Chiappe, M. E., Chalasani, S. H., Petreanu, L., Akerboom, J., McKinney, S. A., Schreiter, E. R., Bargmann C., Jayaraman, V., Svoboda, K., and Looger, L. L., I*maging neural activity in worms, flies and mice with improved GCaMP calcium indicators.* Nature Methods, 2009. 6: 875 - 881

32. P. S. Tsai and D. Kleinfeld, *In vivo two-photon laser scanning microscopy with concurrent plasma-mediated ablation: Principles and hardware realization*. Methods for In Vivo Optical Imaging, Second Edition, R. Frostig, editor, 2009. CRC Press, 3:59-115.

33. J. Driscoll and Q. -T. Nguyen, *MPScope 2.0*.

34. . I. Valmianski, A. Y. Shih, J. D. Driscoll, D. M. Matthews, Y. Freund and D. Kleinfeld, *Automatic identification of fluorescently labeled brain cells for rapid functional imaging*. Journal of Neurophysiology, 2010. 104:1803-1811.

35. J. Driscoll, *Techniques in Two-Photon Microscopy for Neuroscience*. Doctoral dissertation, 2011.

36. Chronux.org

37. Guo, Y., Ho, P.P., Savage, H., Harris, D., Sacks, P., Schantz, S., Liu, F., Zhadin, N., and Alfano, R.R., *Second-harmonic tomography of tissues*. Optics Letters, 1997. 22: 1323-1325.

38. Shen, Y.R., *The Principles of Nonlinear Optics*. 1984, New York: John Wiley and Sons.

39. Agrawal, G., *Nonlinear Fiber Optics.* Academic Press, 2006. (4^{th} edition)

40. Franken, P., Hill, A., Peters, C. and Weinreich, G., *Generation of Optical Harmonics*. Physical Review Letters, 1961. 7: 118

41. Campagnola, P. J. and Loew, L. M., *Second-harmonic imaging microscopy for visualizing biomolecular arrays in cells, tissues and organisms*. Nature Biotechnology, 2003. 22: 1356 - 1360

42. Träger, Frank (Ed.), *Handbook of Lasers and Optics*. Springer Handbooks, 2007. XXVI, 1332 p. 978

43. Campagnola PJ, Wei MD, Lewis A, Loew LM., *High-resolution nonlinear optical imaging of live cells by second harmonic generation*. Biophys J, 1999. 77:3341-9

44. Williams, R. M., Zipfel, W. R., and Webb, W. W., *Interpreting Second-Harmonic Generation Images of Collagen I Fibrils*. Biophys J., 2005. 88: 1377–1386.

45. Ashwell, G. J., Jackson, P. D., and Crossland, W. A., *Non-centrosymmetry and second-harmonic generation in Z-type Langmuir–Blodgett films.* Nature, 1994. 368: 438 - 440

46. Fejer, M.M., *Quasi-phase-matched second harmonic generation: tuning and tolerances*. IEEE Journal of Quantum Electronics, 1992. 28:2631-2654

47. Squier, J., Muller, M., Barzda, V., *Multiphoton Microscopy with Ultrafast Lasers*, Trebino, R., Ultrafast optics, unpublished text book.

48. Zipfel, W.R., Williams, R.M., Christie, R., Nikitin, A.Y., Hyman, B.T., and Webb, W.W., *Live tissue intrinsic emission microscopy using multiphoton-excited native fluorescence and second harmonic generation*. Proceedings of the National Academy of Sciences USA, 2003. 100: 7075-7080.

49. Nadiarnykh, O., Plotnikov, S., Mohler, W.A., Kalajzic, I., Redford-Badwal, D., and Campagnola, P.l.J., *Second harmonic generation imaging microscopy studies of osteogenesis imperfecta.* Journal of Biomedical Optics, 2007. 12: 051805.

50. Binder, P.S., Sarayba, M., Ignacio, T., Juhasz, T., and Kurtz, R., *Characterization of submicrojoule femtosecond laser corneal tissue dissection*. Journal of Cataract and Refractive Surgery, 2008. 34(1): 146-152.51. 61

51. Dombeck, D. A., Blanchard-Desce, M., and Webb, W. W., *Optical Recording of Action Potentials with Second-Harmonic Generation Microscopy*. The Journal of Neuroscience, 2004. 24:999 –1003

52. Campagnola, P.J., Clark, H.A., Mohler, W.A., Lewis, A., and Loew, L.M., *Second-harmonic imaging microscopy of living cells*. Journal of Biomedical Optics, 2001. 6: 277-286.

53. Zipfel, W.R., Williams, R.M., Christie, R., Nikitin, A.Y., Hyman, B.T., and Webb, W.W., *Live tissue intrinsic emission microscopy using multiphoton-excited native fluorescence and second harmonic generation*. Proceedings of the National Academy of Sciences USA, 2003. 100: 7075-7080.

54. Mertz, J., *Nonlinear microscopy: New techniques and applications.* Current Opinion in Neurobiology, 2004. 14: 610-616.

55. Vogel, A. and Venugopalan, V., *Mechanisms of pulsed laser ablation of biological tissues*. Chem Rev, 2003. 103:577-644.

56. Vogel, A., Noack, J., Huttman, G., and Paltauf, G., *Mechanisms of femtosecond laser nanosurgery of cells and tissues.* Applied Physics B-Lasers and Optics, 2005. 81(8): 1015-1047.

57. Karplus, M. and Porter, R.N., *Atoms and Molecules: An Introduction for Students of Physical Chemistry*. 1970, New York: W. A. Benjamin.

58. Joglekar, A.P., Liu, H.H., Meyhofer, E., Mourou, G., and Hunt, A.J., *Optics at critical intensity: Applications to nanomorphing*. Proceedings of the National Academy of Sciences USA, 2004. 101: 5856-5861.

59. Venugopalan, V., Nishioka, N.S. and Mikic, B.B., *The thermodynamic response of soft biological tissues to pulsed ultraviolet laser irradiation.* Biophysical Journal 69: 1259-1271

60. Stuart, B.C., Feit, M.D., Rubenchik, A.M., Shore, B.W., and Perry, M.D., *Laser-induced damage in dielectrics with nanosecond to subpicosecond pulses*. Physical Review Letters, 1995. 74: 2248-2251.

61. Loesel, F.H., Niemez, M.H., Bille, J.F., and Juhasz, T., *Laser-induced optical breakdown on hard and soft tissues and its dependence on the pulse duration: Experiment and model*. IEEE Journal of Quantum Electronics, 1996. 32: 1717-1722.

62. Stuart, B.C., Feit, M.D., Herman, S., Rubenchik, A.M., Shore, B.W., and Perry, M.D., *Nanosecond-to-femtosecond laser-induced breakdown in dielectrics*. Physical Review B, 1996. 53: 1749-1761.

63. Neev, J., Nelson, J.S., Critelli, M., McCullough, J.L., Cheung, E., Carrasco, W.A., Rubenchik, A.M., Da Silva, L.B., Perry, M.D., and Stuart, B.C., *Ablation of human nail by pulsed lasers. Lasers in Surgery and Medicine*, 1997. 21: 186-192.

64. Rode, A.V., Gamaly, E.G., Luther-Davies, B., Taylor, B.T., Dawes, J., Chan, A., Lowe, R.M., and Hannaford, P., *Subpicosecond laser ablation of dental enamel*. Journal of Applied Physics, 2002. 92: 2153-2158.

65. Weigl, P., Kasenbacher, A., and Werelius, K., *Femtosecond Technology for Technical and Medical Applications*. 2004, Berlin: Springer-Verlag.

66. Armstrong, W.B., Neev, J.A., Da Silva, L.B., Rubenchik, A.M., and Stuart, B.C., *Ultrashort pulse laser ossicular ablation and stapedotomy in cadaveric bone*. Lasers in Surgery and Medine, 2002. 30: 216-220.

67. Schwab, B., Hagner, D., Bornemann, J., and Heermann, R*., The use of femtosecond technology in otosurgery*. Topics in Applied Physics, 2004. 96: 211-226.

68. Liu, Y. and Niemz, M., *Ablation of femural bone with femtosecond laser pulses: A feasibility study*. Lasers in Medical Science, 2007. 22: 171-174.66-69. 35-37

69. Kautek, W., and Kruger, J., *Femtosecond pulse laser ablation of metallic, semiconducting, ceramic, and biological materials.* Proc. SPIE 2207, Laser Materials Processing: Industrial and Microelectronics Applications, 1994. 600

70. Lim, Y.C., Altman, K.J., Farson, D.F., and Flores, K.M., *Micropillar fabrication on bovine cortical bone by direct-write femtosecond laser ablation*. Journal of Biomedical Optics, 2009. 14: 064021-1-10.

71. Schaffer, C.B., Nishimura, N., Glezer, E.N., Kim, A.M.T., and Mazur, E., *Dynamics of femtosecond laser-induced breakdown in water from femtoseconds to microseconds.* Optics Express, 2002. 10(3): 196-203.

72. Stuart, B.C., Feit, M.D., Herman, S., Rubenchik, A.M., Shore, B.W., and Perry, M.D., *Optical ablation by high-power short-pulse lasers.* Journal of the Optical Society of America B, 1996. 13: 459-468.

73. Ladieu, F., Martin, P., and Guizard, S., *Measuring thermal effects in femtosecond laser-induced breakdown of dielectrics*. Applied Physics Letters, 2002. 81: 957-959.

74. Rode, A.V., Gamaly, E.G., and Luther-Davies, B., *Subpicosecond laser ablation of dental enamel*. Journal of Applied Physics, 2002. 92: 2153-2158.

75. McCaughey, R.G., Sun, H., Rothholtz, V.S., Juhasz, T., and Wong, B.J.F., *Femtosecond laser ablatiion of the stapes*. Journal of Biomedical Optics, 2009. 14: 0240401.

76. Chicbkov, B.N., Momma, C., Nolte, S., yon Alvensleben, F. and Tiinnermann, A., *Femtosecond, picosecond and nanosecond laser ablation of solids*. Appl. Phys. A, 1996. 63: 109-115

77. Sacconi, L., O'Connor, R.P., Jasaitis, A., Masi, A., Buffelli, M., and Pavone, F.S., *In vivo multiphoton nanosurgery of cortical neurons.* Journal of Biomedical Optics, 2007. 12: 1-3.

78. Guo, S.X., Bourgeois, F., Chokshi, T., Durr, N.J., Hilliard, M.A., Chronis, N., and Ben-Yakar, A., *Femtosecond laser nanoaxotomy lab-on-a chip for in vivo nerve regeneration studies*. Nature Methods, 2008. 5: 531-533.

79. Nguyen, J., Ferdman, J., Zhao, M., Huland, D., Saqqa, S., Ma, J., Nishimura, N., Schwartz, T.H., and Schaffer, C.B., *Sub-surface, micrometer-scale incisions produced in rodent cortex using tightly-focused femtosecond laser pulses*. Lasers in Surgery and Medicine, 2011. 43: 382-391.

80. Shen, N., Datta, D., Schaffer, C.B., LeDuc, P., Ingber, D.E., and Mazur, E., *Ablation of cytoskeletal filaments and mitochondria in live cells using a femtosecond laser nanoscissor.* Mechanical and Chemical Biosystems, 2005. 2: 17-25.

81. Soong, H.K., Mian, S., Abbasi, O., and Juhasz, T., *Femtosecond laser–assisted posterior lamellar keratoplasty: Initial studies of surgical technique in eye bank eyes.* Ophthalmology, 2005. 112: 44-49.

82. Binder, P.S., Sarayba, M., Ignacio, T., Juhasz, T., and Kurtz, R., *Characterization of submicrojoule femtosecond laser corneal tissue dissection.* Journal of Cataract and Refractive Surgery, 2008. 34(1): 146-152.

83. Nishimura, N., Schaffer, C.B., Friedman, B., Tsai, P.S., Lyden, P.D., and Kleinfeld, D., *Targeted insult to individual subsurface cortical blood vessels using ultrashort laser pulses: Three models of stroke*. Nature Methods, 2006. 3: 99-108.

84. Nishimura, N., Rosidi, N.L., Iadecola, C., and Schaffer, C.B., *Limitations of collateral flow after occlusion of a single cortical penetrating arteriole.* Journal of Cerebral Blood Flow and Metabolism, 2010. 30: 1914-1927.

85. Yalcin, H.C., Shekhar, A., Nishimura, N., Rane, A.A., Schaffer, C.B., and Butcher, J.T., *Two-photon microscopy-guided femtosecond-laser photoablation of avian cardiogenesis: Noninvasive creation of localized heart defects.* American Journal of Physiology: Heart and Circulation Physiology, 2010. 299: H1728-1735.

86. Tsai, P.S., Friedman, B., Ifarraguerri, A.I., Thompson, B.D., Lev-Ram, V., Schaffer, C.B., Xiong, Q., Tsien, R.Y., Squier, J.A., and Kleinfeld, D., *All-optical histology using ultrashort laser pulses.* Neuron, 2003. 39: 27-41.

87. Leis, F., Sdorra, W., Ko, J.B., Niemax, K., *Basic investigations for laser microanalysis I: optical emission spectrometry of laser-produced sample plumes.* Mikrochim. Acta, II, 1989, 98:185–190

88. Cremers, D.A. and Radziemski, L.J., *Handbook of laser-induced breakdown spectroscopy.* 2006, San Francisco: Wiley.

89. Gurevich, E.L. and Hergenroeder, R., *Femtosecond laser-induced breakdown spectroscopy: Physics, applications, and perspectives*. Applied Spectroscopy, 2007. 61: 233A-242A.

90. Assion, A., Wollenhaupt, M., Haag, L., Mayorov, F., Sarpe-Tudoran, C., Winter, M., Kutschera, U., and Baumert, T., *Femtosecond laser-induced-breakdown spectrometry for Ca2+ analysis of biological samples with high spatial resolution.* Applied Physics B Lasers and Optics, 2003. 77: 391-397.

91. Corsi, M., Cristoforetti, G., Hidalgo, M., Legnaioli, S., Palleschi, V., Salvetti, A., Tognoni, E., and Vallebona, C., *Application of laser-induced breakdown spectroscopy technique to hair tissue mineral analysis.* Applied Optics, 2003. 42: 6133-6137.

92. Samuels, A.C., DeLucia, F.C., McNesby, K.L., and Miziolek, A.W., *Laser-induced breakdown spectroscopy of bacterial spores, molds, pollens, and protein: Initial studies of discrimination potential.* Applied Optics, 2003. 42: 6205-6209.

93. Trevizan, L.C., Freitas, A.Z.D.E., and Vieira, N.D., *Evaluation of femtosecond laser-induced breakdown spectroscopy for analysis of animal tissues*. Applied Spectroscopy, 2008. 62: 1137-1143.

94. Kim, B.M., Feit, M.D., Rubenchik, A.M., Mammini, B.M., and Da Silva, L.B., *Optical feedback signal for ultrashort laser-pulse ablation of tissue.* Applied Surface Science, 1998. 127: 857-862.

95. Samek, O., Beddows, D.C.S., Telle, H.H., Kaiser, J., Liska, M., Caceres, J.O., and Urena, A.G., *Quantitative laser-induced breakdown spectroscopy analysis of calcified tissue samples.* Spectrochimica Acta Part B - Atomic Spectroscopy, 2001. 56: 865-875.

96. Abdel-Salam, Z.A., Nanjing, Z., Anglos, D., and Harith, M.A., *Effect of experimental conditions on surface hardness measurements of calcified tissues via LIBS*. Applied Physics B - Lasers and Optics, 2009. 94: 141-147.

97. Radziemski, L. J., Loree, T. R., Cremers, D. A., and Hoffman, N. M., *Time-resolved laser-induced breakdown spectrometry of aerosols.* Anal. Chem., 1983. 55: 1246

98. Rethfeld, B., Sokolowski-Tinten, K., von der Linde, D., Anisimov, S.I., *Timescales in the response of materials to femtosecond laser excitation*. Appl. Phys. A, 2004. 79: 767–769

99. Piñon, V. and Anglosa, D., *Optical emission studies of plasma induced by single and double femtosecond laser pulses*. Spectrochimica Acta Part B: Atomic Spectroscopy, 2009. 64:950–960

100. Tognoni, E., Palleschi, V., Corsi, M. and Cristoforetti, G., *Quantitative micro-analysis by laser-induced breakdown spectroscopy: a review of the experimental approaches*. Spectrochimica Acta Part B: Atomic Spectroscopy, 2002. 57: 1115–1130

101. Wiza, J., *Microchannel plate detectors*. Nuclear Instruments and Methods, 1979. 162: 587–601.

102. Margetic, V., Pakulev, A., Stockhaus, A., Bolshov, M., Niemax, K., and Hergenroder, R., *A comparison of nanosecond and femtosecond laser-induced plasma spectroscopy of brass samples*. Spectrochimica Acta Part B - Atomic Spectroscopy, 2000. 55: 1771-1785.

103. Sirven, J.B., Bousquet, B., Canioni, L., and Sarger, L., *Time-resolved and time-integrated single-shot laser-induced plasma experiments using nanosecond and femtosecond laser pulses*. Spectrochimica Acta Part B - Atomic Spectroscopy, 2004. 59: 1033-1039.

104. Cremers, D.A., Radziemski, L.J., and Loree, T.R., *Spectrochemical analysis of liquids using the laser spark*. Applied Spectroscopy, 1984. 38(5): 721-729.

105. Pichahchy, A.E., Cremers, D.A., and Ferris, M.J., *Elemental analysis of metals under water using laser-induced breakdown spectroscopy*. Spectrochimica Acta Part B - Atomic Spectroscopy, 1997. 52: 25-39.

106. De Giacomo, A., Dell'Aglio, M., De Pascale, O., and Capitelli, M., *From single pulse to double pulse ns-laser induced breakdown spectroscopy under water: Elemental analysis of aqueous solutions and submerged solid samples*. Spectrochimica Acta Part B - Atomic Spectroscopy, 2007. 62: 721-738.

107. Gottfried, J.L., De Lucia, F.C., Munson, C.A., and Miziolek, A.W., *Double-pulse standoff laser-induced breakdown spectroscopy for versatile hazardous materials detection*. Spectrochimica Acta Part B - Atomic Spectroscopy, 2007. 62: 1405-1411.

108. Lazic, V., Colao, F., Fantoni, R., Spizzichino, V., and Jovicevic, S., *Underwater sediment analyses by laser induced breakdown spectroscopy and calibration procedure for fluctuating plasma parameters.* Spectrochimica Acta Part B - Atomic Spectroscopy, 2007. 62: 30-39.

109. Abdel-Salam, Z.A., Nanjing, Z., Anglos, D., and Harith, M.A., *Effect of experimental conditions on surface hardness measurements of calcified tissues via LIBS*. Applied Physics B - Lasers and Optics, 2009. 94: 141-147.

110. De Giacomo, A., Dell'Aglio, M., Colao, F., and Fantoni, R., *Double pulse laser produced plasma on metallic target in seawater: basic aspects and analytical approach.* Spectrochim. Acta Part B, 2004. 59:1431–1438

111. Scaffidi, J., Pearman, W., Carter, J. C., and Angel, S. M., *Observations in Collinear Femtosecond–Nanosecond Dual-Pulse Laser-Induced Breakdown Spectroscopy.* Applied Spectroscopy, 2006. 60: 65-71

112. Schiffern, J. T., Doerr, D. W., and Alexander, D. R., *Optimization of collinear double-pulse femtosecond laser-induced breakdown spectroscopy of silicon.* Spectrochimica Acta Part B: Atomic Spectroscopy, 2007. 62: 1412–1418

113. Yalcin, S., Tsui, Y.Y., and Fedosejevs, R., *Pressure dependence of emission intensity in femtosecond laser-induced breakdown spectroscopy*. Journal of Analytical Atomic Spectrometry, 2004. 19: 1295-1301.

114. Cremers, D. A., Radziemski, L. J., and Loree, T. R., *Spectrochemical Analysis of Liquids Using the Laser Spark.* Applied Spectroscopy, 1984. 38: 721-729

115. Scaffidi, J., Angel, S.M., and Cremers, D.A., *Emission enhancement mechanisms in dual-pulse LIBS*. Analytical Chemistry, 2006. 78: 24-32.

116. Stratis, D. N., Eland, K. L., and Angel, S. M., *Dual-Pulse LIBS Using a Pre-ablation Spark for Enhanced Ablation and Emission*. Applied Spectroscopy, 2000. 54: 1270-1274

117. Baudelet, M., Boueri, M., Yu, J., Mao, S. S., Piscitelli, V., Mao, X., Russo, R. E., *Time-resolved ultraviolet laser-induced breakdown spectroscopy for organic material analysis*. Spectrochimica Acta Part B: Atomic Spectroscopy, 2007. 62:1329–1334.

118. Le Drogoff, B., Margot, J., Chaker, M., Sabsabi, M., Barthelemy, O., Johnston, T.W., Laville, S., Vidal, F., and von Kaenel, Y., *Temporal characterization of femtosecond laser pulses induced plasma for spectrochemical analysis of aluminum alloys*. Spectrochimica Acta Part B - Atomic Spectroscopy, 2001. 56: 987-1002.

119. Baudelet, M., Guyon, L., Yu J., Wolf, J. -P., Amodeo, T., Fréjafon, E., and Laloi, P., *Femtosecond time-resolved laser-induced breakdown spectroscopy for detection and identification of bacteria: A comparison to the nanosecond regime.* J. Appl. Phys., 2006. 99:084701

120. Svoboda, K., Denk, W., Kleinfeld, D., and Tank, D.W., *In vivo dendritic calcium dynamics in neocortical pyramidal neurons*. Nature, 1997. 385: 161-165.

121. Kleinfeld, D., Mitra, P.P., Helmchen, F., and Denk, W., *Fluctuations and stimulus-induced changes in blood flow observed in individual capillaries in layers 2 through 4 of rat neocortex*. Proceedings of the National Academy of Sciences USA, 1998. 95: 15741-15746.

122. Grutzendler, J., Kasthuri, N., and Gan, W.B., *Long-term dendritic spine stability in the adult cortex*. Nature, 2002. 420: 812-816.

123. Drew, P.J., Shih, A.Y., Driscoll, J.D., Knutsen, P.M., Davalos, D., Blinder, P., Akassoglou, K., Tsai, P.S., and Kleinfeld, D*., Chronic optical access through a polished and reinforced thinned skull*. Nature Methods, 2010. 7: 981-984.

124. Yang, G., Pan, F., Parkhurst, C.N., Grutzendler, J., and Gan, W.B., *Thinned-skull cranial window technique for long-term imaging of the cortex in live mice*. Nature Protocols, 2010. 5: 201-208.

125. Levasseur, J.E., Wei, E.P., Raper, A.J., Kontos, A.A., and Patterson, J.L., *Detailed description of a cranial window technique for acute and chronic experiments*. Stroke, 1975. 6: 308-317.

126. Holtmaat, A., Bonhoeffer, T., Chow, D.K., Chuckowree, J., De Paola, V., Hofer, S.B., Hübener, M., Keck, T., Knott, G., Lee, W.C., Mostany, R., Mrsic-Flogel, T.D., Nedivi, E., Portera-Cailliau, C., Svoboda, K., Trachtenberg, J.T., and Wilbrecht, L., *Long-term, high-resolution imaging in the mouse neocortex through a chronic cranial window*. Nature Protocols, 2009. 4: 1128-1144.

127. Xu, H.T., Pan, F., Yang, G., and Gan, W.B., *Choice of cranial window type for in vivo imaging affects dendritic spine turnover in the cortex*. Nature Neuroscience, 2007. 10: 549-551.

128. Arieli, A., Grinvald, A., and Slovin, H., *Dural substitute for long-term imaging of cortical activity in behaving monkeys and its clinical implications*. Journal of Neuroscience Methods, 2002. 114: 119-133.

129. Piper, R.D., Lambert, G.A., and Duckworth, J.W., *Cortical blood flow changes during spreading depression in cats.* American Journal of Physiology, 1991. 261: H96-H102.

130. Helmchen, F. and Denk, W., *Deep tissue two-photon microscopy*. Nature Methods, 2005. 2: 932-940.

131. Wilt, B.A., Burns, L.D., Wei Ho, E.T., Ghosh, K.K., Mukamel, E.A., and Schnitzer, M.J., *Advances in light microscopy for neuroscience*. Annual Review of Neurosciences, 2009. 32: 435-506.

132. Miyawaki, A., *Innovations in the imaging of brain functions using fluorescent proteins*. Neuron, 2005. 48: 189-199.

133. Davalos, D., Lee, J.K., Smith, W.B., Brinkman, B., Ellisman, M.H., Zheng, B., and Akassoglou, K., *Stable in vivo imaging of densely populated glia, axons and blood vessels in the mouse spinal cord using two-photon microscopy*. Journal of Neuroscience Methods, 2008. 169: 1-7.

134. van der Harst, M. R., Brama, P. A., van de Lest, C. H., Kiers, G. H., DeGroot, J., van Weeren, P. R., *An integral biochemical analysis of the main constituents of articular cartilage, subchondral and trabecular bone*. Osteoarthritis and Cartilage, 2004. 12:752-761

135. Jung, S., Aliberti, J., Graemmel, P., Sunshine, M. J., Kreutzberg, G. W., Sher, A., and Littman, D. R., *Analysis of Fractalkine Receptor CX3CR1 Function by Targeted Deletion and Green Fluorescent Protein Reporter Gene Insertion*. Mol Cell Biol, 2000. 20: 4106–4114.

136. Cheung, K.C., *Implantable microscale neural interfaces*. Biomed Microdevices, 2007. 9:923–938

137. Boyden, E. S., Zhang, F., Bamberg, E., Nagel, G., Deisseroth, K., *Millisecond-timescale, genetically targeted optical control of neural activity*. Nat. Neurosci, 2005. 8: 1263–8

138. Oron, D., Tal, E., and Silberberg, Y., *Scanningless depth-resolved microscopy*. Optics Express, 2005. 13:1468-1476

139. Vitek, D. N., Block, E., Bellouard, Y., Adams, D. E., Backus, S., Kleinfeld, D., Durfee, C. G., and Squier, J. A., *Spatio-temporally focused femtosecond laser pulses for nonreciprocal writing in optically transparent materials*. Optics Express, 2010. 18:24673-24678